

INVESTIGATION OF NOZZLE PERFORMANCE FOR
ROTATING DETONATION ROCKET ENGINES

A Dissertation

Submitted to the Faculty

of

Purdue University

by

Alexis J. Harroun

In Partial Fulfillment of the

Requirements for the Degree

of

Master of Science

August 2019

Purdue University

West Lafayette, Indiana

**THE PURDUE UNIVERSITY GRADUATE SCHOOL
STATEMENT OF DISSERTATION APPROVAL**

Dr. Stephen D. Heister, Chair

School of Aeronautics and Astronautics

Dr. Carson D. Slabaugh

School of Aeronautics and Astronautics

Dr. William E. Anderson

School of Aeronautics and Astronautics

Dr. Douglas A. Schwer

Naval Research Laboratory

Approved by:

Dr. Weinong W. Chen

Head of the School Graduate Program

ACKNOWLEDGMENTS

I would like to thank the many people who have supported me throughout my education and especially through my master's thesis work. I would like to thank my advising professor, Dr. Stephen Heister, for helping me turn an off-hand observation from a presentation he gave at my undergraduate institution my senior year into a full fledged research thesis. Thank you to my thesis committee, including Drs. Carson Slabaugh, Bill Anderson, and Doug Schwer, for their advice and review of my work.

Thank you to Swanand Sardeshmekh for bringing me up to speed with CFD and Linux. His help was a boon to a student who had never performed a CFD study before. Thank you to my NASA mentor, Joe Ruf, who provided me expertise on aerospike nozzles and more on CFD. Joe is the reason I have presentable computational results.

My colleagues in my research group were fundamental to my success. Thank you to Kota Mikoshiba, for many discussions involving CFD and help with computer problems. Thank you to Dasheng Lim for help with designing the hardware for the nozzle experiments. Thank you to both Dasheng and Jenna Humble for letting me tag along to obtain nozzle experimental data. Along with their technical contributions, my research group was a constant source of moral support, key to surviving graduate school in a new state.

I would like to acknowledge the substantial contribution from the NASA Space Technology Research Grant which provided both financial and technical support of this thesis research.

Finally, thank you to the ones who have supported me from afar. My parents have supported me throughout my life and raised me to believe nothing was impossible for me to accomplish. And thank you to Lucas Heflin, whose proofreading efforts are the reason I was accepted to graduate school and won my fellowship in the first place.

TABLE OF CONTENTS

	Page
LIST OF TABLES	viii
LIST OF FIGURES	x
SYMBOLS	xv
ABBREVIATIONS	xvii
ABSTRACT	xviii
1 INTRODUCTION	1
1.1 Overview of Rotating Detonation Engines	1
1.2 Motivation for RDE Nozzle Study	4
1.3 Aerospike Nozzles	8
1.3.1 Flow Physics	10
1.3.2 Internal-External Expansion Design	14
1.3.3 Flared Design	17
1.4 Challenges to Aerospike Integration with RDEs	18
1.5 Considerations for Nozzleless Geometries	20
1.6 Study Objectives and Approach	22
2 COMPUTATIONAL FRAMEWORK	23
2.1 Geometries of Interest	23
2.1.1 Nozzleless Configuration	23
2.1.2 IE-Aerospike Configuration	24
2.1.3 Flared Aerospike Configuration	26
2.2 CFD Solver	28
2.2.1 Solver Validation	29
2.3 Computational Domain, Meshing, and Boundary Conditions	31
2.4 Inflow Boundary Condition	33

	Page
2.4.1 Gas Model	37
2.5 Turbulence Modeling	39
2.6 Meshing and Mesh Sensitivity Study	40
2.7 Solver Parameters	47
2.7.1 Axisymmetric Steady Cases	47
2.7.2 3D Steady Cases	48
2.7.3 3D Time-Varying Cases	48
2.8 Study Approaches	49
2.8.1 2D Axisymmetric Time Average	49
2.8.2 3D Constant Pressure and Detonation Waveform Model	49
2.9 Performance Metrics	50
3 COMPUTATIONAL RESULTS	52
3.1 Nozzleless Results	52
3.1.1 Performance Results	52
3.1.2 Flow Features	54
3.1.3 Base Pressure Contribution	58
3.2 IE-Aerospike Results	62
3.2.1 Performance Results	62
3.2.2 Flow Features	64
3.2.3 Ramp Thrust Contribution	69
3.3 Nozzleless versus IE-Aerospike Results	72
3.3.1 Overall Performance	72
3.3.2 Comparing Axisymmetric 2D Time-Averaged and Full 3D So- lutions	73
3.4 Flared Aerospike Results	74
3.4.1 Flow Features	74
3.4.2 Performance Results	76
3.5 Wave Number	78

	Page
3.5.1 Overall Performance	80
3.5.2 Surface Pressures	80
3.5.3 Refreshing Parameter	82
3.6 Internal Expansion Ratio Results	84
3.6.1 Explanation of IEAR/IEPR	84
3.6.2 Overall Performance	86
3.7 Channel Length	89
3.7.1 Overall Performance	90
3.7.2 Surface Pressures	91
4 EXPERIMENTAL RESULTS	94
4.1 RDE V1.3 Test Campaign	94
4.1.1 Background	94
4.1.2 Instrumentation	94
4.1.3 Comparison of Experimental Performance to Computation Results	95
4.2 RDE V1.4 Test Campaign	97
4.2.1 Background	97
4.2.2 Instrumentation	99
4.2.3 Evaluation of Nozzleless Results	101
4.2.4 Evaluation of IE-Aerospike Results	106
4.2.5 Comparison of Different Nozzle Designs	108
5 CONCLUSIONS	114
5.1 Main Conclusions	114
5.1.1 RDE Nozzleless Configuration as Enhanced Ejector	114
5.1.2 Delay of Flow Separation for RDE Aerospike	115
5.1.3 Flared versus IE-Aerospike Design	117
5.1.4 Use of 2D Axisymmetric Cases to Approximate 3D Results . . .	117
5.1.5 Comparison of Computational and Experimental Results . . .	118
5.2 Lessons Learned	119

	Page
5.2.1 CFD Solver Stability	119
5.2.2 Design Hardware with Diagnostics in Mind	120
5.3 Future Work	120
5.3.1 Analysis of Different Parameters	120
5.3.2 Altitude Testing for High Area Ratio Nozzle Concepts	122
5.3.3 Application of New Physics to Current Nozzle Performance Calculation Methods	122
REFERENCES	123
A RDE V1.4 Hardware Drawings	127

LIST OF TABLES

Table	Page
2.1 Purdue RDE V1.3 Test #53 Conditions	34
2.2 Mass weighted percentages for different evaluated specie models based on methane/gaseous oxygen detonation.	38
2.3 Normalized error compared to full detonation species for different species models.	39
2.4 Mesh sensitivity study for IE-aerospike domain.	44
2.5 Mesh sensitivity study for nozzleless domain.	44
2.6 Mesh sensitivity study for flared aerospike domain.	46
2.7 Computational parameters for axisymmetric cases.	47
2.8 Computational parameters for 3D steady-state cases.	48
2.9 Computational parameters for 3D time-varying cases.	49
3.1 Performance results of nozzleless geometry with constant mass flow inlet and two-wave detonation pressure profile.	53
3.2 Performance results of IE-aerospike geometry with constant mass flow inlet and two-wave detonation pressure profile.	63
3.3 Detonation wave pressure profile performance time-averaged results for nozzleless and IE-aerospike geometries.	72
3.4 Results of 3D detonation wave case versus time-averaged 2D axisymmetric cases for nozzleless and IE-aerospike geometries.	73
3.5 Performance results of 2D axisymmetric time-averaged detonation wave pressure profile for IE- and flared aerospike geometries.	76
3.6 Flow conditions and performance for different wave numbers with same pressure impulse waveforms.	80
3.7 Time scales, refreshing parameter, and helical angle for 1, 2, and 4 wave cases.	84
3.8 Dimensions, internal-expansion area ratio, and internal-expansion pressure ratios considered for internal-expansion parametric study.	86

Table	Page
3.9 Performance results for original, half-, and quarter- length chambers. . . .	91
4.1 Average experimental specific impulse from v1.3 test campaign for nozzle- less and IE-aerospike geometries compared to computational results of 3D time-varying and 2D logarithmic averaged solution.	97
4.2 Conditions for low-, mid-, and high-pressure paired tests for IE- and flared aerospike geometries.	109

LIST OF FIGURES

Figure	Page
1.1 Schematic of generic annular RDE configuration. [1]	2
1.2 Unwrapped view of RDE combustion chamber. [3]	3
1.3 Experimental RDE chamber pressure at one station as function of time. [12]	5
1.4 Schematic of aerospike and de Laval nozzles.	9
1.5 Test photo of X-33 linear aerospike engine. [Courtesy NASA]	10
1.6 Specific impulse of aerospike and de Laval nozzles ($\epsilon=55$) compared to ideal adapted nozzle over a range of pressure altitudes. Adapted from [24].	11
1.7 Specific impulse of aerospike nozzles with different area ratios compared to ideal nozzle at (a) high and (b) low pressure ratios.	12
1.8 Flow phenomena for full-length aerospike nozzles, for over- (top), opti- mally (middle), and underexpanded (bottom) cases. [25]	14
1.9 Nozzle plug surface pressure for overexpanded (top curve) to optimally expanded cases (bottom curve). [25]	15
1.10 Fully external and internal-external designs for aerospike nozzle.	16
1.11 Method of characteristics schematic for IE-aerospike nozzle. [27]	17
1.12 Flared aerospike design.	18
1.13 Cross-sectional view of internal-external (IE) and flared aerospike designs. Dashed lines denote IE cowl and plume boundary at its optimal NPR while solid lines denote flared cowl and plume.	19
1.14 Base pressure for rocket RDE test. [5]	21
2.1 Isometric view of nozzleless geometry for Purdue rocket RDE.	24
2.2 Cross-sectional view of nozzleless geometry for Purdue rocket RDE.	25
2.3 Isometric view of IE-aerospike geometry for Purdue rocket RDE.	25
2.4 Cross-sectional view of IE-aerospike geometry for Purdue rocket RDE.	26
2.5 Method of characteristics for internal expansion of IE-aerospike with linear cone of half-angle 22.57 degrees. [10]	27

Figure	Page
2.6 Isometric view of flared aerospike geometry for Purdue rocket RDE.	28
2.7 Cross-sectional view of flared aerospike geometry for Purdue rocket RDE. . .	28
2.8 Geometry of dual thruster aerospike experiment. Left, sample points were on aerospike plug. Right, close-up view of stacked thrusters. [33]	30
2.9 Experimental (triangles) and computational (circles) results for different nozzle pressure ratios from dual thruster validation study.	31
2.10 Computational domain of aerospike geometry, dimensional units in inches. . .	32
2.11 Computational domain of nozzleless geometry, dimensional units in inches. . .	33
2.12 Generated pressure waveform for Test #53 two-wave detonation at two different times: initial time and half period later.	36
2.13 Snapshots of pressure inlet at three different times in cycle. Pressure inlet imposed 3.9 in upstream from RDE exit plane. Pressure in Pa.	36
2.14 Computational results of turbulence model comparative study including surface pressure as function of radial distance. Surface-averaged base pres- sure of BSL Sarkar* model was compared to test data.	41
2.15 Mesh for aerospike domain.	42
2.16 Mesh for nozzleless domain.	42
2.17 Dimensional and y^+ distance of first cell off wall for four critical locations in aerospace domain.	43
2.18 Two snapshots of oscillating plume behavior for nozzleless geometry with high mesh resolution.	45
2.19 Process for using axisymmetric cases at different pressure ratios to esti- mate RDE cycle time average result.	50
3.1 Instantaneous pressure contour of RDE inlet and inner detonation channel surface and Mach contour of channel exhaust plume on symmetry plane for nozzleless geometry with detonation wave case. Detonation pressure wave is imposed on inlet end of the annular combustion chamber 7.0 cm in length with gap of 0.7 cm. Diameter of combustion chamber is 9.9 cm. . .	55
3.2 Cross-sectional view of nozzleless geometry at one azimuthal location of exhaust plume Mach contour for two different times for constant mass flow case.	56
3.3 Cross-sectional view of nozzleless geometry at one azimuthal location of exhaust plume Mach (left) and pressure (right) contours at three different times in detonation wave cycle. Pressure measured in Pa.	57

Figure	Page
3.4 Surface pressure on nozzleless base region for steady constant mass flow inflow and time-averaged result for time-varying detonation wave nozzle inflow as function of radial distance.	60
3.5 Base pressure profile as function of radial distance for same azimuthal slice at three different times in detonation wave cycle. Cycle time averaged base pressure profile also shown.	61
3.6 Pressure contours at base region for same azimuthal slice at three different times in detonation wave cycle. Pressure in Pa.	62
3.7 Instantaneous pressure contour of RDE inlet and inner detonation channel surface and Mach contour of channel exhaust plume on symmetry plane for IE-aerospike geometry with detonation wave case.	65
3.8 Pressure contour and particle flow path plot on surface of RDE inner chamber and aerospike plug. Pressure wave is imposed on the left-hand boundary and flow moves downstream to the right. Wave rotation direction is from bottom to top.	66
3.9 Isometric view of pressure contour and particle flow path plot on surface of RDE inner chamber and aerospike plug. Pressure wave interface on cone shown with red dashed line.	67
3.10 Cross-sectional view of IE-aerospike geometry at one azimuthal location of exhaust plume Mach (left) and pressure (right) contours at three different times in detonation wave cycle. Pressure in Pa.	68
3.11 Surface pressure on IE-aerospike plug for constant mass flow and time-averaged result of time-varying detonation wave inflow as function of axial distance. Cowl exit plane at 2.5 cm.	70
3.12 Normalized surface pressure over axial distance at one azimuthal location for three times in detonation wave cycle. Cycle time-averaged solution also shown. Cowl exit plane at 2.5 cm.	71
3.13 Mach contour plots for IE-aerospike (left) and flared aerospike (right) at $NPR = 3, 8.5,$ and 30	75
3.14 Nozzle efficiency as function of NPR for IE- and flared aerospike. Time-averaged result also shown (dashed).	77
3.15 Coefficient of thrust contribution from ramp (circles) and cowl (diamonds) for IE- and flared aerospike geometries.	78
3.16 Detonation pressure waveforms as function of azimuthal location in channel for 1, 2, and 4 wave cases.	79

Figure	Page
3.17 Surface pressure on ramp surface for 1, 2, and 4 wave cases at same CTAP compared to constant mass flow case. Cowl exit plane at 2.5 cm.	81
3.18 Change of IEAR for annular aerospike geometry with constant throat area and nozzle area ratio.	85
3.19 Mach contours of exhaust plume for different internal expansion pressure ratios.	87
3.20 Specific impulse with changing internal expansion pressure ratio for flared aerospike geometry; operating overall pressure ratio shown (dashed). . . .	88
3.21 Component coefficient of thrust for flared aerospike ramp and cowl surfaces with changing internal-expansion pressure ratio.	89
3.22 Surface pressures on chamber wall and ramp surfaces for original, half-, and quarter-length chambers. Cowl exit plane at 2.5 cm.	92
3.23 Flow fields inside each chamber for chamber length study. From left to right, (a) original, (b) half-, and (c) quarter-length chambers. Inner chamber wall is mapped with colored pressure contours. Gray volume designates Mach 1 iso-surface. Flow is from left to right in each chamber. . . .	93
4.1 Specific impulse of RDE V1.3 experiments, 2D axisymmetric time-averaged computational result, and 3D time-varying computational result for IE-aerospike and nozzleless configurations at nominal mass flow of 1.1 kg/s. . .	96
4.2 Specific impulse of RDE V1.3 experiments, 2D axisymmetric time-averaged computational result, and 3D time-varying computational result for IE-aerospike and nozzleless configurations for all mass flow rates considered. . .	98
4.3 Photos of V1.4 RDE with 4.5 cm detonation channel diameter. (a) IE-aerospike nozzle and (b) nozzleless configuration.	99
4.4 Cut-away of nozzleless configuration with pressure ports on base surface.	101
4.5 Computer-aided design and hardware of nozzleless configuration with seven pressure ports.	102
4.6 Cut-away of aerospike nozzle configuration with pressure ports on ramp surface.	103
4.7 Computer-aided design (head-on view) and hardware (profile view) of aerospike plug with six pressure ports.	104
4.8 Base pressure plots of seven base region locations on nozzleless geometry for Test #49.	105

Figure	Page
4.9 Low-pass filtered base pressures for seven radial locations on nozzleless geometry for Test #49 during RDE window of operation.	106
4.10 Base pressure plots for V1.3 computations, including results from constant mass flow case and detonation wave case, compared to experimental results from V1.4 Tests #54, 55, 65, 66, and 79 for nozzleless geometry.	107
4.11 Base pressure as function of incoming mass flow for V1.4 nozzleless experiments. Compared to Stechmanns analytical model. [10]	108
4.12 Normalized base pressure to atmospheric pressure for V1.4 nozzleless experiments. Closed to open wake transition at approximately $P_a/P_c = 0.15$	109
4.13 Surface pressure plots of six ramp locations on IE-aerospike geometry for Test #70.	110
4.14 Low-pass filtered ramp pressures for six axial locations on IE-aerospike geometry for Test #70 during RDE window of operation.	111
4.15 Surface pressure plots for V1.3 computations, including results from constant mass flow case and detonation wave case, compared to experimental results from V1.4 Tests #69, 70, and 77 for IE-aerospike geometry. Cowl exit plane at 2.5 cm.	112
4.16 CTAP normalized surface pressures for IE- and flared aerospike at different CTAPs.	113

SYMBOLS

A	area [m ²]
c_F	coefficient of force
F	force [N]
f	frequency [Hz]
g_0	acceleration of gravity [m/s ²]
I_{sp}	specific impulse [s]
L	diagonal length of nozzle [m]
M	Mach number
m	mass [kg]
\dot{m}	mass flow rate [kg/s]
n	wave number
P	pressure [Pa, atm]
r	radial distance [m]
T	temperature [K]
t	time [s]
v	velocity [m/s]
x	axial distance [m]
y^+	non-dimensional distance off of wall
α	turning angle
β	nozzle half-angle
γ	ratio of specific heats
ϵ	area ratio
η	efficiency

θ	azimuthal angle
τ	nozzle refreshing parameter

Subscripts

a	ambient
b	base
c	chamber
N	nozzle
t	throat

ABBREVIATIONS

ADAPT	Aerospike Design and Performance Tool
BC	boundary condition
CEA	NASA Chemical Equilibrium with Applications
CFD	computational fluid dynamics
CFL	Courant-Friedrichs-Lewy number
CJ	Chapman-Jouget
CTAP	capillary tube averaged pressure
GEMS	Generic Equation and Mesh Solver
IE	internal-external expansion
IEAR	internal expansion area ratio
IEPR	internal expansion pressure ratio
MOC	method of characteristics
MSFC	NASA Marshall Space Flight Center
NASA	National Aeronautics and Space Administration
NPR	nozzle pressure ratio
O:F	oxidizer-to-fuel ratio
PDE	pulse detonation engine
PR	pressure ratio
RDE	rotating detonation engine

ABSTRACT

Harroun, Alexis J. MS, Purdue University, August 2019. Investigation of Nozzle Performance for Rotating Detonation Rocket Engines. Major Professor: Stephen D. Heister.

Progress in conventional rocket engine technologies, based on constant pressure combustion, has plateaued in the past few decades. Rotating detonation engines (RDEs) are of particular interest to the rocket propulsion community as pressure gain combustion may provide improvements to specific impulse relevant to booster applications. Despite recent significant investment in RDE technologies, little research has been conducted to date into the effect of nozzle design on rocket application RDEs. Proper nozzle design is critical to capturing the thrust potential of the transient pressure ratios produced by the thrust chamber. A computational fluid dynamics study was conducted based on hotfire conditions tested in the Purdue V1.3 RDE campaign. Three geometries were investigated: nozzleless/blunt body, internal-external expansion (IE-) aerospike, and flared aerospike. The computational study found the RDE's dynamic exhaust plume enhances the ejection physics beyond that of a typical high pressure device. For the nozzleless geometry, the base pressure was drawn down below constant pressure estimates, increasing the base drag on the engine. For the aerospike geometries, the occurrence of flow separation on the plug was delayed, which has ramifications on nozzle design for operation at a range of pressure altitudes. The flared aerospike design, which has the ability to achieve much higher area ratios, was shown to have potential performance benefits over the limited IE-aerospike geometry. A new test campaign with the Purdue RDE V1.4 was designed with instrumentation to capture static pressures on the nozzleless and aerospike surfaces. These results were used to validate the results from the computational study. The computational and

experimental studies were used to identify new flow physics associated with a rocket RDE important to future nozzle design work. Future computational work is necessary to explore the effect of different parameters on the nozzle performance. More testing, including with an altitude simulation chamber, would help quantify the possible benefit of new aerospike nozzle designs, including the flared aerospike geometry.

1. INTRODUCTION

1.1 Overview of Rotating Detonation Engines

Conventional liquid rocket engines have approached their theoretical limit in terms of combustion efficiency. The technology peaked with the Space Shuttle Main Engine and the Russian RD-180, designed for ultra-high performance by using liquid hydrogen- and liquid kerosene-liquid oxygen, respectively. [1,2] Realizing the plateau of current rocket engine technologies, recently researchers have placed an increasing focus on alternative propulsion devices, including detonation-wave engines like pulse detonation engines (PDEs) and rotating detonation engines (RDEs).

A rotating detonation engine is a pressure-gain combustion device where a continuously travelling detonation wave or set of waves is used to combust propellants. Figure 1.1 shows a general configuration for an annular RDE, including the injection plane, annular combustion chamber, and a nozzle extending from the RDE exit plane. [3] The detonation wave travels normal to the injection plane, consumes the propellants, and the products are expanded and exhausted parallel to the engine centerline.

While conventional engines utilize the Brayton thermodynamic cycle, pressure-gain engines like RDEs operate on the Humphrey cycle. Unlike the Brayton cycle, where combustion is performed at a constant pressure, the constant volume combustion process in the Humphrey cycle allows for substantial pressure increases during the combustion event. [4,5] For RDEs, the constant-volume combustion step of the Humphrey cycle is due to detonation-based combustion. The leading shock of the detonation wave compresses and preheats the reactants. The reactants then exothermically release heat that further powers the propagation of the detonation wave. The greater the strength of the detonation, the greater the work output, where the

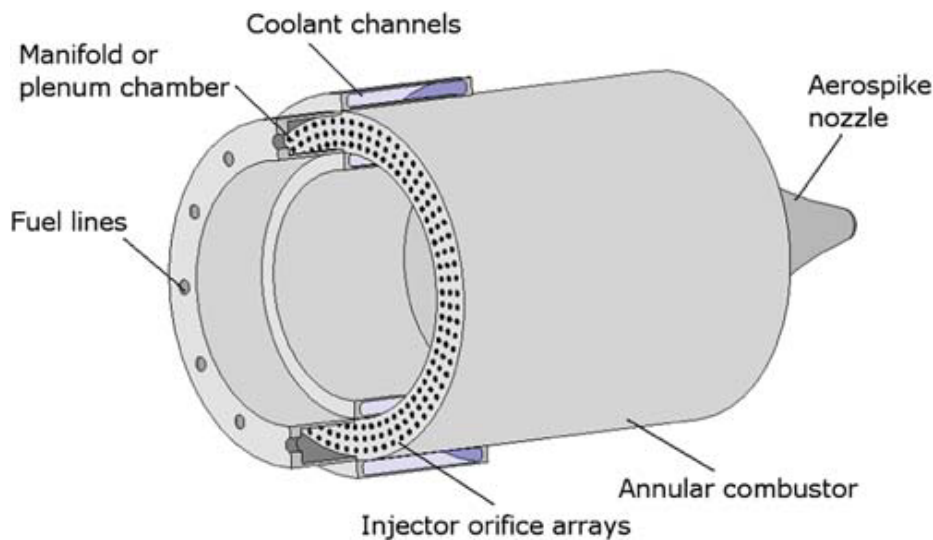


Fig. 1.1. Schematic of generic annular RDE configuration. [1]

strength is dependent on the propellant combination. Pressure ratios across the detonation wave for rocket relevant propellants range from $PR = 20$ for gaseous hydrogen/oxygen to $PR = 30$ for methane/oxygen. [6] The constant volume combustion of the Humphrey cycle generates less entropy compared to the Brayton cycle for the same work output, leading to significant improvements in efficiency. Some analyses of rocket RDEs predict that the thermodynamic cycle can lead to specific impulses 5-10% greater than conventional deflagration-based rocket engine concepts, a gain relevant to improving payload capacity by up to 100% for launch vehicles. [7]

Figure 1.2 shows an unwrapped view of the RDE combustion chamber and the regions of reactants, products, and the detonation wave. The detonation wave runs azimuthally around the annulus while the propellants are injected axially. Fresh reactants are injected before the detonation wave encounters and converts them into products. The high-pressure region after the detonation wave temporarily stops reactant injection. An expansion fan that extends behind the detonation wave expands the products and directs them downstream. The frequency of the detonation wave for rocket-relevant propellants can range from 5-30 kHz and multiple detonation waves can occur concurrently. The rotation and number of detonation waves causes the

chamber pressure to be a function of time at any one given station around the annulus.

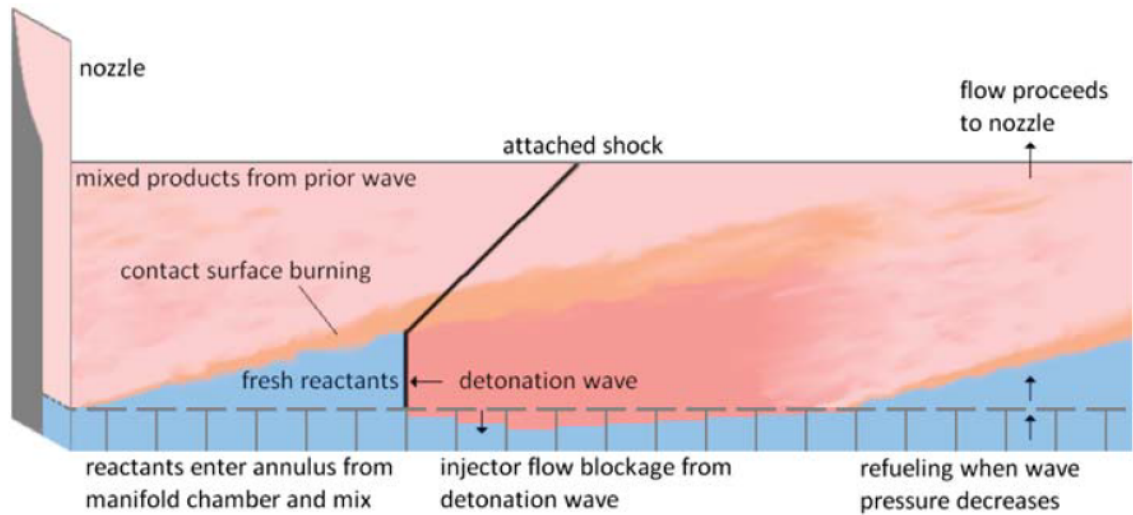


Fig. 1.2. Unwrapped view of RDE combustion chamber. [3]

Contrary to a conventional deflagration-based engine, an RDE does not necessarily require a geometric throat to choke the flow at the engine exit. The flow at the RDE exit plane for high pressure cases has been found to be supersonic in numerical computations. [8] It is debated if this choking is due to the chamber-to-ambient pressure ratio or thermal choking. At the bottom of the detonation cycle where the pressure is at a minimum, the RDE theoretically may unchoke; this behavior has not yet been investigated. For rocket cases, a geometric throat at best only serves to further reduce the mass flow by increasing the chamber pressure and reducing the injector mass flow. [9] At worst, a geometric throat prevents the distance the new reactants can travel, a critical parameter required for the formation of the detonation wave. In some rocket RDE experiments, geometric throats have been shown to cause flameholding behavior, which prevents detonation waves from forming entirely. [10] Computational studies show that a geometric restriction reflects the strong pressure waves back into the chamber and can cause instabilities in the fill layer of the injected

propellants, which may explain the destabilization of the detonation behavior. [11] For these reasons, only a divergent section may be needed – and may be required – to expand the products to an appropriate exit pressure to capture more of the useful energy of the rocket engine while maintaining stable detonation behavior. The aerodynamic features of the RDE, especially at its exit plane, are now important because the flow is sonic or supersonic and can generate shock losses. Boundary layers can also contribute to a virtual geometric throat; thus, some tapered expansion in the RDE itself may be necessary to prevent contraction of the flow inside the annulus.

1.2 Motivation for RDE Nozzle Study

The performance gains attributable to Humphrey cycle processes can only be realized if the nozzle is able to harness the additional work potential afforded by the detonation events. Several features of the RDE cause unique challenges for integrating a nozzle design. As seen in the pressure trace in Fig. 1.3, the chamber pressure, and thus the pressure at the RDE exit plane, varies as a function of time, spiking suddenly and then trailing off. [12] As the nozzle pressure ratio (NPR) is the prime parameter influencing nozzle design, the highly unsteady pressure ratios created by the RDE raise fundamental questions, i.e. since the nozzle contour cannot adjust to the instantaneous pressure ratio, one must choose a suitable average value to design the geometry. Current researchers in the gas turbine field advocate the use of an average pressure ratio for nozzle design, but the range of pressures and total mean pressure in a rocket cycle are much higher and it is not clear if this guideline still applies. Since a greater fraction of the mass flow is contributed from the high pressure gases directly behind the detonation wave, it may make sense to bias the nozzle contour to better convert these gases to thrust, while suffering off-design performance losses in the lower pressure part of the cycle.

Further questions involve the effect of the pressure profile on optimal extraction of useful work by the nozzle system. The actual shape of the detonation wave depends on

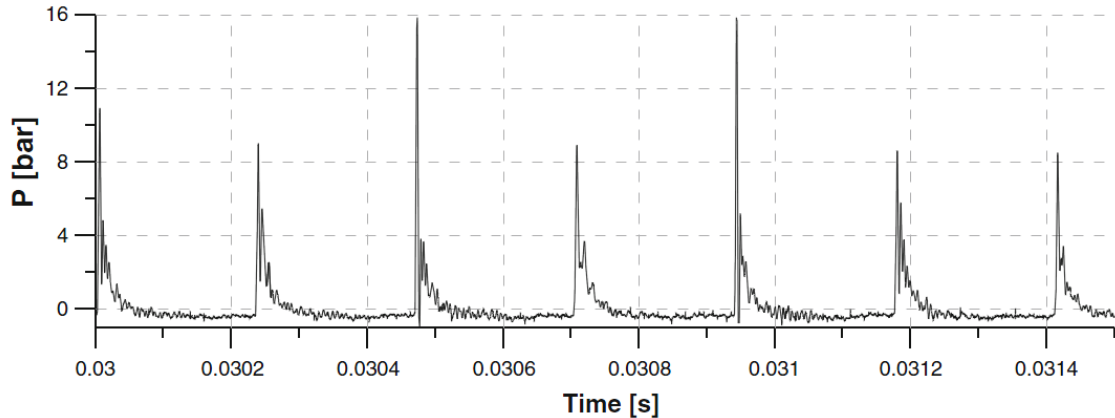


Fig. 1.3. Experimental RDE chamber pressure at one station as function of time. [12]

the fill height and specific injection conditions in the RDE combustor. Additionally, it is unknown how the pressure profile may homogenize in the RDE chamber and after the RDE exit plane as the flow expands azimuthally, which may relax the pressure spikes seen in the combustion chamber. While homogenization of the pressure wave may simplify the flow field entering the nozzle and allow for a more straightforward design, the thermodynamic benefit of the RDE cycle may be lost. [13]

Very few experiments and computational studies have assessed the effect of nozzle design or compared their results to nozzleless cases. Fewer have looked at rocket conditions, where the detonation pressure ratios and the average pressure in the chamber is greater than for air-breathing applications. The following studies comprise the relevant work to this thesis.

A zero-dimensional analysis by Stechmann et al. was created in order to assess rocket RDE performance for a range of different operating conditions. [7] This analysis also covered the effect of the nozzle, including no-nozzle, a bell nozzle, and an aerospike nozzle concept. The analysis found that the engine cycle benefits from using an aerospike nozzle, as the nozzle can naturally adapt to the different pressure ratios in the cycle. In particular, it found aerospike nozzles as enhancing the benefit

of detonation cycles over no nozzle by 2-6% in specific impulse, depending on the operating conditions.

An experimental study by Ishihara et al. of a gaseous ethylene/oxygen RDE was conducted with and without a conical plug. [14] No cowling was used to direct the flow prior to the engine exit. The experiment confirms the trend of the zero-dimensional study and shows that adding a conical aerospike nozzle enhances the thrust over no nozzle by 6-10%. Visually, it was evident that the plug helped to expand and direct the exhaust flow more efficiently.

Fotia et al. have conducted experiments to determine the performance of an aerospike on a hydrogen-fuel airbreathing RDE. [15, 16] In the first experiment, they tested a general bluff body, recessed centerbody, unchoked and choked aerospikes. [16] The aerospikes had rounded corners at the RDE exit but were otherwise conical. It was found that choked aerospikes had higher specific impulses than unchoked aerospikes at the same mass flow rate for different chamber pressures and equivalence ratios and both performed better than the bluff body and recessed centerbody designs. It is theorized that the choked aerospike causes higher stagnation pressures in the combustor, enhancing the performance.

In the second experiment, a choked aerospike nozzle was used and the effect of the internal expansion ratio – the expansion within the cowl – and truncation were evaluated. [16] As to be expected, the thrust declined with increasing amount of truncation, but the results were within experimental error. The thrust also decreased as the internal expansion ratio was increased. The study theorized the effect was due to the reflection of a Mach wave at the cowl causing flow separation as the cowl length increased. It is unknown if the results from both these experiments will correlate to a rocket RDE, as airbreathing concepts typically do not suffer as much from flameholding effects with a choked nozzle as rocket concepts do. No information was provided into the design of an aerospike for these experiments.

Some computational studies from the Naval Research Laboratory and Naval Postgraduate School have focused on the performance gain of an aerospike for airbreathing

propulsion applications. [17, 18] It was shown that the averaged pressure profile on the nozzle for the 3D transient case matched the result of a 2D axisymmetric constant inlet boundary condition at the average pressure. Because of the low pressure ratio inherent to the airbreathing cycle, the nozzle design employed in the referenced study includes a large base region which essentially mimics a nozzleless geometry. It is uncertain that these results are applicable to high pressure rocket RDE nozzle design.

A computational study by Tsuboi et al. was conducted on unchoked conical nozzles for a hydrogen-oxygen RDE. [19] The study identified flow structures in the plume, primarily the oblique shock wave structure in the chamber and how it changes on the nozzle surface. Performance metrics such as specific impulse and thrust were computed with respect to various stagnation pressures and mass flow rates, but these results were not compared to any reference.

The purpose of this research is to decouple the performance of the nozzle from that of the RDE itself. For a constant pressure deflagration engine, 1D analytical models can be used to assess the theoretical effect of adding a converging-diverging nozzle on an engine. The performance for a constant pressure engine nozzle can be distilled to a few parameters, including the nozzle throat area and the supersonic area expansion ratio. For an RDE, it is difficult to remove the effect of RDE operation from the performance of the nozzle. The temporal and spatially evolving pressure wave from the engine has a large impact on the nozzle that makes one-dimensional analysis impossible. Decoupling the nozzle from the engine is important to determine the effectiveness of the engine design. Currently, tests run with and without a nozzle obfuscate the true potential of the engine, as losses or gains due to the nozzle design cannot be isolated. Finally, by isolating the nozzle performance, models may be made to effectively design a nozzle for any given engine concept.

The current study focuses on plug/aerospike nozzles and their specific effect on RDE performance. An aerospike nozzle is of particular interest because of its ability to naturally adapt to be optimized at pressure ratios below its design NPR. This would

allow the nozzle to compensate for low pressure ratio points in the pressure profile fed to the nozzle. Further, the annular topology of the RDE combustor naturally accommodates an aerospike geometry. These attributes have led to the proliferation of aerospike nozzle utilization on RDE experimental platforms; however, little research has been conducted to determine their effect on performance.

1.3 Aerospike Nozzles

An aerospike nozzle employs a centerbody plug to expand the flow of combustor products to a given ambient pressure. As there is no physical outer boundary, the exhaust plume shape expands or contracts such that the exit pressure matches the ambient pressure. For this reason, aerospike nozzles are considered altitude compensating, as the plume naturally adjusts to the ambient conditions. [20] Figure 1.4 compares the geometry and plume of an aerospike nozzle with a de Laval nozzle at on-design pressure conditions. Aerospikes typically consist of an outer cowl and a plug spike. The cowl typically turns the flow from the axially exhausting flow of the combustor to some flow angle. The spike then turns the flow exiting the cowl back parallel to the nozzle axis, expanding the flow to the exit Mach number to achieve a given exit pressure. Typically the spike is truncated a certain percentage of its length, seen in Fig. 1.4, as little pressure thrust is generated on the end of the nozzle compared to the weight generated from the length.

Altitude compensating nozzles are of interest for rocket launching applications where the vehicle ascends through a range of pressure altitudes before entering a vacuum condition. The most notable work on an aerospike engine is the Lockheed Martin X-33 program. The X-33 was a lifting body vehicle concept intended as a demonstration for the VentureStar, a single-stage-to-orbit vehicle. [21] The X-33 used the Boeing Rocketdyne XRS-2200 linear aerospike engine to improve performance for the wide range of pressure altitudes expected in the flight profile. Linearly clustered engines fed into a linear truncated aerospike plug (Fig. 1.5). This engine was ex-

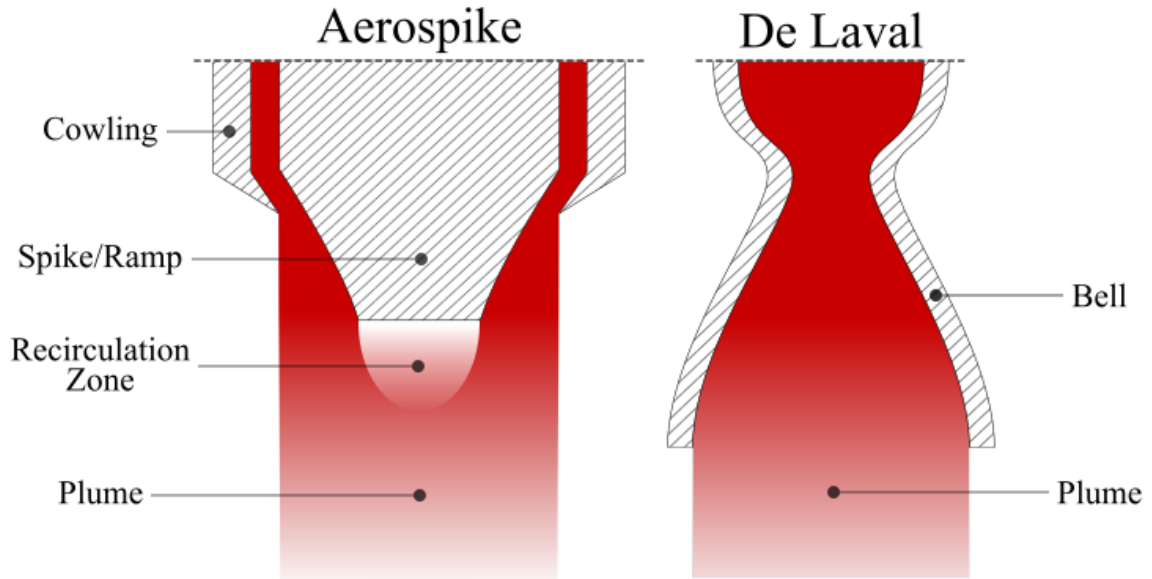


Fig. 1.4. Schematic of aerospike and de Laval nozzles.

tensively tested on ground; however, the X-33 program was eventually abandoned. The aerospike nozzle showed promise but had difficulties with thermal management. Korte contributed multiple studies into optimizing an aerospike nozzle for the X-33 program, including structural and aerodynamic analysis, and a parametric model for nozzle integration. [22, 23]

In particular, aerospike nozzles achieve much higher performance than fixed-area-ratio de Laval nozzles at low pressure altitudes, making them good candidates for first stage propulsion applications. Figure 1.6 shows that an aerospike nozzle reaches the ideal nozzle performance at pressure altitudes below its design pressure altitude, compared to a de Laval nozzle. However, issues do persist for aerospikes nozzle designs. Practically, they behave at the same performance or worse than de Laval nozzles at high altitudes, where a large portion of a first stage burn occurs. Additionally, the base of the rocket, including the outside of the cowling, may experience form or wave drag and cause low pressure regions which can negatively impact the performance of

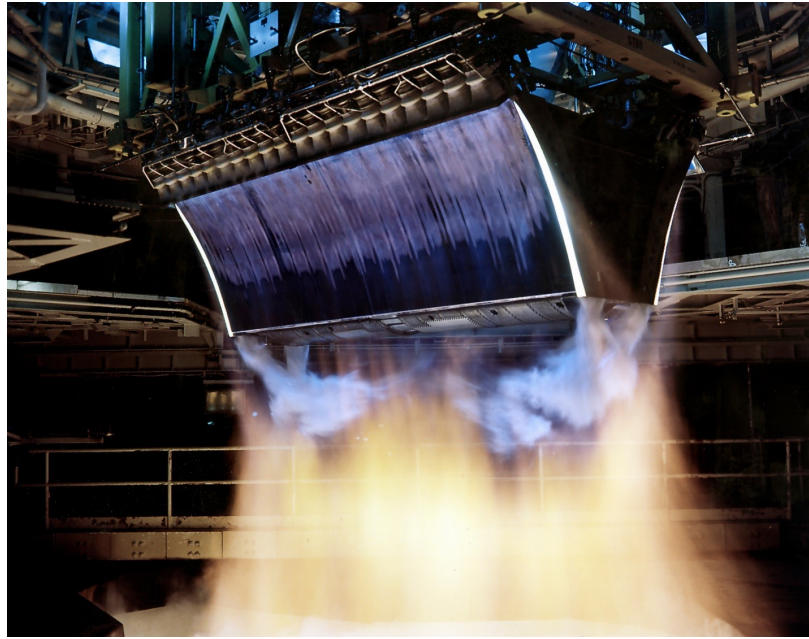


Fig. 1.5. Test photo of X-33 linear aerospike engine. [Courtesy NASA]

the aerospike, which relies on the local ambient pressure. Altering the geometry of the base of the vehicle can help alleviate these performance losses.

1.3.1 Flow Physics

As the external boundary of the aerospike plume is controlled by the ambient pressure, the plume is subject to change based on the current chamber pressure to ambient pressure ratio. Thus, the plume will vary both with pressure altitude and the natural chamber pressure oscillation of the RDE. Both underexpanded and overexpanded plumes induce shock losses that negatively affect the performance; however, Hagemann (1998) suggested that the most benefit can be gained by designing nozzle area ratio to be as high as possible. [25] This suggests it is best to operate the nozzle at optimal to overexpanded conditions at all times to benefit the most from the altitude compensatory effects of an aerospike. Figure 1.7 shows the specific impulse of aerospike nozzles of different area ratios compared to an ideal adapted nozzle. In Fig.

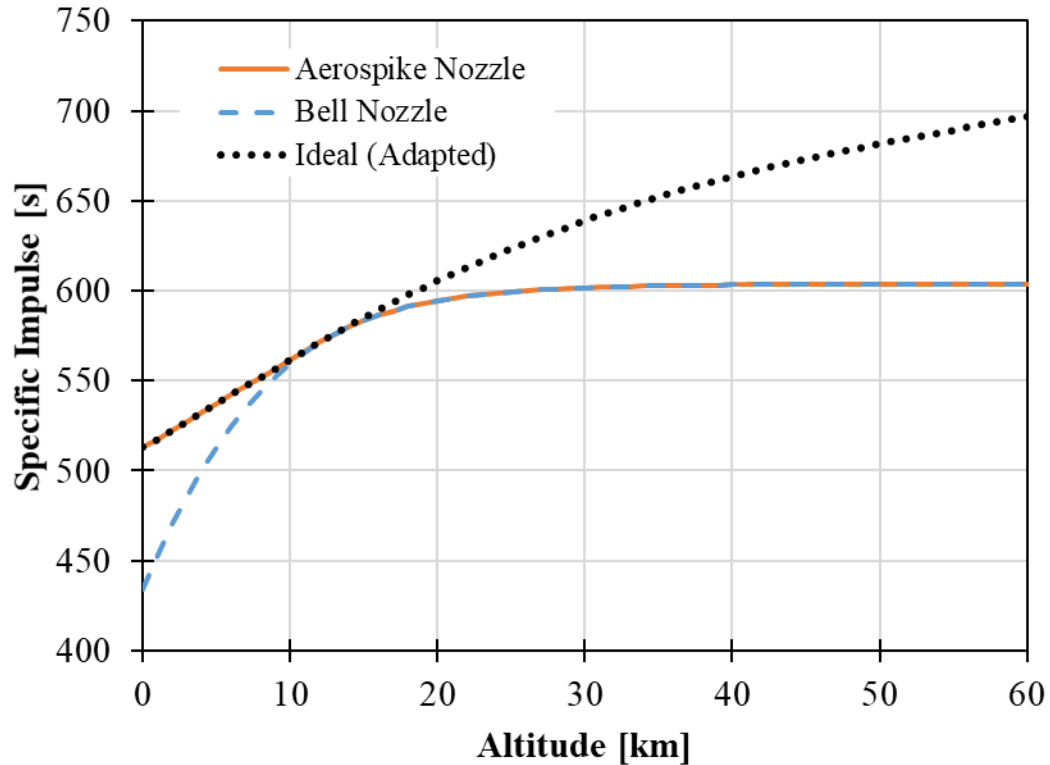
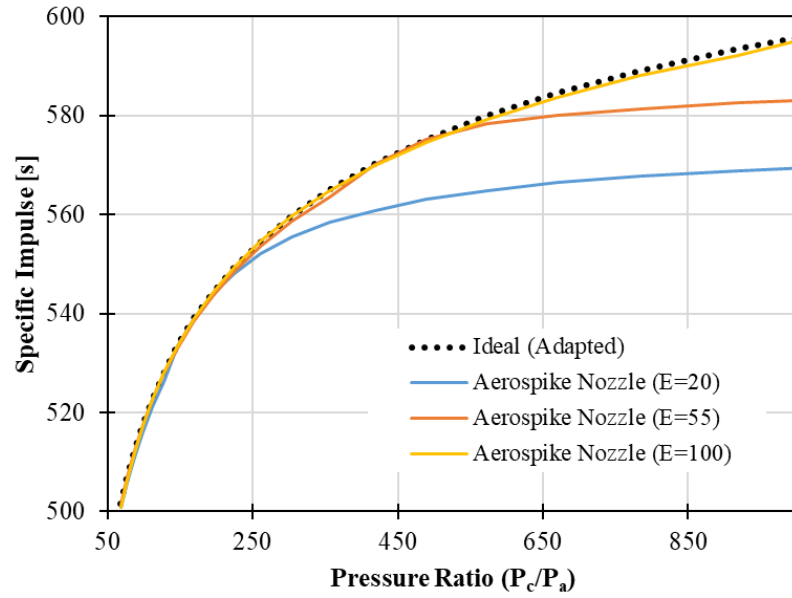


Fig. 1.6. Specific impulse of aerospike and de Laval nozzles ($\epsilon=55$) compared to ideal adapted nozzle over a range of pressure altitudes. Adapted from [24].

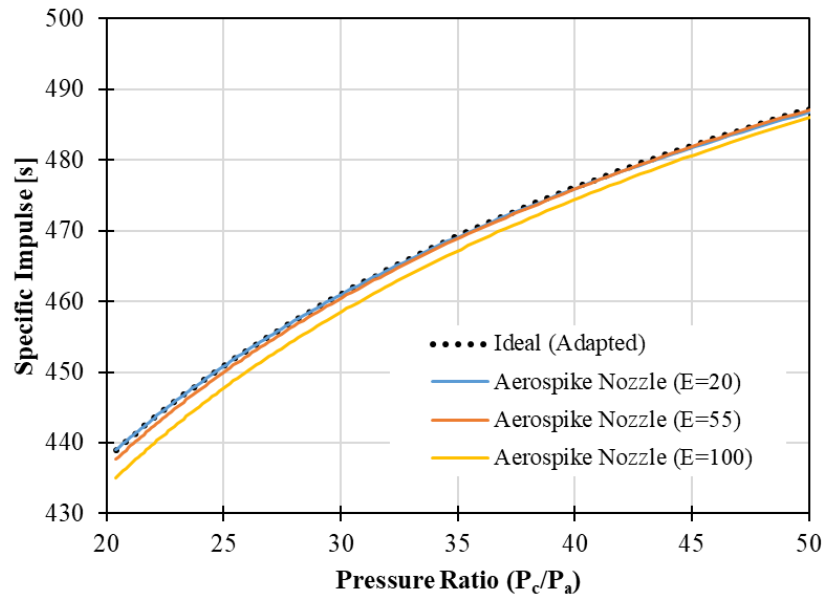
1.7(a), it is obvious that the larger area ratio aerospike is preferred when operating at high pressure ratios. A less obvious result, however, is that the high area ratio can lead to significant overexpansion at low pressure ratios, leading to flow separation losses, seen in Fig. 1.7(b).

When the pressure ratio is at the design case, the final right-running characteristic runs from the cowling lip to the final point on the aerospike plug (Fig. 1.8, middle). The shear layer between the exhaust plume and ambient flow is parallel to the engine centerline. Ideally, no shock losses are experienced. This is the optimal expansion of the nozzle plume.

In the case of underexpansion (where the pressure ratio is greater than the designed pressure ratio), an expansion fan is generated off the cowling lip and a small



(a)



(b)

Fig. 1.7. Specific impulse of aerospike nozzles with different area ratios compared to ideal nozzle at (a) high and (b) low pressure ratios.

recirculation zone by the cowling lip appears (Fig. 1.8, lower). These effects cause a low pressure region, causing recompression waves and a barrel shock to form. As the plume expands beyond the footprint of the annulus, the nozzle behaves like a conventional nozzle, thus eliminating its pressure recovery capability. An aerospike nozzle is typically designed to avoid this condition because it no longer acts as an altitude compensating nozzle.

In the case of overexpansion (where the pressure ratio is below the designed pressure ratio), the ambient pressure counteracts the expansion of the flow radially, pushing the plume toward the engine centerline. The flow creates a system of compression and expansion waves that reflect off the shear layer (Fig. 1.8, top). The shear layer also grows with distance downstream from interactions with the compression and expansion waves and turbulent diffusion.

At very low pressure ratios, the system of shocks and expansion waves in over-expanded flow causes an oscillatory behavior of the pressure on the aerospike plug (Fig. 1.9). It has been noted that the oscillatory behavior of the wall pressure is not strong enough to cause flow separation on its own. Onofri stated that the compression shocks are intensified as the Mach number at the cowling exit is increased. [24] At moderately low pressure ratios, flow separation occurs at some point on the nozzle plug. When the flow separates, the nozzle compensates and the pressure on the surface increases. While this pressure-compensation can contribute to higher thrust due to higher integrated pressure force, the pressure oscillation at very low pressure ratios inherently causes a dynamic and unstable force on the plug.

Aerospike nozzles are typically designed with high area ratios to be overexpanded at the back pressures of interest. This is to avoid losses incurred when the flow is underexpanded. However, flow separation at low pressure ratios can incur dynamics on the nozzle that may be difficult to predict and control.

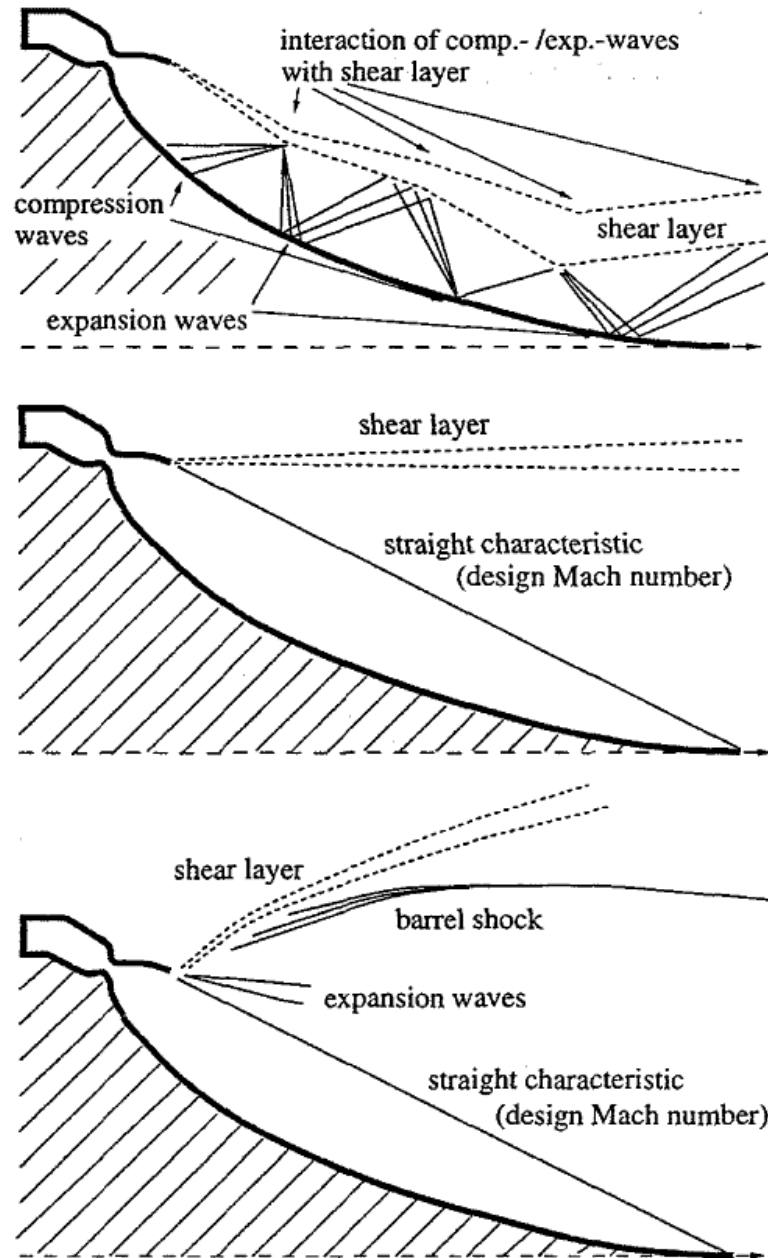


Fig. 1.8. Flow phenomena for full-length aerospike nozzles, for over- (top), optimally (middle), and underexpanded (bottom) cases. [25]

1.3.2 Internal-External Expansion Design

The geometry for an axisymmetric aerospike plug and cowling is typically generated using an inviscid axisymmetric method of characteristics for a prescribed pressure

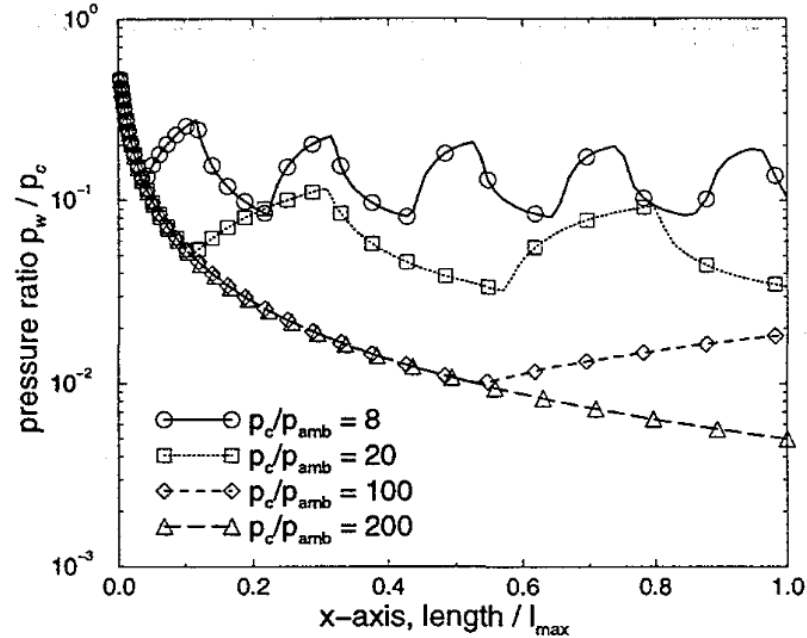


Fig. 1.9. Nozzle plug surface pressure for overexpanded (top curve) to optimally expanded cases (bottom curve). [25]

ratio. The method of characteristics (MOC) is a numerical method for solving the properties of a flow field. It is often used in nozzle design to determine the optimal contours for a device containing or directing supersonic flow to prevent shock reflections. In the method of characteristics, a fan of characteristic lines is started around an area of expansion. Looking downstream, if the lines originate from the right and are directed toward the left, they are considered left-running, and vice versa. The properties along the characteristic lines, including the flow angle and Mach number, can be found using compatibility equations. When designing a nozzle contour to avoid shock reflections, the wall angle at a certain point is set equal to the flow angle of the characteristic line that intersects the wall at that point. In axisymmetric flow, the characteristic lines are also Mach lines.

The cowling and spike for an axisymmetric aerospike nozzle may be a fully external or internal-external design (Fig. 1.10). Either design can be initially designed with an axisymmetric method of characteristics. This process assumes that the flow is

expanded to ambient pressure such that the boundary of the plume with the ambient flow (slip line) is parallel to the nozzle axis and extends from the cowling lip. Angelino gives a brief overview of using method of characteristics to design an aerospike contour. [26] Denton gives a detailed description on designing bell nozzles, fully external and internal-external aerospikes with method of characteristics. [27]

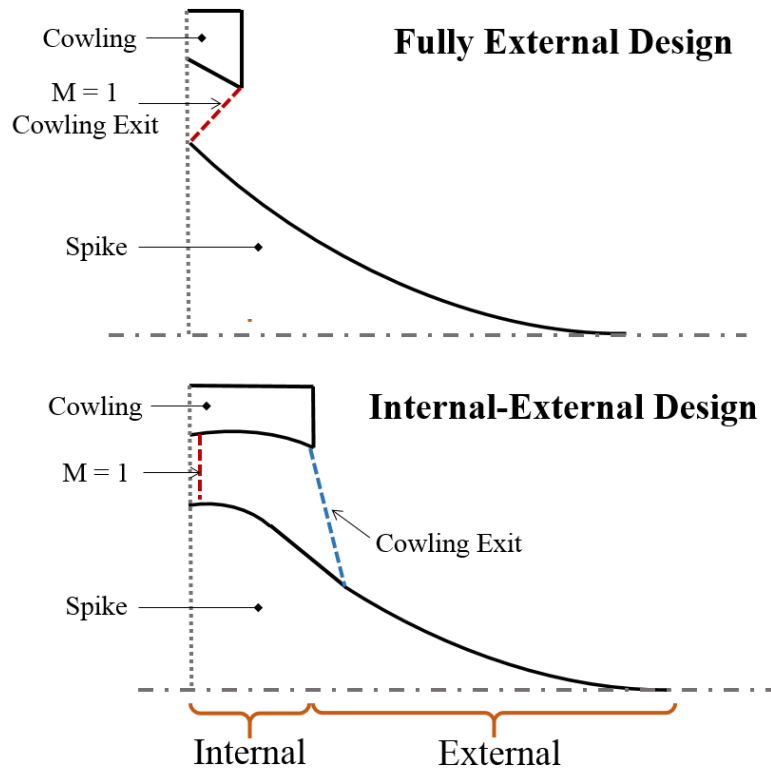


Fig. 1.10. Fully external and internal-external designs for aerospike nozzle.

The method of characteristics schematic for an internal-external design is shown in Fig. 1.11. [27] For the internal-external design, the first section designed is the internal section. The cowling and spike contours for the internal section are found in parallel. A sonic inflow condition is presumed and the internal contour is designed to turn and expand the flow to a prescribed cowling-exit Mach number determined by the designer. An origination point for the left-running characteristic lines is chosen by the designer as some distance of the inner radius up from the origin on the plane

of the throat. The characteristic line fan ends when the flow reaches the set cowl-exit Mach number. The last point for the cowl contour becomes the cowl lip. The external section of the spike turns the flow from the cowl-exit Mach to the final exit Mach, where the flow is turned parallel to the nozzle axis. The right-running characteristic lines for the external section originate from the cowl lip and extend from the top of the spike external contour to the nozzle tip. The internal and external sections of the spike contour are connected by a linear conical section. The spike contour may then be truncated as a certain percentage of its overall length.

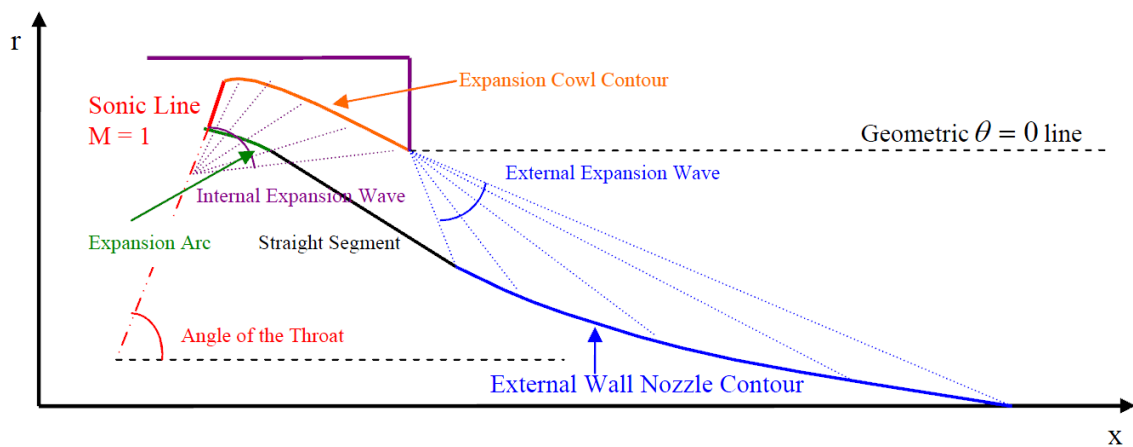


Fig. 1.11. Method of characteristics schematic for IE-aerospike nozzle. [27]

1.3.3 Flared Design

A flared aerospike design was proposed as an alternative to the IE-aerospike (Fig. 1.12). The flared aerospike is similar to the IE-aerospike, except that instead of internally turning the flow toward the centerline of the engine, the flow is only expanded within the cowl, driving the design of the flared cowl (Fig. 1.13). The flared aerospike was theorized to improve the performance over the IE-aerospike because it does not turn the flow supersonically in the cowl. The IE-aerospike cowl is de-

signed based on a singular ratio of specific heats; however, near the sonic point, the gas properties change drastically, including the ratio of specific heats. The single point ratio of specific heats cowl design for the IE-aerospike could cause shock losses. The outward-turning flared cowl is also a preferable geometry as the pressure thrust generated translates to a positive contribution, as opposed to the negative thrust contribution of the IE-aerospike's inward turning cowl. Additionally, the flared cowl provides a larger exit area, increasing the design NPR of the nozzle. A higher design NPR was thought to be beneficial because more of the RDE pressure cycle would be overexpanded, the regime in which aerospike are optimized.

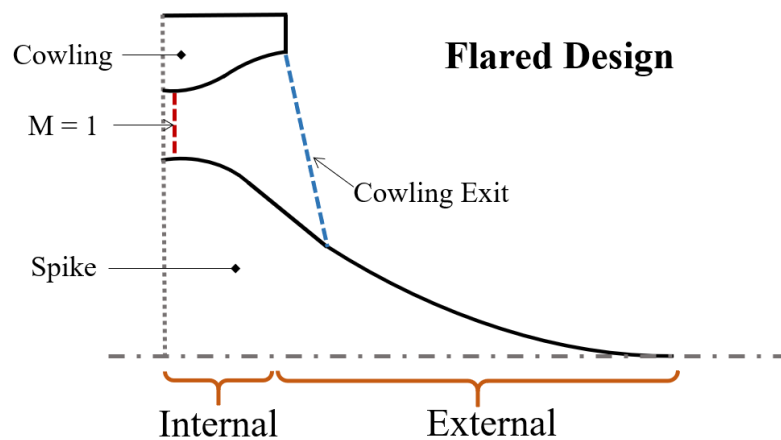


Fig. 1.12. Flared aerospike design.

1.4 Challenges to Aerospike Integration with RDEs

The periodic detonation behavior of RDEs and their geometry constraints create challenges that make it difficult to adapt any nozzle design. A few nozzle design candidates include de Laval, aerospike, and expansion-deflection nozzles. The aerospike nozzle integrates naturally into the annular topology of an RDE combustor and can adapt to changing NPR; thus, it is a leading candidate for application for these devices.

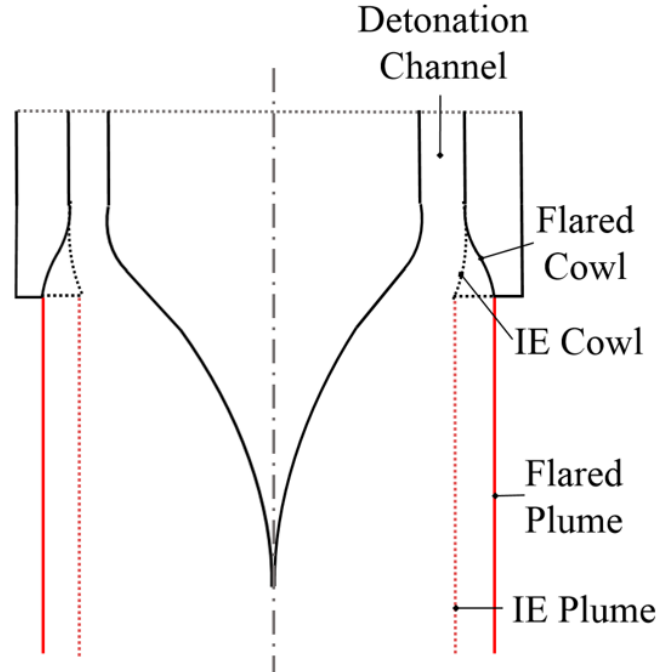


Fig. 1.13. Cross-sectional view of internal-external (IE) and flared aerospike designs. Dashed lines denote IE cowl and plume boundary at its optimal NPR while solid lines denote flared cowl and plume.

The production of a stable detonation wave is highly dependent on the geometry of the RDE combustor, including the inner radius and annular gap. The nozzle must be designed to a certain nozzle throat-to-exit area ratio to achieve the appropriate chamber-to-exit pressure ratio. For an aerospike, the throat area is defined as the annulus area and the exit area is defined as the area the radius of the cowling lip sweeps out. The cowling lip is often close to the outer radius of the annulus; thus, the RDE is often already designed with an area ratio, even before the nozzle is considered. The chamber pressure may not be adjusted for the proper pressure ratio for the area ratio, as it is often chosen for the desired mass flow rate.

Matching an aerospike contour design to its given area ratio provides additional challenges. Using the axisymmetric method of characteristics, an aerospike is typically designed to turn the flow from Mach 1 to the given exit Mach to match the

exit pressure to the ambient pressure. The actual geometry of the aerospike is highly dependent on the parameters given by the designer, including the cowling-exit Mach number and the origination point for the internal left-running characteristic fan. Thus, even while the nozzle may turn the flow to the correct exit Mach, the final point of the spike may not meet up with the engine centerline for the appropriate area ratio. It is important to design both the nozzle and engine together such that the throat and exit areas match for the designed pressure ratio, while making sure such a contour is achievable with an aerospike.

As the flow exiting the RDE is typically sonic or supersonic, it is important that the cowling turn the flow in such a way as to avoid shock losses. In the fully external aerospike design, the cowling turns the flow from the combustor to the Prandtl-Meyer angle associated with the desired exit Mach number. The cowling contour is not optimized for sonic flow. The internal-external aerospike design is better suited for an RDE because it turns sonic axial flow from the combustor with a cowling and aerospike designed to prevent shocks from forming.

While aerospikes benefit from pressure-adjusting behavior, it is always optimal to run the engine such that the slip line is parallel to the engine axis. Thus, it is critical to know the chamber pressure to design the nozzle. For RDEs, often the peak pressure is significantly higher than the mean pressure. More analysis is required to determine the optimal chamber pressure to design the nozzle. As stated before, aerospike nozzles typically perform at a higher efficiency when overexpanded than underexpanded. This may imply that it is beneficial to design to the highest pressure expected to be experienced; however, the transience of this peak pressure is such that the nozzle would perform off-design for a larger portion of the cycle than not.

1.5 Considerations for Nozzleless Geometries

When an RDE does not include a nozzle, the downstream face of the centerbody acts as a base region. Base regions are undesirable because the sudden expansion

causes the base pressure to drop significantly. This translates to lost pressure thrust that may have been captured by a plug surface. It is possible for the base pressure to even drop below the ambient pressure, resulting in base drag.

Most testing of RDEs is performed with a sizable base region. Models have been proposed to calibrate out the effect of base drag on the engine in post-processing; however, because of the transient nature of the RDE pressure wave, it is difficult to predict the base pressure in this region. To date, no rocket RDEs have been tested for a long enough duration that the RDE mode of operation has stabilized. Since steady-state has not been reached, the base pressure cannot be used to find an appropriate mean value (Fig. 1.14). This is a barrier to appropriately assessing the thrust potential of the RDE, separate from the nozzle design.

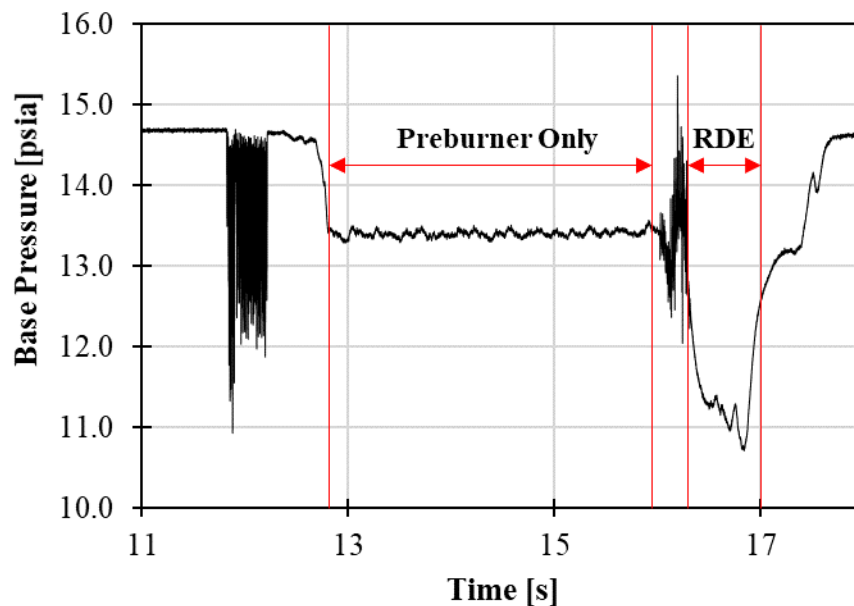


Fig. 1.14. Base pressure for rocket RDE test. [5]

Stechmann proposed a model to estimate the base pressure by approximating the flow to be constant at the average properties. The following relation was found to estimate the base pressure behind the centerbody for the nozzleless case, based on the mass flow rate and geometry: [10]

$$P_b = P_a - \frac{\dot{m}v_t(1 - \cos(\alpha))}{\pi r_b^2} \quad (1.1)$$

1.6 Study Objectives and Approach

The present study evolved from previous testing of a rocket RDE at Purdue University, both with an aerospike nozzle and without a nozzle. The primary goal of this study was to evaluate the performance benefit of using an aerospike nozzle using computational fluid dynamics (CFD). The results were intended to validate the experiment and to isolate the effect of the nozzle on the engine performance.

Chapter 2 describes the methods used for the computational portion of this study and the validation of these methods. The flow conditions from a Purdue RDE V1.3 test are described and used as the basis for this study. The computational domains and boundary conditions for the study are described in depth. The metrics used to evaluate the performance of each nozzle design are also detailed.

Chapter 3 details the computational results. In the first part of the chapter, the IE-aerospike, flared aerospike, and nozzleless geometries were evaluated. For each geometry, pertinent flow structures and loss mechanisms were identified. In the second part of Chapter 3, several different nozzle design parameters were evaluated with respect to their effect on the aerospike nozzle performance, including the channel length, internal expansion ratio, and wave number.

Chapter 4 shows the results of the RDE V1.3 and 1.4 experimental test campaigns. The computational performance results from Chapter 3 are compared to the experimental results from the V1.3 rocket RDE test campaign. Additional diagnostics were included in the V1.4 test campaign to more thoroughly compare to the computational results. The combination of the experimental and computational results from this study are aimed to provide a better understanding into appropriate nozzle design for rocket application RDEs.

2. COMPUTATIONAL FRAMEWORK

The following chapter provides a background into the computational methods used in this study. In Section 2.1, the nozzle geometries studied both in the experiment and the subsequent computational study are explained. Section 2.2 describes the solver used and validation studies for the application of interest. Sections 2.3-2.4 assess the fluid domain and go into depth on the boundary conditions. Section 2.5 describes the validation study on the turbulence model used, which is especially important to the nozzleless geometry. Section 2.6 details the mesh sensitivity studies. Section 2.7 details the computational parameters used. Section 2.8 details the methodology used for the results in Chapter 3 while Section 2.9 shows how the performance metric results were computed.

2.1 Geometries of Interest

The following CFD study is based on the experimental work of Stechmann's rocket RDE V1.3, tested at Purdue University. [10] Although two different detonation channel gap widths were considered, only the larger 0.30 in channel gap size will be considered in this study. The rocket RDE was tested without a nozzle – the nozzleless geometry – and with an IE-aerospike nozzle. A new aerospike geometry, the flared aerospike, was designed but was not tested until the RDE V1.4 test campaign.

2.1.1 Nozzleless Configuration

The nozzleless geometry is simply a blunt body, where no expansion surfaces have been attached downstream of the RDE exit plane (Figs. 2.1 and 2.2). Both the centerbody and the outer body act as base regions. While there are six hexagonal

bolt heads that protrude from the centerbody, these features were ignored for the purpose of simplifying the computation, as the pressure on the surface should equalize regardless.

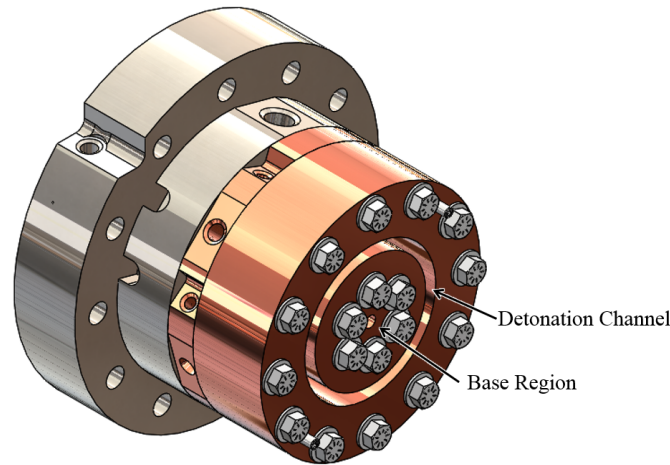


Fig. 2.1. Isometric view of nozzleless geometry for Purdue rocket RDE.

2.1.2 IE-Aerospike Configuration

The IE-aerospike geometry is similar to the geometry described in Chapter 1 (Figs. 2.3 and 2.4). The internal expansion, including the cowl and the upstream corner of the plug, was designed using the method of characteristics detailed by Denton. [27] Figure 2.5 shows the construction of the expansion fan using the MOC code and the corresponding streamlines in the internal expansion region. Based on the channel dimensions and final cowling diameter, the overall expansion area ratio was 3.01, for a design NPR of 13.7.

The plug, which is the inner surface of the external expansion region, was designed as a simple cone in order to keep the geometry somewhat generic. By using a conical shape, the plug does not expand the flow perfectly at the design NPR, risking some losses due to shock formation. The conical half-angle was chosen to be 22.57 degrees to achieve the appropriate expansion in the external section. It should be noted that

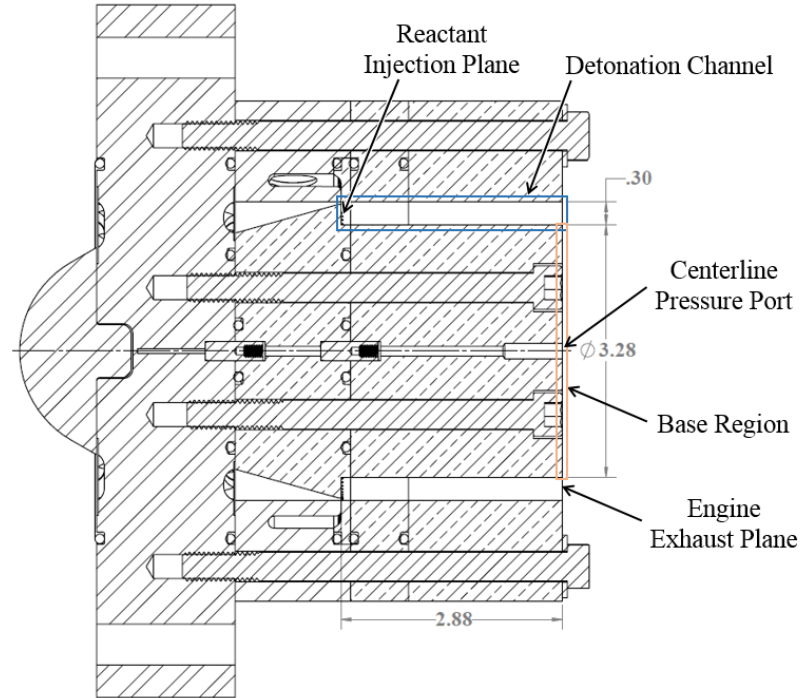


Fig. 2.2. Cross-sectional view of nozzleless geometry for Purdue rocket RDE.

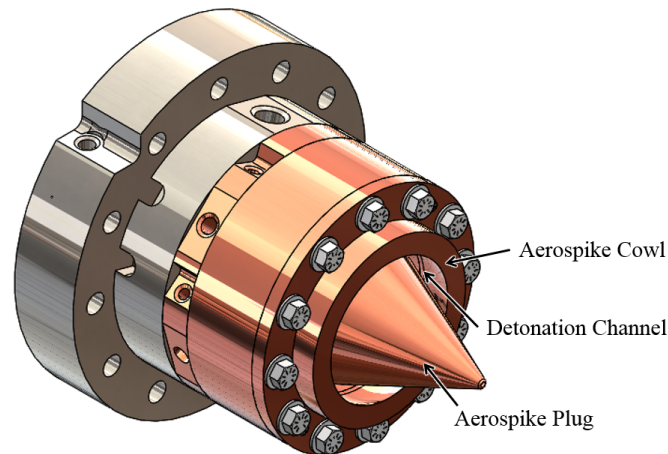


Fig. 2.3. Isometric view of IE-aerospike geometry for Purdue rocket RDE.

aerodynamic contouring of the nozzle is most important near and just after the sonic point, as the flow properties change rapidly and shock formation due to improper expansion is more likely to occur. As the internal expansion section, the region near

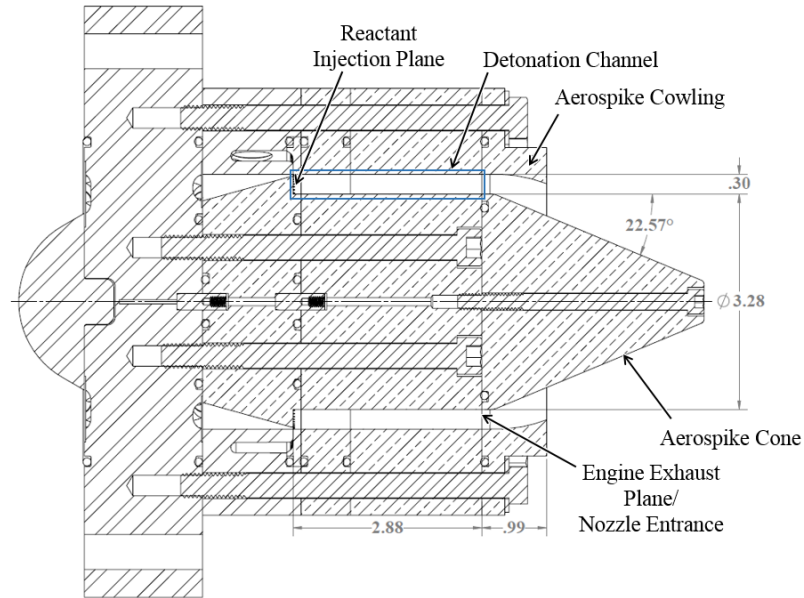


Fig. 2.4. Cross-sectional view of IE-aerospike geometry for Purdue rocket RDE.

the sonic point, is properly designed, the losses due to using a conical plug should be minimal.

2.1.3 Flared Aerospike Configuration

The flared aerospike geometry was designed using the NASA Aerospike Design and Performance Tool (ADAPT). [28] The ADAPT program has many design options and can be used to generate perfect and Rao aerospike contours. Design options include controlling the internal expansion area ratio and the tilt angle of the sonic plane. The ADAPT program also takes boundary layer formation into account in the nozzle contour generation. The ADAPT program is especially useful because it aligns the MOC generated curves for the internal and external expansion sections of the nozzle, which can be difficult to achieve. However, this limits the design inputs allowed, as some combinations of design inputs cannot generate realistic nozzle contours.

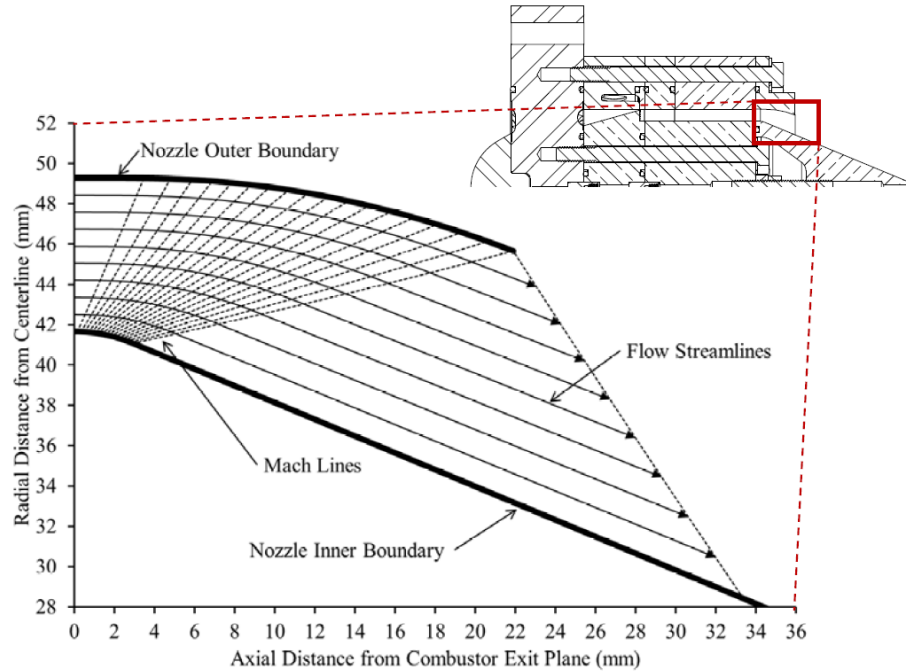


Fig. 2.5. Method of characteristics for internal expansion of IE-aerospike with linear cone of half-angle 22.57 degrees. [10]

The flared aerospike shown in Figs. 2.6 and 2.7 was designed with a Rao contour. A Rao contour is designed to maximize the thrust produced, but does not absolutely require parallel flow at the nozzle exit plane, as a perfect nozzle contour would. [29] As the internal expansion ratio dictates the final cowling diameter and thus the projected exit area of the nozzle, the internal expansion ratio directly affects the total expansion area ratio. While the flared aerospike geometry was chosen to explore higher total expansion area ratios, the channel outer diameter was already close to the external diameter of the engine, so the total area ratio was limited to the outer radius of the engine. To maximize the total expansion ratio while limiting the exit area within the engine footprint, the total expansion area ratio was 3.8, for a design NPR of 19.3. The internal expansion ratio was iteratively reduced until a minimum was found for an internal expansion area ratio of 2.1, for an internal pressure ratio of 8.5.

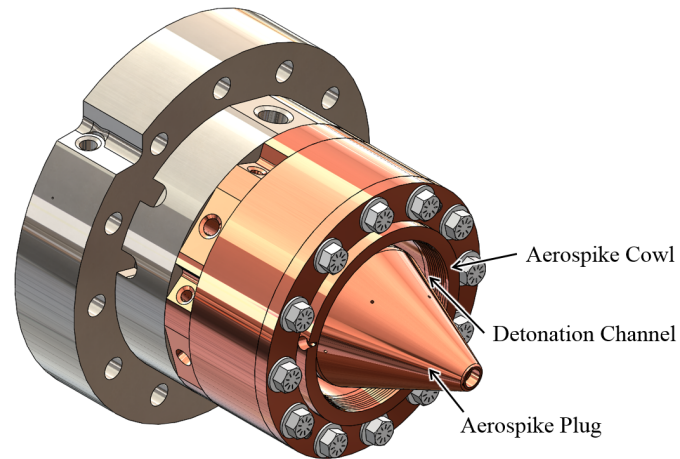


Fig. 2.6. Isometric view of flared aerospike geometry for Purdue rocket RDE.

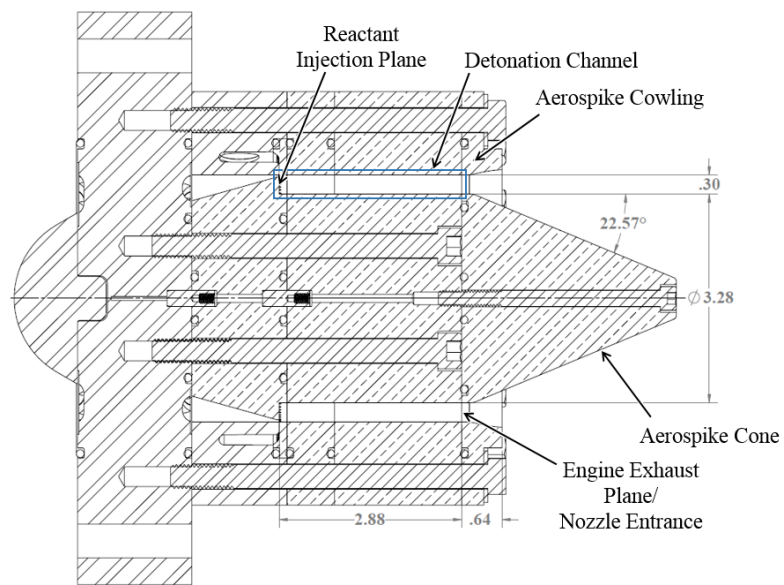


Fig. 2.7. Cross-sectional view of flared aerospike geometry for Purdue rocket RDE.

2.2 CFD Solver

Loci/CHEM was used for the CFD modeling in this study. Loci/CHEM is of interest because of its extensive historical use for nozzle flow computations, and specifically, aerospike nozzle computations, at NASA Marshall Space Flight Center (MSFC).

Loci/CHEM was created by Dr. Ed Lukes group at Mississippi State University [30] under contract to NASA MSFC and is maintained by this organization and the Tetra Research Corporation. This code is a fully-implicit, dual time solver with 2nd order accuracy in both time and space.

The Loci/CHEM code uses a declarative programming framework, where the program gives a description of problem, but does not dictate the method to run the solution. Instead of the user defining the computational parameters for the run, the code will automatically determine the optimal parameters. This allows the user to focus on the physical inputs instead of having to change the computational parameters for each run. [31]

An attractive feature of the code is its stability. The latest version of Loci/CHEM had great stability with nozzle flows in external flow fields. Previous work with the Generic Equation and Mesh Solver (GEMS), maintained by Purdue University [32], had difficulty with stability in over- and underexpanded nozzle flow cases. In these cases, the solution would develop for thousands of iterations and suddenly would become non-physical. Older versions of Loci/CHEM sometimes also had issues with stability. In contrast, the latest version of Loci/CHEM is stable for a large range of pressure ratios and transient pressure ratio conditions.

2.2.1 Solver Validation

Before Loci/CHEM was used for the RDE simulations, it was validated for aerospike flow physics using a different study case. The validation study was for a dual thruster case that had experimental results for a wide range of nozzle pressure ratios. [33] The two thrusters, stacked on top of each other, exhausted over a shared linear aerospike ramp (Fig. 2.8). Seven pressure transducers were placed at different axial positions along the plug. The experiment was conducted in a vacuum chamber and the back pressure was varied to achieve six different NPRs.

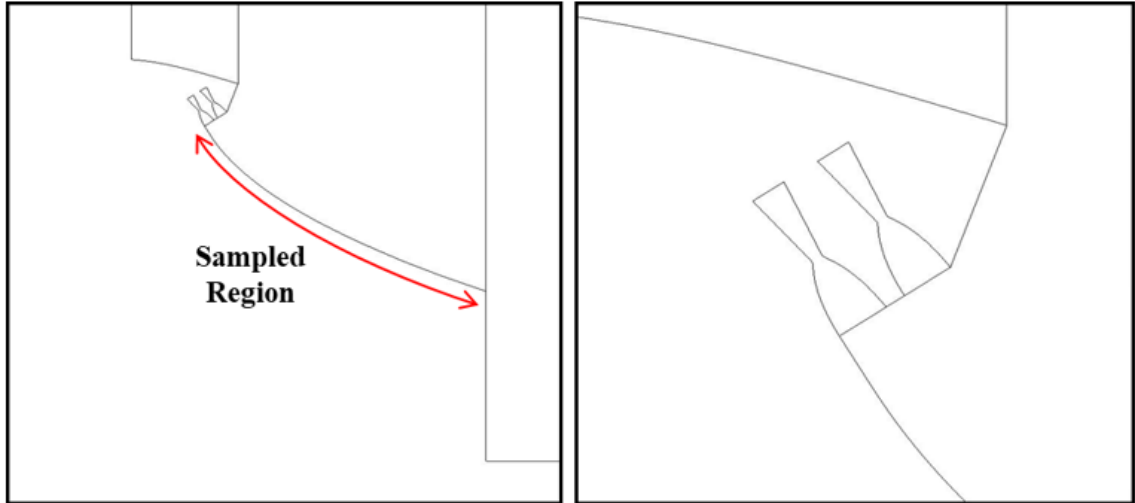


Fig. 2.8. Geometry of dual thruster aerospike experiment. Left, sample points were on aerospike plug. Right, close-up view of stacked thrusters. [33]

The results of the experiment and the computations are shown in Fig. 2.9. The pressure decreases initially as the bottom thruster expands on the plug. The large increase in pressure is due to the top thruster's impinging flow. Subsequently, the flow continues to expand and the pressure decreases down the length of the nozzle. For the higher pressure ratios, $\text{NPR} = 188$ to 289 , the surface pressures on the plug found by the computation agree well with the experiment. This result shows the computation is able to model the physical conditions with reasonable accuracy.

As the back pressure increases and the NPR decreases, flow separation occurs, indicated by the sudden increase in pressure on the downstream portion of the plug. Because of the poor spatial resolution of the pressure transducers, it is difficult to determine the point of separation in the experiment. However, in general, the point of separation occurs later in the computation than in the experiment. Additionally, the recovered pressure is lower in the computation than in the experiment. Later flow separation and lower pressure recovery equate to lower pressure forces on the plug and thus lower thrust computed in the simulation. In these overexpanded cases, the

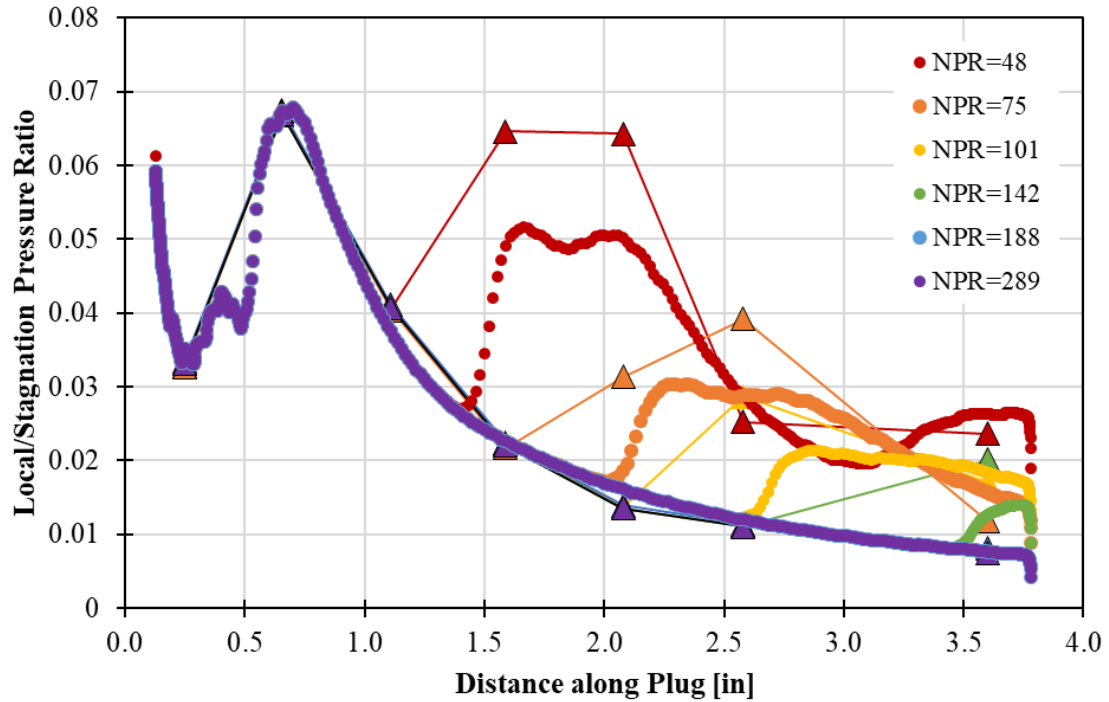


Fig. 2.9. Experimental (triangles) and computational (circles) results for different nozzle pressure ratios from dual thruster validation study.

CFD underpredicted the thrust by 2.5-5.0%. The negative bias of the computation for overexpanded conditions has important implications for the proposed computational study.

2.3 Computational Domain, Meshing, and Boundary Conditions

The domain for the three RDE geometries is based on the experimental testing conditions. The boundary conditions for the aerospike and nozzleless geometries are shown in Figs. 2.10 and 2.11. The domain was initialized at a sea-level ambient pressure of 1 atm, as the experiment was conducted at this back pressure. An external flow region was included to simulate the flow around the engine and to observe the interaction between the nozzle plume and the ambient fluid. The inlet to the external

flow is a pressure boundary condition set at the 1 atm ambient pressure and a flow velocity of Mach 0.05. The outlet of the domain was set to a pressure boundary condition slightly below ambient, 0.998 atm. The external flow inlet and outlet conditions were set as such to encourage a freestream low-speed flow, from the left to right. This low-speed freestream reduces the likelihood that induced pressure gradients caused at the beginning of the simulation corrupt the intended ambient conditions. The top of the domain was set to a far-field boundary condition and the centerline of the domain was a symmetry condition, as the geometry is axisymmetric.

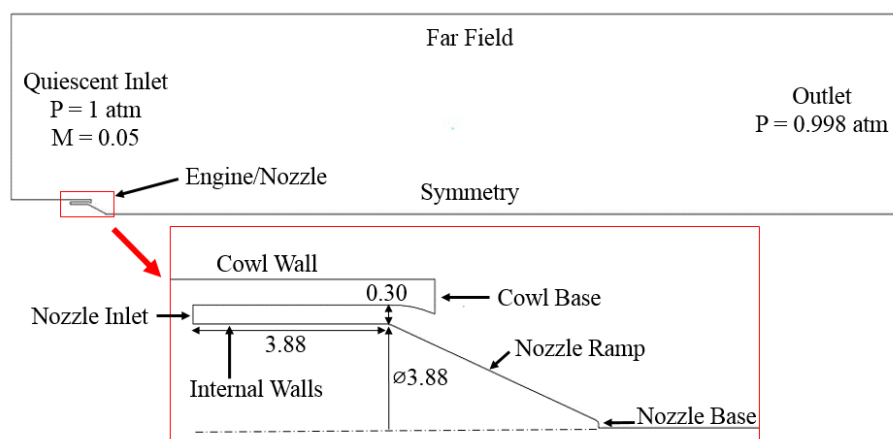


Fig. 2.10. Computational domain of aerospike geometry, dimensional units in inches.

The engine inlet condition was imposed on the entrance to the detonation channel, called the nozzle inlet. For the cases with a constant pressure/mass flow, the nozzle inlet was set to a constant mass flow boundary condition. When the pressure varied at the nozzle inlet, the nozzle inlet was set to a time-varying pressure boundary condition. The time-varying pressure boundary condition allowed multiple parameters to be specified as a function of location and time, including pressure, temperature, velocity, and turbulence parameters.

The detonation channel length was initially set to the same dimension as the centerbody diameter to provide enough length to ensure smooth flow conditions entered the nozzle. Just downstream of the nozzle inlet, a short length of the channel

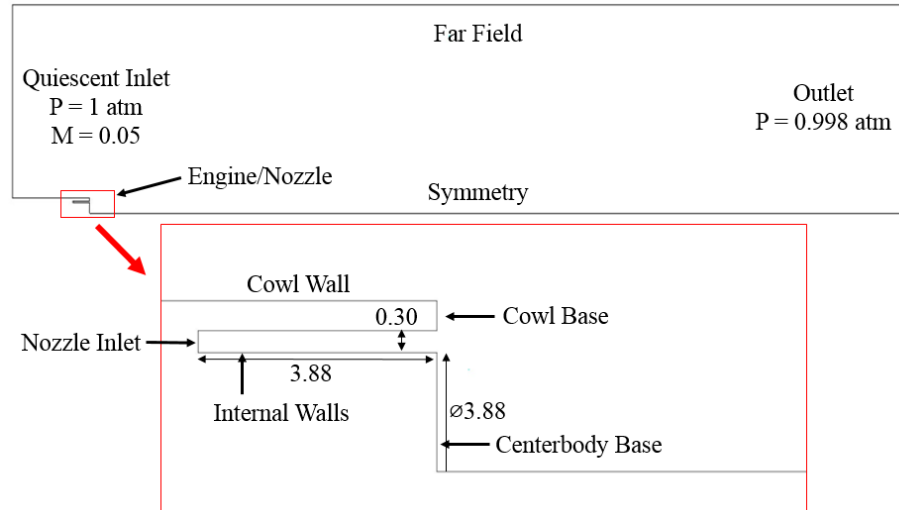


Fig. 2.11. Computational domain of nozzleless geometry, dimensional units in inches.

walls was set to a slip wall boundary condition allowing the inflow to adjust to the local pressure conditions before the no slip velocity gradients are enforced. This BC approach improves the stability of simulations with large pressure gradients just downstream of an inlet BC. The walls in the chamber after this slip-wall length are no-slip walls. For the aerospike geometries, the nozzle plug wall and corresponding base region, the cowl and corresponding base region, and the cowl wall exposed to the external flow were all set to no slip boundary conditions. For the nozzleless geometry, the centerbody and outerbody base regions and the cowl wall exposed to the external flow were all set to no slip boundary conditions.

2.4 Inflow Boundary Condition

The experimental hot-fire test result from Stechmann's Test #53 from the V1.3 test campaign were used to generate the nozzle inflow conditions for the computational cases. [10] The engine parameters from Test #53 are shown in Table 2.1. This test was chosen as the case study for the computation because it was a two-wave case

with good detonation stability, had high thrust performance, and had good quality high-speed video of the plume.

Table 2.1.
Purdue RDE V1.3 Test #53 Conditions

Propellants	Natural Gas & Oxygen
O:F Ratio	3.89
Total Mass Flow	1.15 [kg/s]
CTAP	8.6 [atm]
Thrust	2.3 [kN]
Wave Speed/CJ Velocity	88%
Wave Number	2
Frequency	13800 [Hz]

In all tests, the RDE operated with gaseous oxygen-natural gas (methane) propellants. The capillary-tube averaged pressure (CTAP) is a measure of the average pressure in the chamber and was 8.6 atm, or 125.5 psia, for Test #53. Direct measurement of the transient pressure in the chamber is practically impossible to capture without destroying the pressure sensor at the high pressure and temperature rocket conditions under study; thus, averaging techniques are the only method to gain a sense of the chamber pressure conditions. The oxygen-to-fuel ratio and total mass flow were determined by the conditions at the cavitating venturis in each propellant line. The Chapman-Jouget (CJ) velocity is the maximum theoretical speed of the detonation for oxygen/methane combustion. The wave-speed-to-CJ-velocity compares the measured wave speed of the detonation to the CJ velocity. This ratio was used as a measure of the efficiency of the detonation wave burning the propellants. The wave number and frequency were determined using high speed video and microphone recordings.

These CFD simulations do not directly compute the detonation of the reactants. Instead, time- and space-varying post-detonation gas conditions are specified at the

nozzle inlet. Results from a previous CFD study was used to generate the detonations pressure waveform. [34] This two-dimensional unwrapped simulation initialized detonation waves in a premixed zone of propellants. Once limit cycle behavior was achieved, the pressure profile at the detonation wave was extracted. An empirical curve fit of the 2D cases pressure profile showed a logarithmic equation best approximated the waveform.

The logarithmic waveform was then adapted to the physical conditions for Test #53 to estimate the detonation wave pressure profile. The propellants and oxidizer-to-fuel ratio from Test #53 was used to find the maximum possible pressure ratio of the detonation using NASA Chemical Equilibrium with Applications (CEA). [6] The wave-speed-to-CJ-velocity efficiency was then used to estimate a more realistic pressure ratio, which was 31.8. Using the CTAP pressure as the detonation time averaged pressure, the more realistic pressure ratio, and the frequency of the two wave case, the logarithmic waveform could be adapted to generate a theoretical waveform for Test #53. The pressure waveform generated can be specified both in time for a specific azimuthal location and azimuthal location for a specific time (Fig. 2.12):

$$P(t) = -630000 * \ln(t) - 5780000[Pa] \quad (2.1)$$

$$P(\theta) = -630000 * \ln\left(\frac{\theta}{180} * \frac{1}{f}\right) - 5780000[Pa] \quad (2.2)$$

The unsteady pressure waveform was employed in a pressure inlet boundary condition with only variation in the azimuthal direction and no variation in the radial direction. The pressure waveform is constant, but its location moves around the inlet, such that the pressure at a specific spatial location varies temporally (Fig. 2.13). In this way, the RDE departs from pulse detonation behavior, where the pressure profile only varies in time and not spatial location.

It should be noted that originally, the waveform was thought to be best modeled using an exponential decay waveform. This waveform was desirable because it is the theoretical solution to isentropic expansion of a gas through an orifice, which

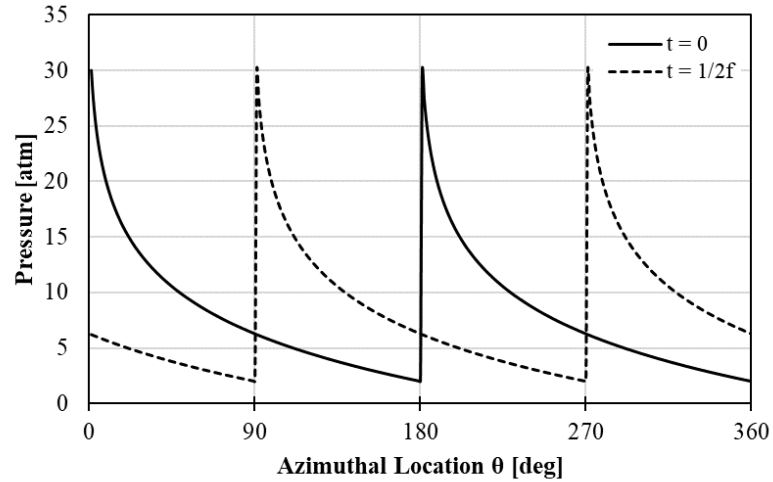


Fig. 2.12. Generated pressure waveform for Test #53 two-wave detonation at two different times: initial time and half period later.

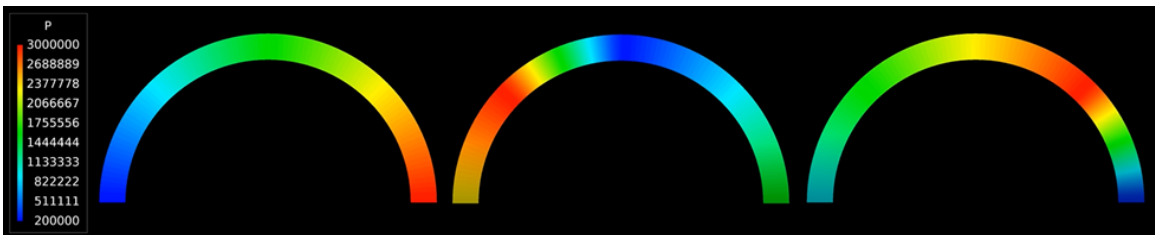


Fig. 2.13. Snapshots of pressure inlet at three different times in cycle. Pressure inlet imposed 3.9 in upstream from RDE exit plane. Pressure in Pa.

is a reasonable one-dimensional estimate of the blow-down process behind the detonation wave. However, the detonation wave expands both circumferentially behind the detonation wave and axially down the chamber. Thus, it is to be expected that the three-dimensional geometry would cause a faster rate of pressure decay, such as with a logarithmic curve, than an exponential curve. To date no appropriate theoretical model has been created to estimate the process of pressure blowdown behind a detonation wave in more than one direction.

Using NASA CEA, the remaining flow parameters were determined. The temperature for the inflow condition was set to the adiabatic flame temperature of 3400 K. Although the previous wrapped CFD case [34] found the temperature of the waveform was not uniform, the change was small enough that it was decided to use a constant temperature at all points. The flow was initialized with an axial velocity set to the sonic velocity of 850 m/s to simulate the flow velocity at the end of the detonation wave. This approach combines both test conditions and computed flow physics, which unfortunately leads to inconsistencies in the flow conditions between the two. For instance, because the pressure wave was set to achieve the CTAP of 125.5 psia, the actual mass flow rate through the simulation was 1.24 kg/s.

2.4.1 Gas Model

The computational studies used a non-reacting, real-gas mixture of detonation products for the working fluid. The Loci/CHEM chemistry database was used for the gas species thermal and transport properties. For instance, the specific heats of the species were a function of temperature. While in reality the gas exiting the engine would still be reacting, it was decided to neglect this effect for computational simplicity. Additionally, to date, chemical models involving detonation reactions are not as mature as those for constant pressure combustion. It should be noted that this simplification will possibly cause significant error when comparing to experimental results, as this study does. Much of this study compares computational cases to each other; in this instance, where the inflow conditions are kept consistent, the inherent errors in the gas model are acceptable.

The products species of the detonation combustion were determined using NASA CEA. [6] The mass-weighted percentages of the methane/oxygen detonation products are listed in the first column of Table 2.2. Those product species with 5e-6 fractions or less are not included by CEA and are not included in this work. While all of these species could be included in the gas model, it was desirable to use fewer species to

approximate the detonation products to reduce the computational complexity. To optimize the gas models specie mixture, an axisymmetric case with the IE-aerospike nozzle geometry was run using different species mixtures. The first case utilized all of the detonation product species shown in Table 2.2. Then, three more cases with successively fewer species included were considered. For each new model, the molar weighted percentages were redistributed such that their proportion to the remaining species remained the same. The specie mass fractions of these four gas models are provided in Table 2.2.

Table 2.2.

Mass weighted percentages for different evaluated specie models based on methane/gaseous oxygen detonation.

Specie	Full Detonation	5-Species	3-Species	2-Species
H ₂ O	33.6%	34.7%	43.5%	60.5%
CO ₂	21.9%	22.7%	28.4%	39.5%
CO	21.7%	22.4%	28.1%	
O ₂	9.8%	10.1%		
OH	9.8%	10.1%		
O	2.2%			
H ₂	0.6%			
H	0.2%			
HO ₂	0.1%			

Table 2.3 shows the normalized thrust error found with each species mixture. The normalized thrust is the thrust generated normalized by the stagnation pressure, as the stagnation pressure varied with the different gas properties of the specie mixture. The normalized error is the normalized thrust compared to the full detonation species thrust. It was found that the gas model with smallest number of species, the two species model with just H₂O and CO₂, had the lowest normalized error at 0.28%,

although the other two models also had reasonably low errors. The two species model was used for subsequent computations.

Table 2.3.
Normalized error compared to full detonation species for different species models.

Species Model	Normalized Error in Thrust
Full Detonation	
5-Species	0.58%
3-Species	0.52%
2-Species	0.28%

It is important to use an appropriate species mixture because of the effect of gas dynamics on the nozzle flow. The nozzle is designed for optimal expansion for a gas with a certain ratio of specific heats. Further, the gas properties change significantly near and at the sonic point. Both of these effects make estimating the gas properties especially important for computing the flow field in the internal turning section of the nozzle.

2.5 Turbulence Modeling

The turbulence model employed by the computational solver is used for determining the shear interactions in the solution and boundary layer development along nozzle surfaces. The most pronounced effect of the turbulence model is on recirculation region on the centerbody base for the nozzleless geometry case. Different turbulence models can significantly alter the calculated base pressure in this separated flow region. This significantly alters the calculated base drag (at low altitudes) and/or base thrust (at high altitudes). For this reason, a study comparing turbulence models was undertaken.

The nozzleless geometry was used for the comparative study to determine the effect of the turbulence model on the base region pressure. Five different turbulence models were evaluated: Wilcox k-omega (KW) [35], Wilcox 2008 revised k-omega (W08) [36], Menter k-omega baseline (BSL) [37], Menter k-omega shear stress transport (SST) [37], and Spalart-Allmaras (SA) [38] models. All models were evaluated with the Sarkar* compressibility correction, except the BSL model, which was evaluated with Sarkar [39], Sarkar* [39], and Wilcox [35] compressibility corrections.

Experiments with the nozzleless geometry were run with preheated oxygen at a constant pressure prior to the fuel being introduced. The base pressure at the centerline was recorded. This measurement is used because the base pressure reached a steady value during the oxygen flow. Base pressure did not reach a steady value during the RDE experiments, limiting its value for the turbulence model study.

A constant pressure condition was specified for the gaseous oxygen inlet boundary conditions. In the simulation, the base pressure was found as a function of radial distance from the centerline, as shown in Fig. 2.14. The single data point from the experiment is shown at the centerline position. The two criteria for evaluating the turbulence models were the variability in pressure and surface area averaged gauge pressure value. The BSL turbulence model with the Sarkar* compressibility correction had a relatively constant pressure profile with radial location compared to some of the other models. The surface area averaged base pressure for this model was 14.0 psia; compared to the test result of 13.4 psia; a 46% gauge pressure error. The two criteria were best met by the BSL Sarkar* turbulence model.

2.6 Meshing and Mesh Sensitivity Study

All meshes were constructed with Gridgen or Pointwise. The meshes for all geometries were constructed to capture the nozzle exhaust plume. A single plane of the aerospike and nozzleless geometry meshes is shown in Figs. 2.15 and 2.16. Near

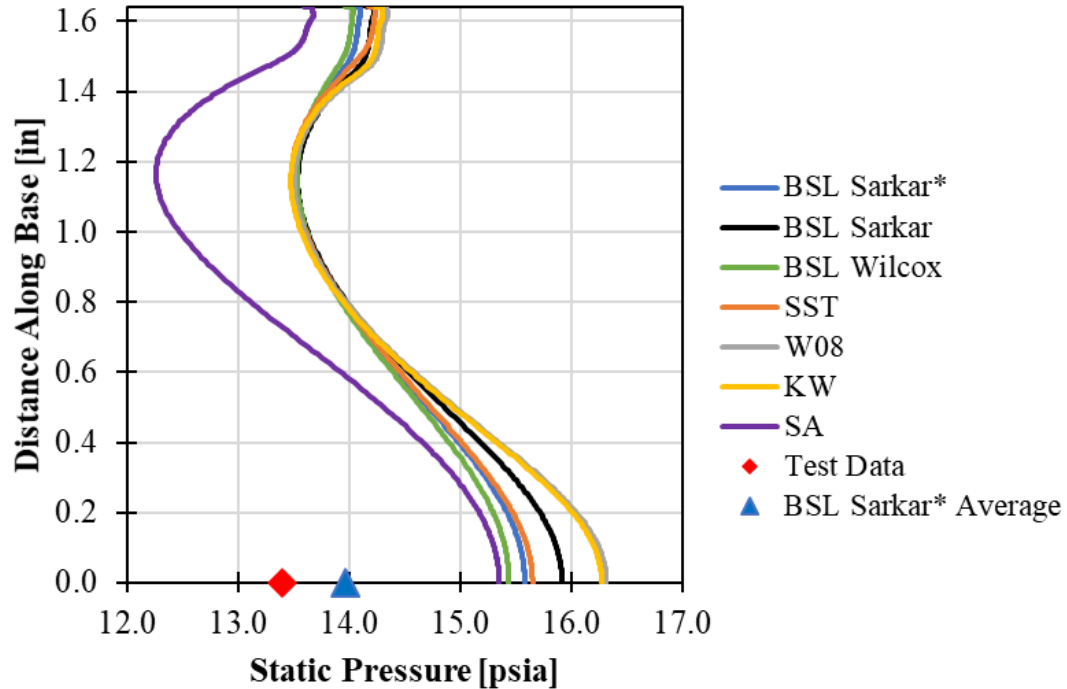


Fig. 2.14. Computational results of turbulence model comparative study including surface pressure as function of radial distance. Surface-averaged base pressure of BSL Sarkar* model was compared to test data.

the engine, quadrilateral meshes were employed. Away from the expected area of the exhaust plume, a tetrahedral mesh was incorporated to reduce the cell count.

In order for the turbulence model to capture the viscous sublayer of the boundary layer, the mesh near the walls must have an appropriate cell size and density. Two primary criteria were used to construct the mesh at the wall: the location of the first cell off of the wall needs to be close to $y^+ = 1$ and the mesh spacing off of the wall must be such that at least 20 cells are included up to $y^+ = 10$. These 20 or so cells are used to effectively discretize the viscous sublayer of the boundary layer. [40] Additionally, the growth rate of the cells needs to be gradual enough to prevent discontinuities in the boundary layer mesh.

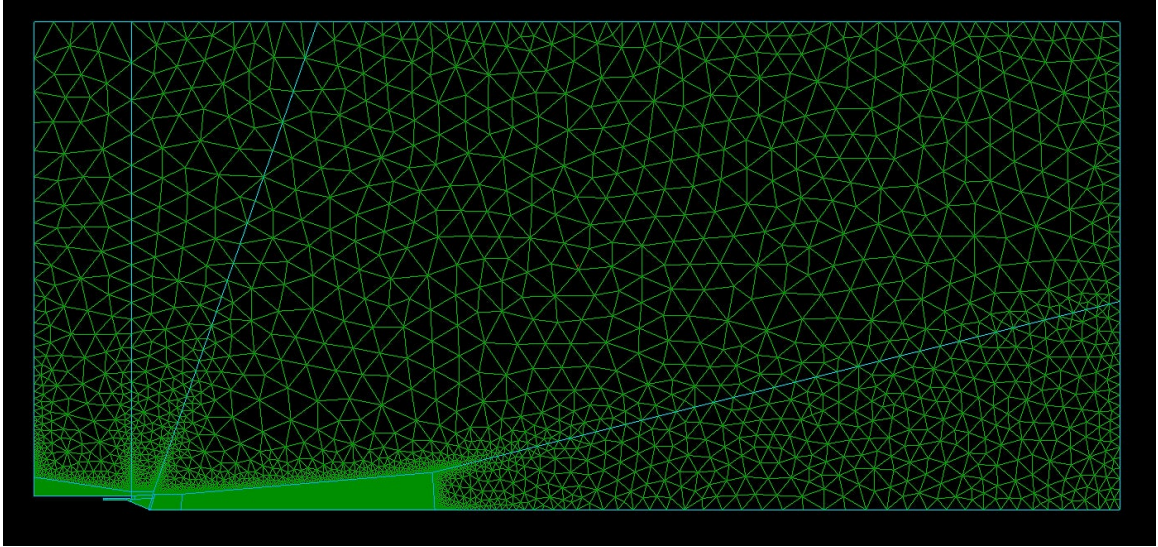


Fig. 2.15. Mesh for aerospike domain.

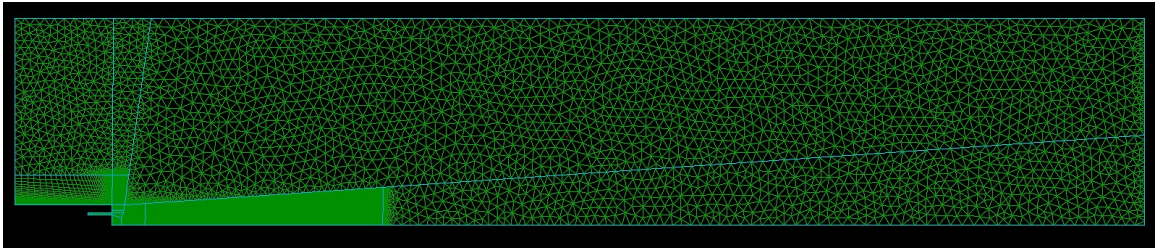


Fig. 2.16. Mesh for nozzleless domain.

An iterative method was used to construct the mesh near the walls. A steady-state computational case was employed on a preliminary mesh to determine the y^+ values at the walls. The size of the first cell off of the wall was then readjusted so that the maximum y^+ at any point along the wall was approximately 1. Four primary locations were examined as the maximum y^+ on the walls were expected at these points: the (a) nozzle inlet, (b) throat, (c) cowl lip corner, and (d) nozzle base corner. Figure 2.17 shows the first cell y^+ value and the delta distance of this first cell off of the wall for each of these critical locations for the finalized mesh. At least

twenty cells were included within the viscous sublayer ($y^+ = 10$). The growth rate of the cells at the wall followed a geometric function with a growth factor of 1.1.

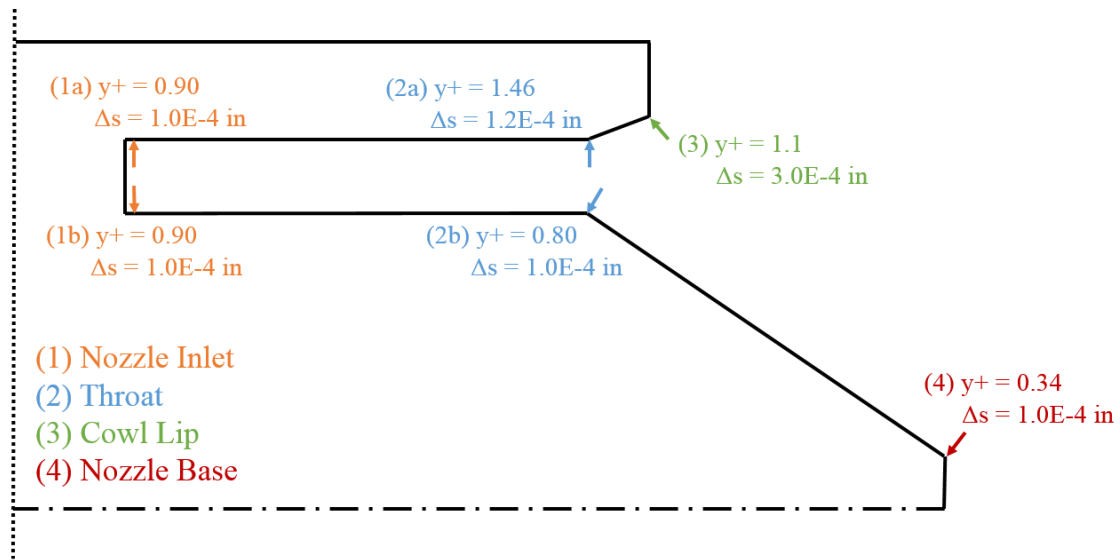


Fig. 2.17. Dimensional and y^+ distance of first cell off wall for four critical locations in aerospace domain.

A mesh sensitivity study was conducted for all three RDE geometries. The mesh sensitivity study aimed to reasonably eliminate the effect of the cell count and density on the results. Nominally three meshes were investigated, where the cell count was typically doubled with each refinement. All meshes were compared to the finest mesh investigated in terms of thrust to determine the optimal mesh that balanced mesh cell count and solution accuracy. The cases were run on axisymmetric geometries with a constant pressure inlet condition of 125 psia, the Test #53 CTAP.

Table 2.4 details the results of the IE-aerospike mesh sensitivity study. Four meshes were investigated: a coarse (lowest cell count), medium, medium with a refined base region, and fine mesh. While the medium mesh had the lowest error, the medium-fine base mesh was chosen for future study as it was determined that higher resolution

would be desired near the plug tip to capture the effects of flow separation on the nozzle.

Table 2.4.
Mesh sensitivity study for IE-aerospike domain.

Mesh	Number of Cells	Difference in Thrust from Fine Mesh
Coarse	67300	0.40%
Medium	269200	0.22%
Medium-Fine Base	345200	0.25%
Fine	1380800	

Table 2.5 details the results of the nozzleless mesh sensitivity study. Three meshes were investigated: a course, medium, and fine mesh. The error in thrust for the coarser meshes is relatively greater than that for the aerospike geometries. This is most likely due to a greater dependence on the centerbody base region flow field on the mesh size. Mesh sensitivity was not met; however, the 7.07% error in the medium mesh was deemed acceptable to limit the mesh size of the subsequent 3D meshes.

Table 2.5.
Mesh sensitivity study for nozzleless domain.

Mesh	Number of Cells	Difference in Thrust from Fine Mesh
Coarse	155720	8.56%
Medium	343500	7.07%
Fine *	586600	

Interestingly, when the finest mesh was used, the flow field changed from a steady-state solution to one that varied in time. Figure 2.18 shows snapshots of the oscil-

lating plume behavior for the finest mesh case. The frequency of the oscillation was approximately 400 Hz. The Mach diamond changes from an oblique shock seen in the steady-state solution for the coarser mesh to a normal shock. The normal shock periodically changes in size and strength over time. Perturbations can be seen in the shear layer between the nozzle plume and the external flow. These perturbations induce large vortices to roll off the shear layer and travel downstream.

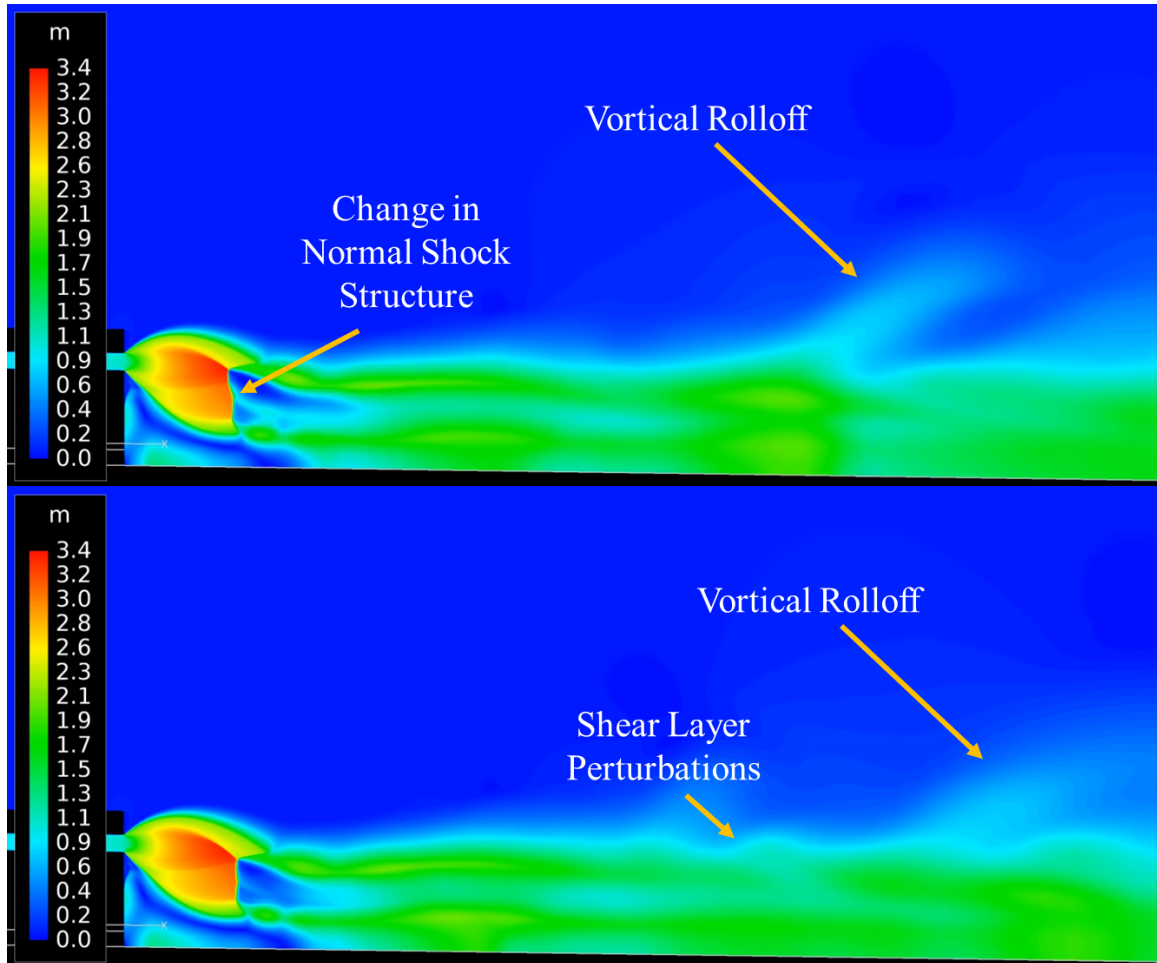


Fig. 2.18. Two snapshots of oscillating plume behavior for nozzleless geometry with high mesh resolution.

The exhaust plume oscillated periodically, even when the computation was run for hundreds of thousands of iterations. When the computation was switched from a

steady-state to a time-accurate, the same behavior was observed. After experimentation with refining the mesh between the medium and finest mesh, it was shown that there was some point in resolution where the solution changed in behavior. It was unknown at the time whether this effect was physical; after completing the 3D simulations with the steady state inflow condition, it was determined that the effect is real. It was decided to proceed with the medium resolution mesh to reduce the mesh size for computational simplicity.

Table 2.6 details the results of the flared aerospike mesh sensitivity study. Three meshes were investigated: a coarse, medium, and fine mesh. The medium mesh was chosen for future study.

Table 2.6.
Mesh sensitivity study for flared aerospike domain.

Mesh	Number of Cells	Difference in Thrust from Fine Mesh
Coarse	81011	0.20%
Medium	284935	0.03%
Fine	741249	

A sensitivity study based on azimuthal mesh discretization for the 3D meshes was conducted by reducing the domain to just the inlet and channel and imposing the time-varying pressure inlet. Three, two, and one degree divisions were investigated. It was found that the coarsest discretization allowable to capture the smooth transition of the pressure wave was a division every degree, or 360 azimuthal divisions.

The meshes shown in Figs. 2.15 and 2.16 are for the two-dimensional axisymmetric cases. These meshes were revolved around their respective centerlines to produce three-dimensional meshes for the IE-aerospike and nozzleless cases. The final cell count for each mesh was 41,767,560 and 31,486,020 for the IE-aerospike and nozzleless geometries, respectively.

2.7 Solver Parameters

The following sections describe the computational parameters for the different cases. These parameters are detailed in the Chem 4.0 User Guide. [41] It should be noted that all cases, excluding the time-varying cases, were run as first order accuracy from the beginning of the run until a reasonable solution was obtained. Afterward, all cases were run with second order accuracy to reach the final second order accurate solution.

2.7.1 Axisymmetric Steady Cases

The parameters for the axisymmetric steady-state cases are shown in Table 2.7. The cases utilized an Euler time integration, which is first order in time backward time integration with local timestepping. This time integration scheme is appropriate for steady-state cases, where the solution is independent of temporal changes. The relaxation parameter is used to control excessive swings in solution between time steps.

Table 2.7.
Computational parameters for axisymmetric cases.

Parameter	Value
Time Integration	Euler
Time Step	1e-6 [s]
CFL	50000
Relaxation	0.1
Newton Iterations	1
Gauss Siedel Iterations	3

2.7.2 3D Steady Cases

The parameters for the 3D steady cases are shown in Table 2.8. Although the boundary condition was steady, especially for the nozzleless geometry, non-steady solutions could develop. The time accurate scheme is a second order accurate 3-point backward time integration scheme. There were 3 Newton iterations per each time step and 5 Gauss-Seidel iterations, which is recommended for time accurate cases. For the time-accurate scheme, CFL and the relaxation parameter are not used.

Table 2.8.
Computational parameters for 3D steady-state cases.

Parameter	Value
Time Integration	Time Accurate
Time Step	1e-6 [s]
Newton Iterations	3
Gauss Siedel Iterations	5

2.7.3 3D Time-Varying Cases

The 3D time-varying cases were started from pre-existing solutions from the 3D steady cases. The parameters for the 3D time-varying cases are shown in Table 2.9. As the inlet condition varied with time, the computation was changed to time accurate. The time step was 1e-7 seconds for adequate time stepping within a wave cycle. For example, for a two wave case, there were 748 time steps in each cycle.

Table 2.9.
Computational parameters for 3D time-varying cases.

Parameter	Value
Time Integration	Time Accurate
Time Step	1e-6 [s]
Newton Iterations	3
Gauss Siedel Iterations	5

2.8 Study Approaches

2.8.1 2D Axisymmetric Time Average

Before starting with the full three-dimensional detonation wave model, it was decided to try to estimate the effect of the changing pressure inlet with a series of constant pressure axisymmetric cases. The detonation pressure waveform, described in Section 2.4, was discretized into eight pressures which constituted eight different nozzle pressure ratios. Each pressure was imposed at the nozzle inlet as a constant pressure boundary condition. Each case produced its own result, including thrust. Using the pressure waveform equation, the results from all eight cases could be time averaged to estimate the time average result from a full time-varying case (Fig. 2.19).

2.8.2 3D Constant Pressure and Detonation Waveform Model

Once a three-dimensional mesh was generated, the first set of cases imposed the average conditions from the detonation test case as input conditions; these cases are called the constant pressure/constant mass flow inflow condition. The inflow condition was set to the average mass flow of 1.24 kg/s with a temperature of 3400 K. The gas species entering the nozzle are the same as described in 2.4.1. These

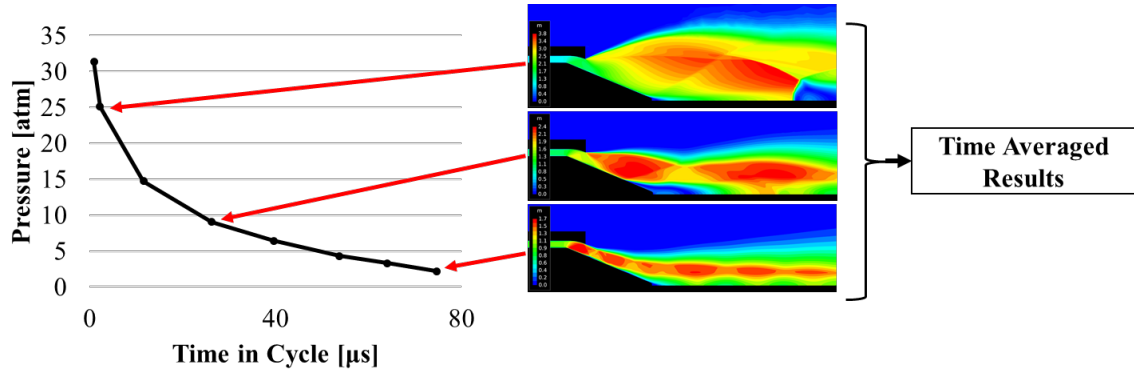


Fig. 2.19. Process for using axisymmetric cases at different pressure ratios to estimate RDE cycle time average result.

cases were used to validate the three-dimensional meshes and later, to compare to the performance of the detonation waveform model cases.

After the constant pressure cases, the full detonation waveform model was imposed onto the nozzle inlet boundary for the three-dimensional mesh. The waveform was imposed using a three-dimensional, time-varying input boundary condition.

2.9 Performance Metrics

The following metrics were used to assess the performance of the RDE for both the experiment and the computational results with the different aerospike and nozzleless geometries. The thrust for the computation was found by summing the momentum and pressure contribution from the nozzle inlet boundary and the pressure forces from the wall boundaries. The mass flow rate for all cases could be found from the nozzle inlet boundary. The specific impulse could then be found from the thrust and mass flow rate: [20]

$$I_{sp} = \frac{F}{\dot{m}g_0} \quad (2.3)$$

The ideal coefficient of thrust is the maximum possible thrust coefficient for using a specific nozzle design. It is a function of the nozzle pressure ratio and by extension, the area ratio, ambient pressure, chamber pressure, and ratio of specific heats:

$$c_{F_{ideal}} = \gamma \sqrt{\frac{2}{\gamma - 1} \left(\frac{2}{\gamma + 1} \right)^{\frac{\gamma + 1}{\gamma - 1}} \left(1 - \frac{1}{NPR} \right)^{\frac{\gamma - 1}{\gamma}}} + \epsilon \left(\frac{1}{NPR} - \frac{P_a}{P_c} \right) \quad (2.4)$$

The chamber pressure for the detonation wave case was assumed to be the time-averaged pressure. For an aerospike nozzle at NPRs below its design NPR, or when it is overexpanded, the exit pressure adjusts to the ambient pressure. The NPR becomes the chamber-to-ambient pressure ratio, and thus the pressure thrust correction in the coefficient of thrust equation is eliminated.

The delivered coefficient of thrust is a measure of the actual thrust produced by the device. It can be found from the measured thrust, chamber pressure, and throat area:

$$c_{F_{delivered}} = \frac{F}{P_c A_t} \quad (2.5)$$

The nozzle efficiency is the ratio of the thrust delivered to the theoretical thrust attainable for the NPR and is a measure of the quality of the nozzle design:

$$\eta_N = \frac{c_{F_{delivered}}}{c_{F_{ideal}}} \quad (2.6)$$

The specific impulse and nozzle efficiency were used to evaluate the performance of the different nozzle designs. The specific impulse is based on the mass flow, while the nozzle efficiency is based on the chamber pressure. Because of the transient nature of the pressure wave, it is difficult to understand the true average chamber pressure; thus, it may be more reasonable to use the mass flow based metric as the mass flow is constant over the cycle.

3. COMPUTATIONAL RESULTS

The following chapter details the computational study conducted on different RDE nozzle designs. In Section 3.1, the nozzleless geometry is evaluated with regard to the mechanisms of drag generation. In Section 3.2, the IE-aerospike geometry is evaluated with regard to thrust production. The performance of the IE-aerospike is compared to the nozzleless geometry in Section 3.3. In Section 3.4, the new flared aerospike geometry is evaluated and compared to the IE-aerospike design. Sections 3.5-3.7 encompass different parametric studies on the internal expansion ratio, wave number, and channel length of the nozzle and their effect on the performance.

3.1 Nozzleless Results

The nozzleless geometry was evaluated for two different flow conditions. The first flow condition employed a constant mass flow inlet condition, where the mass flow was set to the total mass flow obtained with the detonation wave case, 1.24 kg/s. The second flow condition was the transient pressure inlet condition, where the inlet utilized a three-dimensional transient pressure mapping derived from the two-wave detonation pressure profile. The results from these two studies are summarized below.

3.1.1 Performance Results

The two-wave detonation pressure profile was applied to two domains. The first domain was generated by rotating the axisymmetric two-dimensional mesh 180 degrees with 1 degree azimuthal discretization. Each side of the plane of symmetry used a periodic boundary condition such that the solution was mapped between the two planes. As the two-wave pressure profile is symmetric, the half domain could be

used with a pressure profile inlet that only models one of the waves at a time. The second domain included a full 360 degree geometry, generated in the same way as the half-domain. The full domain computation was used to determine the veracity of using the half-domain, as it was preferable to use the smaller mesh size half-domain to reduce the computation time. The constant mass flow inlet condition was also run with the half-domain.

The results of the constant mass flow inlet and two cases with the two-wave detonation pressure profile are summarized in Table 3.1. The inflow conditions for the constant mass flow and detonation pressure cases are described in Chapter 2. The results for the half domain with the two-wave detonation pressure profile vary from the full domain by less than 1% in terms of force, coefficient of force, nozzle efficiency, and specific impulse, so it was determined that using the half domain with the single symmetric wave profile was valid.

Table 3.1.

Performance results of nozzleless geometry with constant mass flow inlet and two-wave detonation pressure profile.

Inlet/Domain	Mass Flow [kg/s]	Stagnation Pressure [atm]	Force [N]	c_F	η_N	I_{sp} [s]
Steady State / Half Domain	1.24	10.1	2376	1.07	0.84	195.0
2 Wave / Half Domain	1.24	10.2	2187	0.97	0.76	179.6
2 Wave / Full Domain	1.24	10.4	2202	0.96	0.75	180.3

The specific impulse increased by 7.5% for the constant mass flow condition versus the detonation wave profile. This result is surprising; although no aerodynamic surface exists to capture the exhaust thrust effectively, it was still theorized that the

detonation wave profile would produce thrust more efficiently due to the enhanced thermodynamic efficiency of the cycle. The following discussion on the flow features and base pressure for the nozzleless geometry will elucidate the inherent drawbacks of using the detonation wave pressure profile with a blunt body geometry.

3.1.2 Flow Features

To orient the reader, Fig. 3.1 shows the computational solution for the nozzleless geometry for the detonation wave case at an instant in time. The pressure on the engine inlet and centerbody inner surface shows the detonation wave travelling around the annulus. The cross-sectional plane is plotted with the Mach contour of the channel and exhaust plume.

The first step in understanding the drag generation mechanisms of the nozzleless design is to analyze the flow structure for both the steady state case and the detonation wave profile. In both the constant mass flow and detonation wave profile cases, drag is generated due to sub-atmospheric pressures formed on the base region because a nozzle exit cone is not present. It is important to characterize this effect as many experiments employ this nozzleless configuration when studying the combustion process. As seen in the figures below, the plume expands into the regions behind the centerbody and cowl bases. The radial expansion of the plume implies that some of the momentum is directed radially, causing a reduction in thrust. Additionally, there are no surfaces for the plume to expand against, so the pressure in the plume is not translated to additional pressure thrust.

Although the constant mass flow case used a constant fluid property inlet, a 7400 Hz oscillation (period of 130 μ s) was observed in the axial force when running the simulation as time accurate. Figure 3.2 shows snapshots of the Mach contour for the exhaust plume at two different points in the observed cycle period; the time step between each snapshot is 80 s. As the plume expands against the ambient pressure, a barrel shock develops as the plume is recompressed. From the change in the two

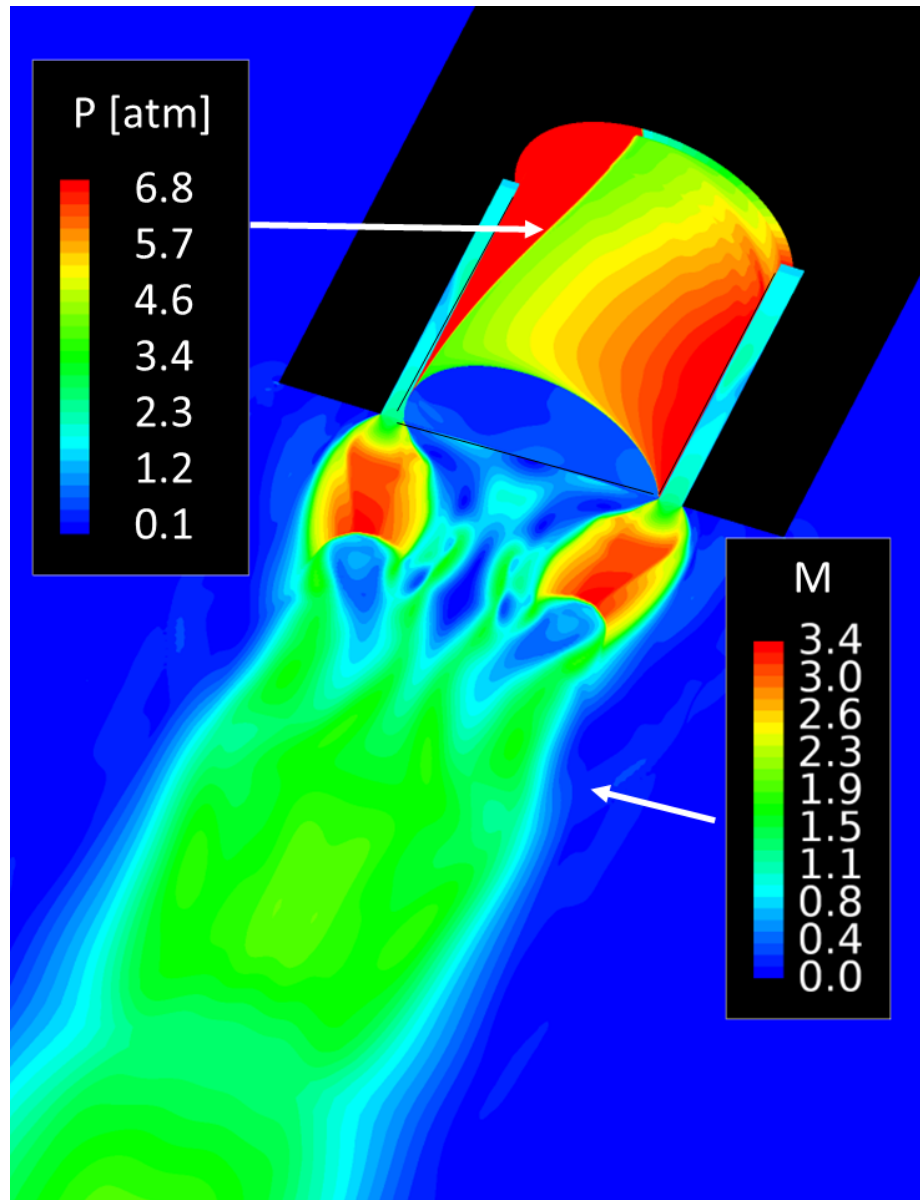


Fig. 3.1. Instantaneous pressure contour of RDE inlet and inner detonation channel surface and Mach contour of channel exhaust plume on symmetry plane for nozzleless geometry with detonation wave case. Detonation pressure wave is imposed on inlet end of the annular combustion chamber 7.0 cm in length with gap of 0.7 cm. Diameter of combustion chamber is 9.9 cm.

snapshots, it is apparent that the strength of the barrel shock changes over this 7400 Hz cycle. The oscillation is associated with a 13 N change in axial force on the

centerbody base. The engine exit absolute pressure between the two snapshots is 0.566 and 0.573 atm respectively, a change of 1.2%.

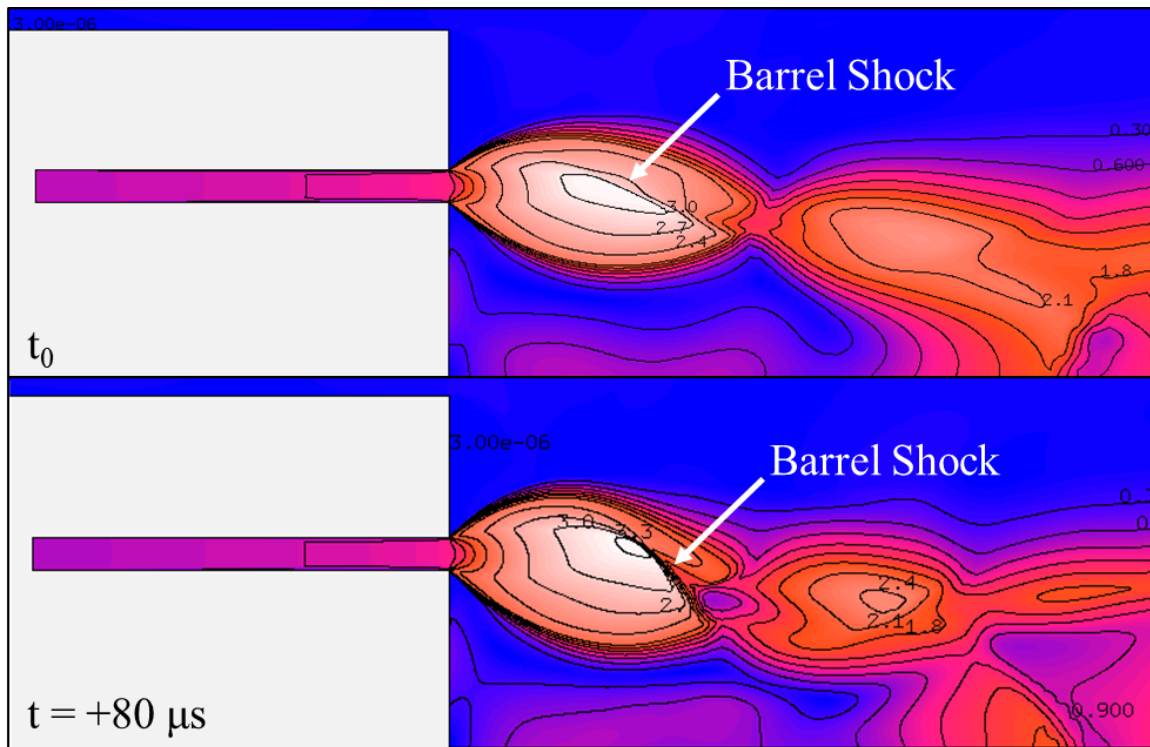


Fig. 3.2. Cross-sectional view of nozzleless geometry at one azimuthal location of exhaust plume Mach contour for two different times for constant mass flow case.

Compared to the constant mass flow case, the detonation wave profile case experiences a more dramatic change in its exhaust plume. The frequency of the oscillating wave was 13700 Hz for a cycle period of 75 μs . Figure 3.3 shows snapshots of the Mach contour for the exhaust plume at three different points in the detonation wave cycle; the time step between each snapshot is 25 μs . The pressure contour at each time step show the progression of the wave peak in the combustor.

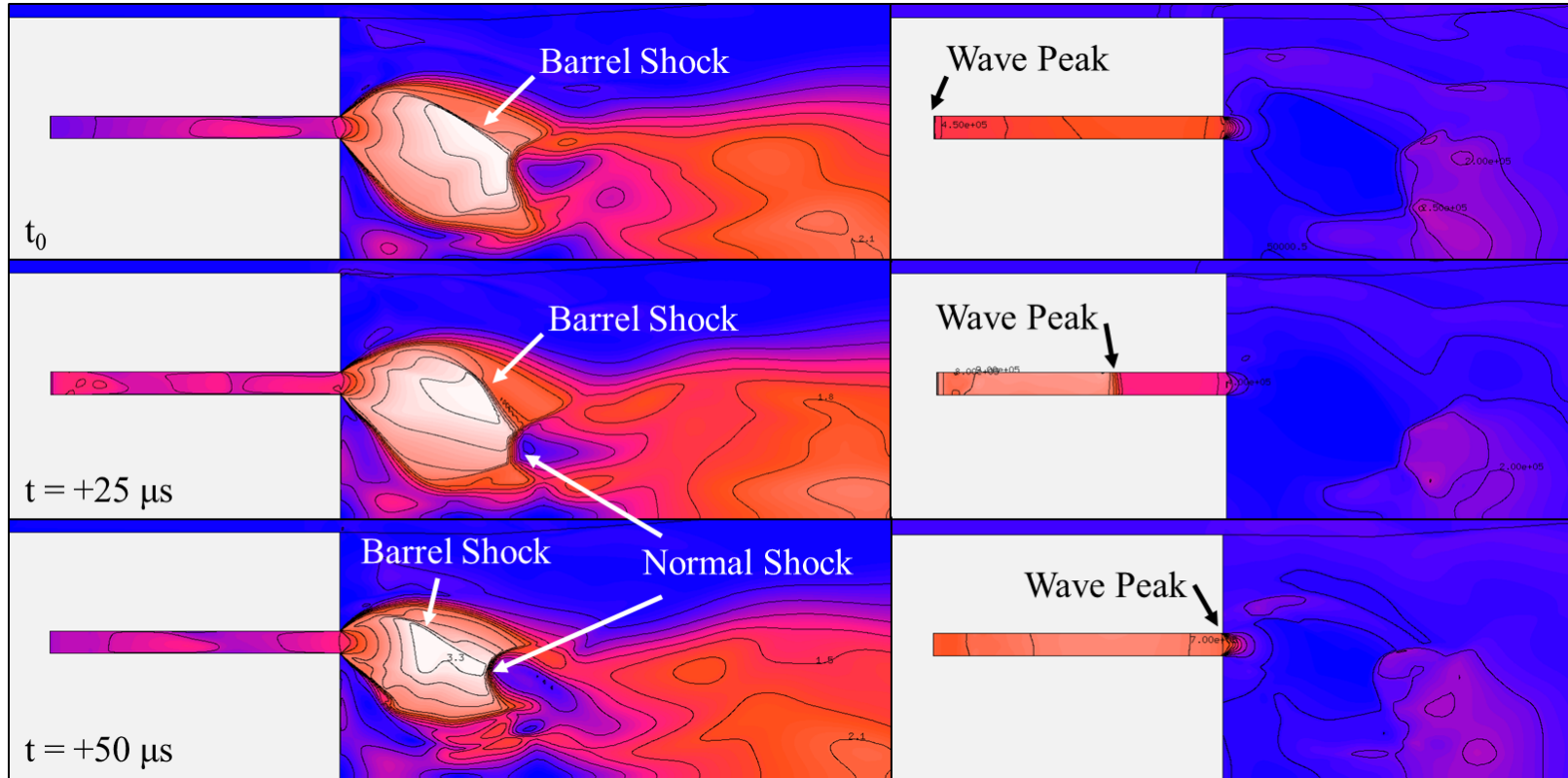


Fig. 3.3. Cross-sectional view of nozzleless geometry at one azimuthal location of exhaust plume Mach (left) and pressure (right) contours at three different times in detonation wave cycle. Pressure measured in Pa.

The drag production due to the oscillating plume dynamics is unique to the detonation wave profile for a blunt body geometry. It is immediately apparent that the exhaust plume changes significantly between each snapshot in the cycle. The most prominent feature in the plume is the changing bow shock and downstream shock formation.

In the first snapshot, the lowest pressure gases of the cycle are exhausting the engine. At this point, the plume has a "V" shaped set of oblique shocks that intersect at the downstream end of the barrel shock. This shock structure is relatively low strength at an incoming Mach number of 2.4. In the second snapshot, the highest pressure gases at the high point in the detonation cycle are midway through the detonation channel. The barrel shock strengthens and a normal shock starts to form at the intersection of the oblique shocks. When the high energy gas reaches the engine exit in snapshot 3, the normal shock grows in strength with an incoming Mach number of 3.3. The barrel shock by this point almost disappears, suggesting the normal shock structure dominates at this point in the cycle. As the cycle continues, the plume returns to the weaker set of oblique shocks and reforms the bow shock.

The normal shock develops in the detonation wave case, but not the constant mass flow case; this normal shock enhances the total pressure losses in the exhaust plume compared to the constant mass flow case. While the presence of the normal shock alone causes loss in thrust, an additional loss mechanism exists due to the drastic oscillation of the plume in the axial direction. This loss mechanism is best understood by evaluating the pressure profile on the centerbody base region.

3.1.3 Base Pressure Contribution

For tests that do not employ a nozzle, the main thrust loss mechanism at low altitude operation for both the constant mass flow and detonation wave profile cases is due to the base drag on the centerbody region. The exhaust plume effectively acts as an ejector on the base region. The momentum of the plume causes shear

interactions with the fluid in the base region and effectively suction fluid from this region. As the fluid is suctioned from centerbody base, a recirculation region forms at sub-ambient pressures.

The main difference in thrust between the two cases is due to the change in the base drag. The base drag increases by almost 10 times in the detonation wave case versus the constant mass flow case. Figure 3.4 shows the base pressure as a function of radial location for the constant mass flow case (solid) and the cycle time-averaged results for the detonation wave case (dashed). The surface averaged base pressure is shown for both cases (dotted). As the flow recirculates, a stagnation point is formed at the centerline, as apparent by the high local pressure at this point. As the flow expands radially outward from the stagnation point, it accelerates and drops in local pressure. The flow then encounters the exhausting flow from the lip of the base and decelerates, increasing the local pressure again. The surface area averaged base pressure for the detonation wave case is 0.59 atm, significantly lower than the base pressure for the constant mass flow case of 0.95 atm, with an 800% decrease in the average gauge pressure. This sharp decline explains the increase in base drag for the detonation wave case.

To understand the stark increase in base drag with the detonation wave case, it is useful to look at the instantaneous pressure on the base. In the constant mass flow case, the pressure is relatively constant over time; in contrast, the pressure in the base region for the detonation wave case strongly varies with time. Figure 3.5 shows the base pressure profile as a function of radial location for the same three temporal snapshots as Fig. 3.3. While the centerline pressure is essentially constant, the pressure at greater radial locations – where the integrated pressure force is more significant than at the centerline – significantly varies between the time steps. Figure 3.6 shows the pressure contours at the centerbody base for the same temporal snapshots as Fig. 3.3.

As evidenced by Figs. 3.4 and 3.6, the base region is not experiencing a constant suction force from the exhaust plume as in the steady-state case. In the detonation

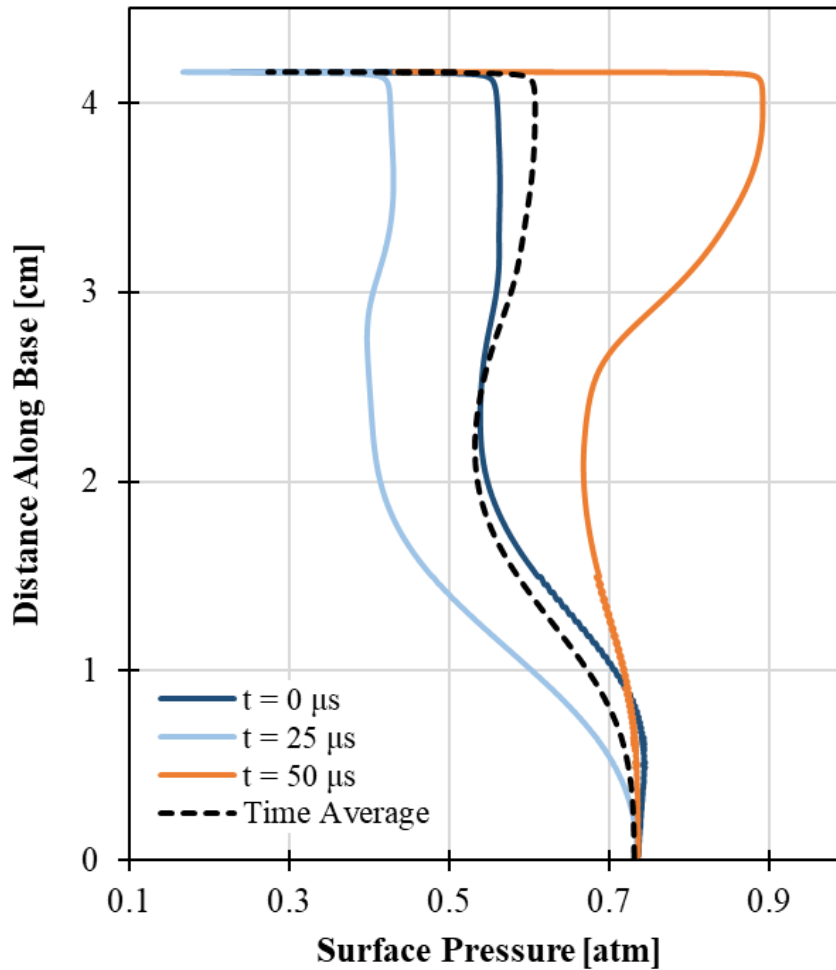


Fig. 3.5. Base pressure profile as function of radial distance for same azimuthal slice at three different times in detonation wave cycle. Cycle time averaged base pressure profile also shown.

at the same average (CTAP) pressure. Using Eq. 1, the base pressure for the Test #53 flow conditions was predicted to be 0.65 atm. Compared to the constant mass flow result of 0.95 atm, this prediction shows that the base region is experiencing enhanced suction. However, there is a 15% difference in gauge pressure from the full detonation wave case result. For this reason, it is important to include base pressure measurements in RDE combustion chamber experiments if one is hoping to properly correct the measured thrust for the base drag generated.

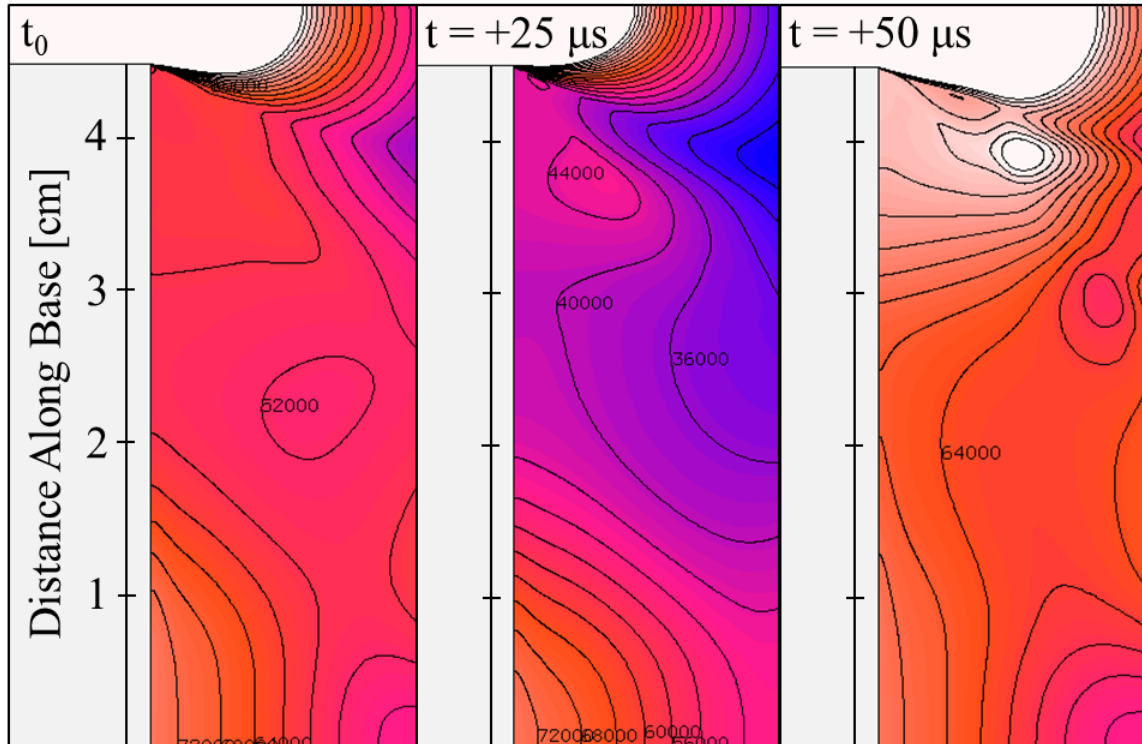


Fig. 3.6. Pressure contours at base region for same azimuthal slice at three different times in detonation wave cycle. Pressure in Pa.

3.2 IE-Aerospike Results

Similar to the nozzleless cases described above, the IE-aerospike geometry was evaluated in two different flow conditions: the constant mass flow inlet condition and the two-wave detonation pressure profile. The results from these two studies are summarized below.

3.2.1 Performance Results

Like the nozzleless cases described above, the two-wave detonation pressure profile was applied to the half- and full-domains. The steady-state mass flow inlet condition was run with the half-domain.

The results of the constant mass flow inlet and two cases with the two-wave detonation pressure profile are summarized in Table 3.2. The results for the half domain with the two-wave detonation pressure profile vary from the full domain by less than 1% in terms of force, coefficient of force, nozzle efficiency, and specific impulse, so it was determined that using the half domain with the single symmetric wave profile was valid.

Table 3.2.
Performance results of IE-aerospike geometry with constant mass flow inlet and two-wave detonation pressure profile.

Inlet/Domain	Mass Flow [kg/s]	Stagnation Pressure [atm]	Force [N]	c_F	η_N	I_{sp} [s]
Steady State / Half Domain	1.24	10.2	2594.2	1.16	0.90	212.9
2 Wave / Half Domain	1.24	10.2	2609.8	1.16	0.90	214.3
2 Wave / Full Domain	1.24	10.4	2617.4	1.15	0.89	215.4

The specific impulse was modestly improved by 3% using the detonation wave condition versus the constant mass flow condition. This improvement, while partially explained by the thermodynamically improved detonation wave cycle, is not as drastic as expected. The following discussion on the flow features and ramp thrust for the IE-aerospike geometry will elucidate some of the losses encountered with the IE-aerospike geometry.

3.2.2 Flow Features

To orient the reader, Fig. 3.7 shows the computational solution for the IE-aerospike geometry for the detonation wave case at an instant in time. The pressure on the engine inlet, centerbody inner surface, and nozzle cone shows the detonation wave travelling around the annulus. The cross-sectional plane is plotted with the Mach contour of the channel and exhaust plume.

Figure 3.8 shows the surface pressure plot and particle flow path on the combustor inner surface and aerospike plug. As apparent from Fig. 3.8 and observation of video of the entire cycle, the plume does not respond immediately to the passage of the detonation wave; instead, the wave is communicated at the local sound speed. The peak of the pressure wave is apparent from the stark contrast in the surface pressure contour plot. In the chamber, the pressure exiting the combustor lags behind the wave imposed at the chamber entrance; this is to be expected, as the pressure wave is communicated at the speed of sound of the detonation products. The rate of lag increases with the chamber length as viscous effects slow the pressure wave further.

The pressure wave interface experiences a change in behavior once the flow exits the chamber and expands onto the plug surface. Indeed, the pressure wave interface has an inflection point where it appears to race ahead of the pressure wave in the chamber. There are two possible explanations. The first is the effect is due to the reduction in perimeter as the wave moves axially along the cone. The azimuthal velocity is maintained, hence the rotation rate of the interface increases. The second explanation is the formation of a separation region at the end of the nozzle cone. The separation region is shown with the velocity iso-surface in Fig. 3.9; the velocity iso-surface plotted is a small negative velocity. The tortuous pressure wave interface is notable because it means that a simple azimuthal cut of the exhaust flow will have a more complicated flow structure than possibly suggested by the instantaneous pressure ratio at that azimuthal location.

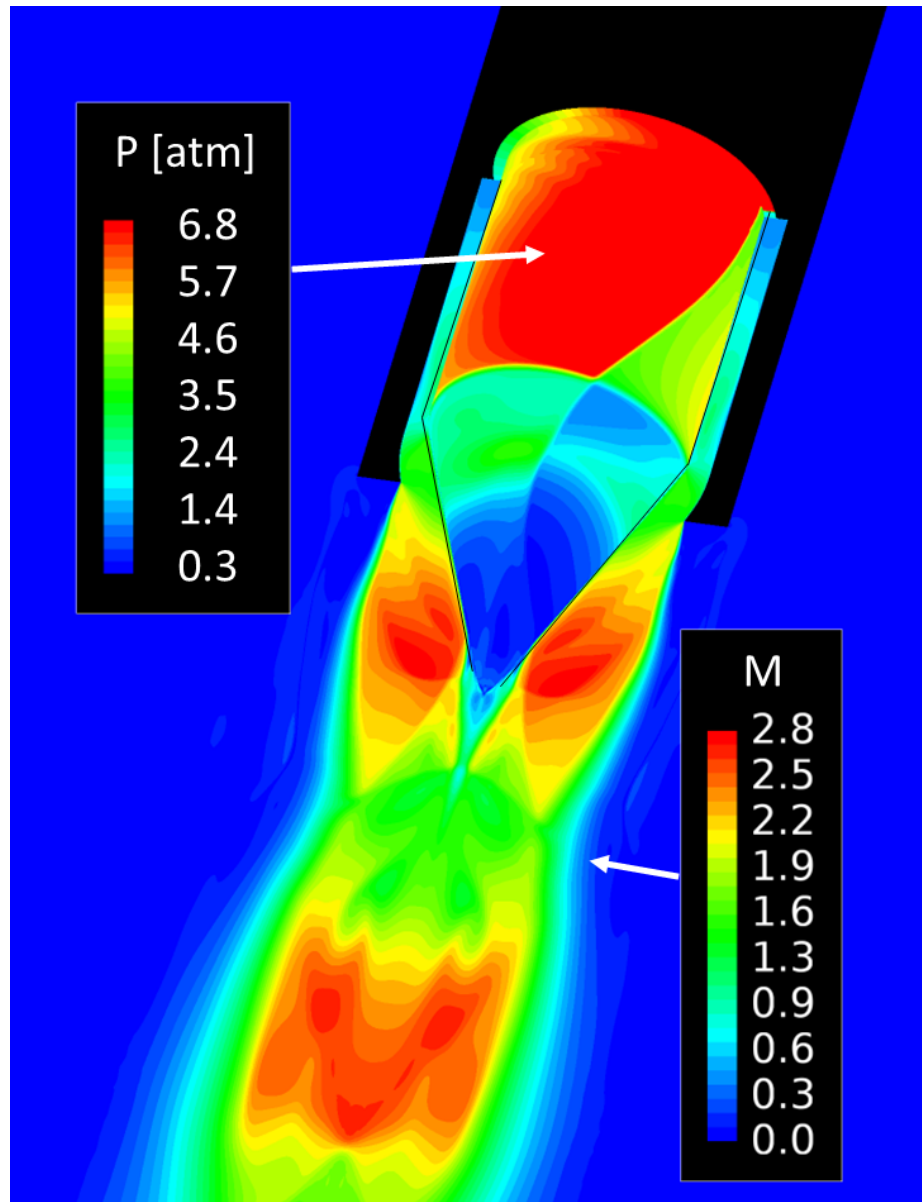


Fig. 3.7. Instantaneous pressure contour of RDE inlet and inner detonation channel surface and Mach contour of channel exhaust plume on symmetry plane for IE-aerospike geometry with detonation wave case.

The rotating detonation wave has a significant effect on the plume structure for the IE-aerospike geometry. Figure 3.10 shows the Mach contour at three time steps in the cycle period; the pressure contour at each time shows the progression of the

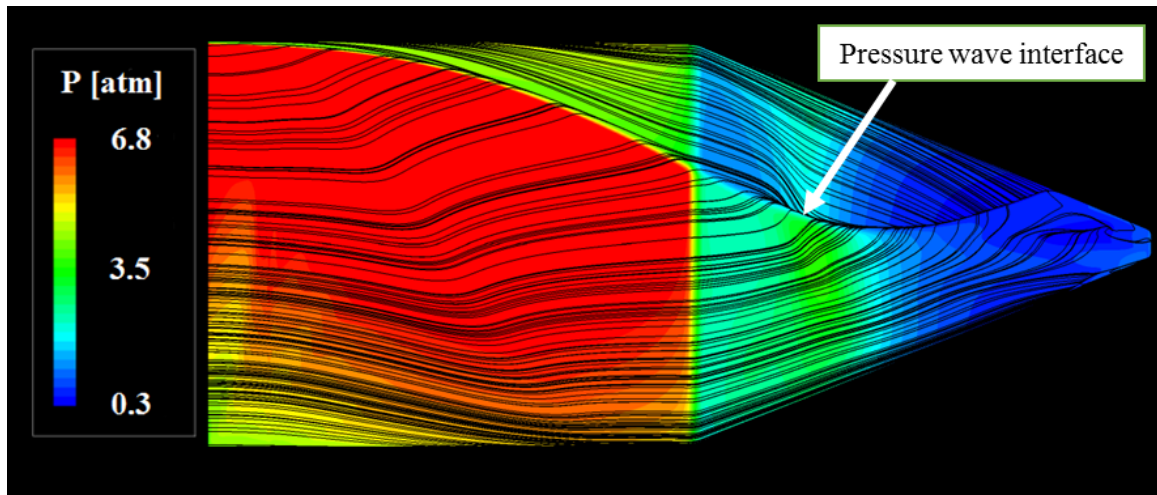


Fig. 3.8. Pressure contour and particle flow path plot on surface of RDE inner chamber and aerospike plug. Pressure wave is imposed on the left-hand boundary and flow moves downstream to the right. Wave rotation direction is from bottom to top.

detonation wave peak. From the first to second snapshot, the high pressure gases have exhausted off of the nozzle and the flow expands. As the pressure of the wave decreases, the flow separation point is shown to move closer to the engine exit plane. In snapshot three, the high pressure gases are reintroduced to the plug; these high pressure gases re-energize the plume and move the separation point down the length of the nozzle.

The three snapshots in Fig. 3.10 show that the detonation wave has a significant effect on the location of the flow separation point. The flow separation point is the location where the flow adjusts to the ambient pressure conditions. Pressure recovery on the aerospike plug surface is important to prevent thrust loss due to sub-atmospheric pressures. The next section will address how the effect of the detonation wave on the flow separation point affects the overall thrust.

It is interesting to note that while the pressures entering the nozzle change significantly over time, the general plume footprint is roughly constant and looks optimally

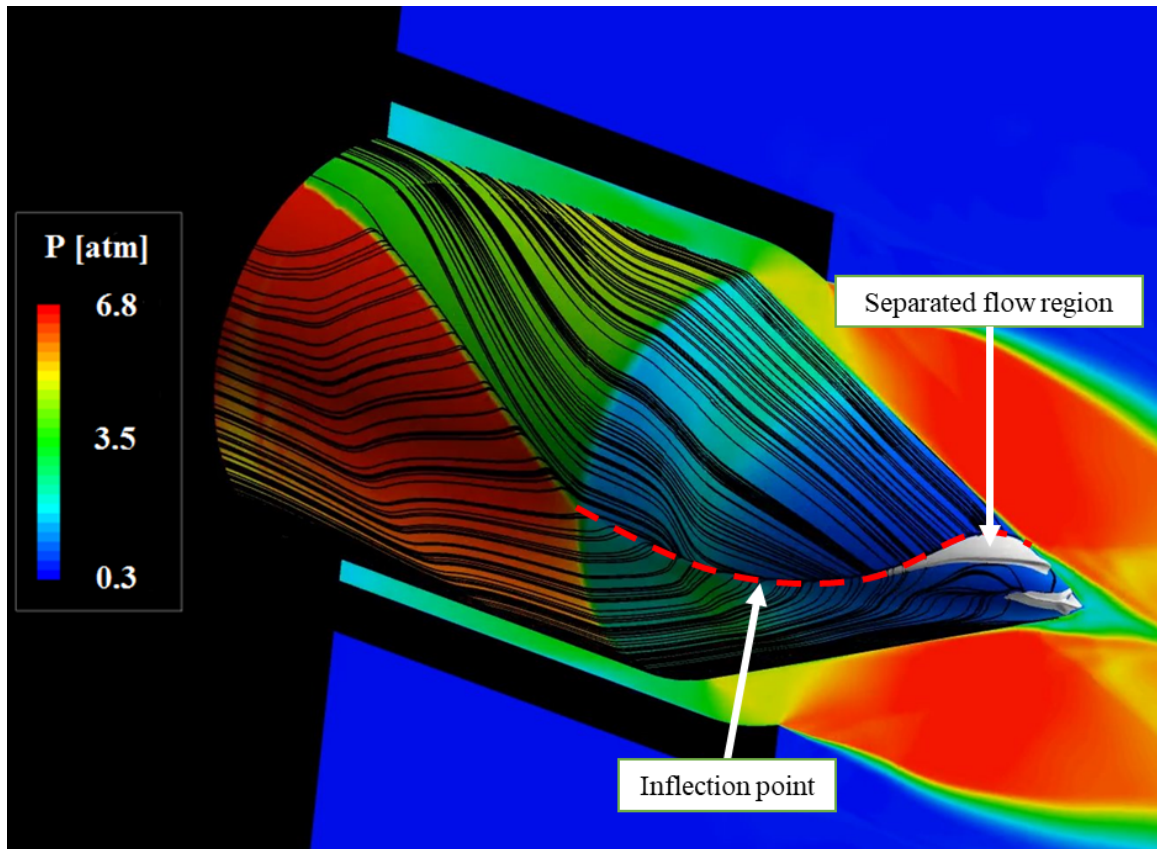


Fig. 3.9. Isometric view of pressure contour and particle flow path plot on surface of RDE inner chamber and aerospike plug. Pressure wave interface on cone shown with red dashed line.

expanded in Fig. 3.10. This suggests the design NPR of 13.7 for this aerospike geometry probably produces optimal expansion for the detonation wave profile considered.

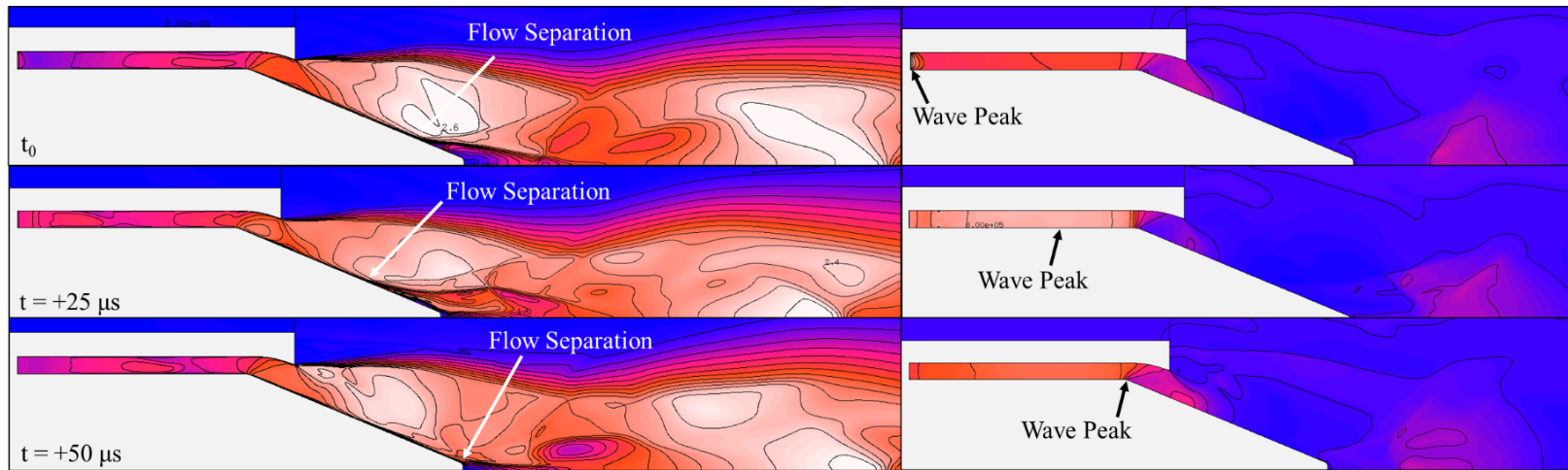


Fig. 3.10. Cross-sectional view of IE-aerospike geometry at one azimuthal location of exhaust plume Mach (left) and pressure (right) contours at three different times in detonation wave cycle. Pressure in Pa.

3.2.3 Ramp Thrust Contribution

A significant portion of the pressure thrust generated by the IE-aerospike nozzle is from the plug/ramp, making it one of the most important aerodynamic surfaces in the geometry. The distribution of pressure along the ramp is essential to understanding the pressure thrust gained – or lost – due to geometry or inflow conditions. Figure 3.11 shows the surface pressure profile as a function of axial distance along the ramp. The time-averaged solution for the detonation wave case (dashed) is compared to the constant mass flow case (solid). For both cases, the surface pressure decreases initially until it reaches a section of increasing pressure. Prandtl-Meyer expansion waves from the cowl interact with the plume, causing recompression on the plug surface. The flow then continues to accelerate down the plug and the pressure decreases once again. In the steady-state case, the surface pressure suddenly increases half-way down the plug. This point is where flow separation occurs due to the local adverse pressure gradient imposed on the boundary layer and pressure is recovered on the surface. In contrast, in the time-averaged solution of the detonation wave case, flow separation is delayed until further down the plug.

Typically designers of de Laval nozzles try to avoid flow separation near the exit of the nozzle caused by overexpanded flow. Since the surface area of the de Laval nozzle increases near the exit of the nozzle, the flow separation has a large effect on the forces on the nozzle. Flow separation in these cases is an unstable phenomena that can cause large amplitude oscillations. A good example of this phenomena is the structural vibration of the RS-25 engine nozzles during the start-up transient. [42] However, flow separation theoretically can improve nozzle performance, as the pressure recovery increases the pressure thrust on the nozzle. Since the surface area decreases near the nozzle exit plane, the flow separation does not have as great of an effect as the de Laval geometry, so the flow separation in the constant mass flow case may be tolerable.

To understand the cause of the delay in flow separation for the detonation wave case, it is useful to look at the instantaneous pressure plots at different points in the

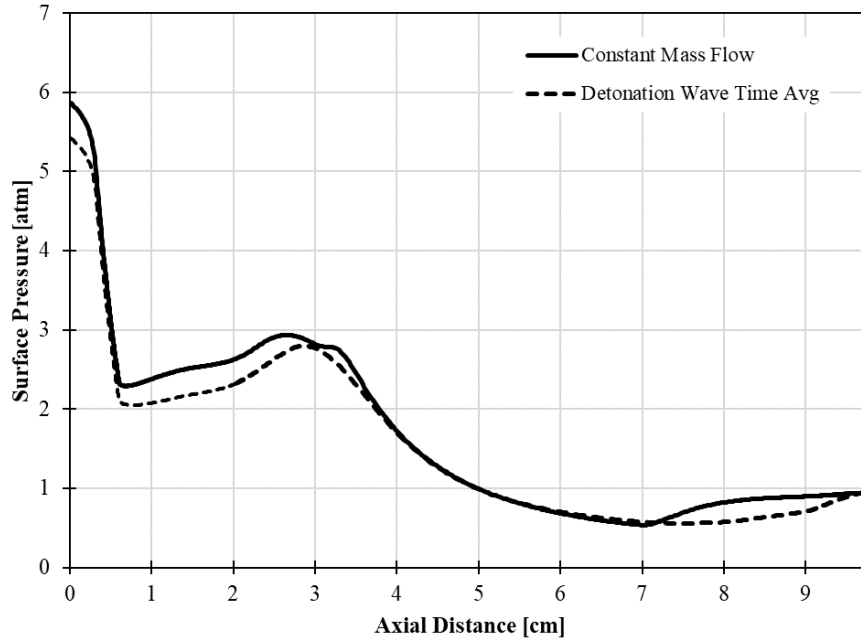


Fig. 3.11. Surface pressure on IE-aerospike plug for constant mass flow and time-averaged result of time-varying detonation wave inflow as function of axial distance. Cowl exit plane at 2.5 cm.

wave cycle. Figure 3.12 shows the surface pressure normalized to the incoming flow pressure as a function of the axial distance for an azimuthal slice along the plug for three different times in the detonation wave cycle. These times correspond to those shown in Fig. 3.10. The time-averaged solution is also shown (dashed). The surface pressure was normalized in order to more easily discern trends in flow features.

Two features are readily apparent from the normalized surface pressure plots. The first is that the recompression at the beginning of the plug moves axially and changes in intensity. As the incoming pressure changes, the Prandtl-Meyer fan from the internal expansion region will change and thus interact differently with the cowl. In this case, it is more thrust efficient to have the recompression occur higher up on the plug surface as there is more surface area to create pressure thrust. As the incoming pressure increases, the point of compression moves down the plug.

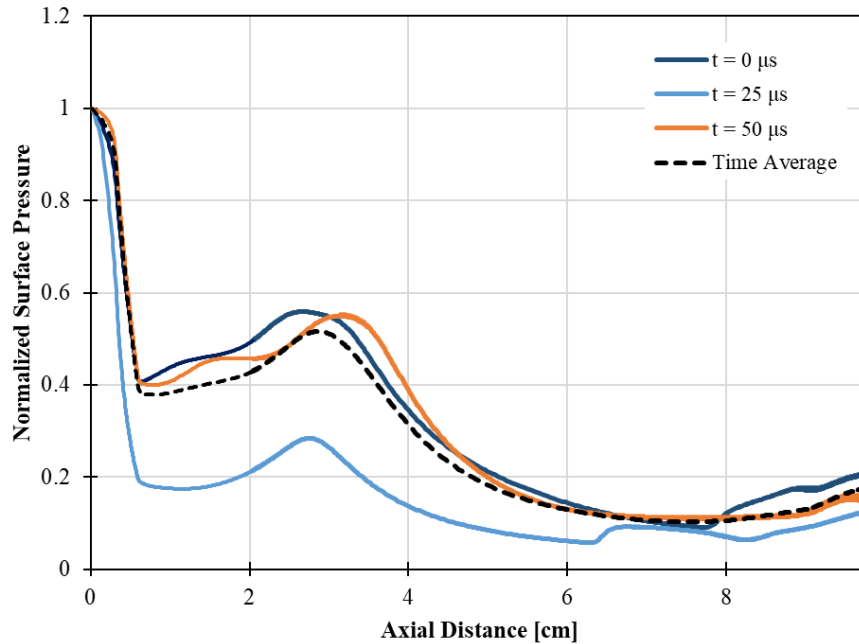


Fig. 3.12. Normalized surface pressure over axial distance at one azimuthal location for three times in detonation wave cycle. Cycle time-averaged solution also shown. Cowl exit plane at 2.5 cm.

The second feature is the location of the flow separation. From snapshot one to two, the incoming pressure decreases, causing a more overexpanded flow condition on the plug. The flow separation point moves up the plug as the adverse pressure gradient occurs also occurs higher up on the plug. When the high pressure part of the wave enters the nozzle at the end of the cycle, the flow separation point moves toward the tip of the plug. The high pressure gases are continuously re-energizing the boundary layer, causing the flow separation to be pushed toward the nozzle plug. From the averaged solution over the cycle, it is shown that this re-energization of the plume is an important mechanism to delaying flow separation. The frequency of the pressure wave re-energizes the plume continuously; the flow does not have time to react to the local pressure gradient to allow flow reversal to travel further up the surface of the plug. Thus, the presence of high pressure gases combined with the low revisit time limit the formation of the recirculation/flow separation region.

3.3 Nozzleless versus IE-Aerospike Results

3.3.1 Overall Performance

While a nozzleless geometry would never be used for a flight engine, it is useful to determine the effect of adding a nozzle to try to isolate the performance of the engine from the performance of the nozzle. To date, a method of analytically assessing the addition of a nozzle with the transient behavior of the RDE has not been discovered. Many experimental RDEs are tested without a nozzle entirely. Typically some estimate is used to predict the effect of base drag and thus isolate the performance of the engine alone. These estimates typically rely on models based on steady-state behavior and then cannot use a nozzle efficiency to predict flight performance characteristics.

The following results in Table 3.3 aim to isolate the effect of the IE-aerospike design on the nozzle performance for the 3D detonation wave cases. The addition of the IE-aerospike geometry increased the specific impulse, coefficient of thrust, and nozzle efficiency of the RDE about 16% over the nozzleless case. This is a significant increase when compared to the analytical results from Ref. [7], which found increases of 3-6% in specific impulse by adding an aerospike nozzle over no nozzle.

Table 3.3.
Detonation wave pressure profile performance time-averaged results
for nozzleless and IE-aerospike geometries.

Metric	Nozzleless	IE-Aerospike	Difference
I_{sp} [s]	180.3	215.4	+16.3%
c_F	0.96	1.15	+15.9%
η_N	0.75	0.89	+15.9%

While it may be tempting to use this as a general factor of improvement, it is unknown how to isolate the results between the losses due to the enhanced base drag

and the gain due to using an aerodynamic expansion surface. Additionally, these results are specific for sea-level ambient conditions.

3.3.2 Comparing Axisymmetric 2D Time-Averaged and Full 3D Solutions

As mentioned Chapter 2, in addition to conducting full 3D detonation wave case simulations, several 2D axisymmetric cases at pressure ratios encompassing the detonation wave cycle were also conducted for the nozzleless and IE-aerospike geometries. These cases were conducted to determine how accurate a series of less computationally intensive cases could be used to estimate the full 3D solution. The solutions from the 2D cases were time-averaged using the same detonation wave profile. Table 3.4 shows the performance parameters of the 3D and 2D time averaged cases for both the nozzleless and IE-aerospike geometries, respectively.

Table 3.4.
Results of 3D detonation wave case versus time-averaged 2D axisymmetric cases for nozzleless and IE-aerospike geometries.

	Geometry	3D Det. Wave	2D Time Average	Absolute Difference
I_{sp} [s]	Nozzleless	180.3	200.2	-11.0%
	IE-Aerospike	215.4	212.1	1.5%
c_F	Nozzleless	0.96	1.12	-15.9%
	IE-Aerospike	1.15	1.25	-8.8%
η_N	Nozzleless	0.75	0.85	-13.1%
	IE-Aerospike	0.89	0.86	4.1%

The specific impulse for the IE-aerospike does not seem to vary greatly with the type of analysis method. In contrast, the result for the nozzleless case changes significantly, by 11%. This is attributed to the enhanced base drag caused by the oscillating waveform, as there is a 12% discrepancy in the base drag between the two

cases. Thus, it may be appropriate to use less computationally intensive methods to estimate the performance of an RDE with a nozzle, but not for a blunt body design. For both geometries, the coefficient of thrust and nozzle efficiency trends do not correspond tightly with the specific impulse trend; this may be due to difficulty in calculating a time-averaged chamber pressure.

3.4 Flared Aerospike Results

3.4.1 Flow Features

In addition to evaluating the IE-aerospike geometry, the flared aerospike design was also evaluated computationally. As the time-averaged 2D and 3D results agreed well for the IE-aerospike design, it was decided to only look at the 2D axisymmetric results for the flared aerospike geometry to reduce computational time.

In order to evaluate the flow features of the flared aerospike, the 2D axisymmetric flow fields were compared to those for the IE-aerospike. Figure 3.13 shows the Mach contour plots for the IE-aerospike (left) and flared aerospike (right) at three nozzle pressure ratios. The top and bottom plots show the NPRs that encompass the detonation wave pressure profile; i.e., the NPRs that represent the lowest ($\text{NPR} = 3$) and highest ($\text{NPR} = 30$) points in the cycle. The middle plot shows the NPR at the CTAP ($\text{NPR} = 8.5$).

At the lowest pressure ratio considered, $\text{NPR} = 3$, the flared aerospike overexpands the flow more, causing the flow to separate almost immediately. This is unsurprising, as the flared aerospike has a larger area ratio and should expand the flow more than the IE-aerospike. Flow separation also occurs higher up the ramp of the flared aerospike in the CTAP case. At the highest NPR considered, the flared aerospike expands the flow more optimally, whereas the flow is significantly underexpanded for the IE-aerospike.

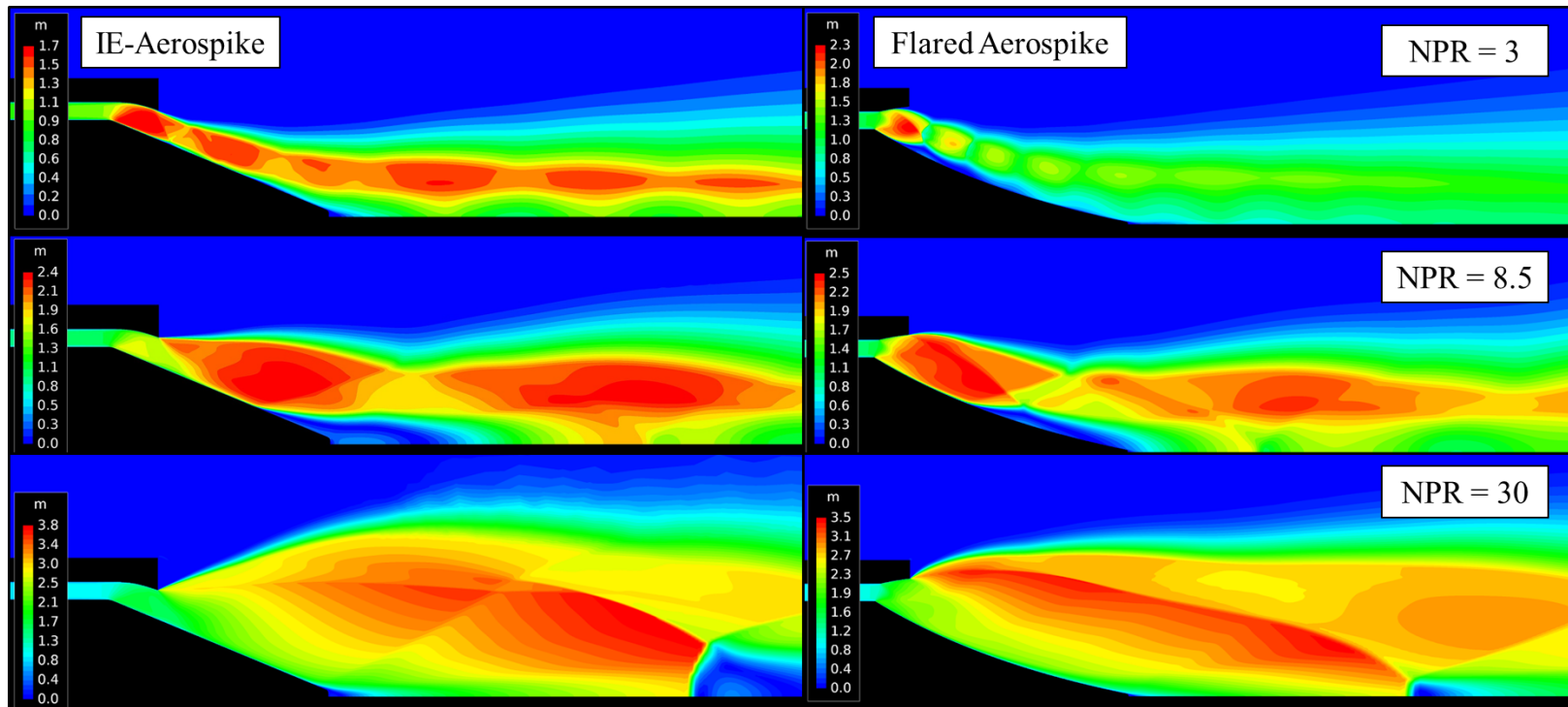


Fig. 3.13. Mach contour plots for IE-aerospike (left) and flared aerospike (right) at NPR = 3, 8.5, and 30.

An important difference in the flow fields is that while the internal expansion design of the IE-aerospike causes recompression at the top of the ramp, the flared aerospike continuously expands the flow from the throat down the ramp. The recompression in the IE-aerospike case causes higher pressures at the top of the ramp, which improves the pressure thrust contribution at this point. The recompression region is undesirable, however, as deceleration of supersonic flow can lead to inefficiencies, including shock losses. Also, it causes the flow to be underexpanded even beyond what the design area ratio would prescribe. The flared aerospike was designed to avoid the inherent flaws of the IE-aerospike design.

3.4.2 Performance Results

To understand the benefit of using the flared aerospike design, we will once again compare to the IE-aerospike design. Table 3.5 shows the performance results for the IE- and flared aerospike designs using the 2D axisymmetric time-averaged solutions. In all three metrics, the flared aerospike slightly outperformed the IE-aerospike for the pressure wave cycle considered. Again, the flared aerospike has a larger overall area ratio of 3.8 compared to the IE-aerospikes area ratio of 3.0; this suggests the detonation wave profile performs better at this higher area ratio.

Table 3.5.

Performance results of 2D axisymmetric time-averaged detonation wave pressure profile for IE- and flared aerospike geometries.

Metric	IE-Aerospike	Flared	Difference
I_{sp} [s]	212.1	213.5	+0.6%
c_f	1.25	1.25	+0.6%
η_N	0.86	0.86	+1.0%

The overall performance of the different aerospike designs over the averaged detonation wave cycle can be pieced into their performance at different NPRs in the

cycle. Figure 3.14 shows the nozzle efficiency as a function of the NPR for both the IE-aerospike and flared aerospikes. For reference, the time-averaged nozzle efficiency for each design is shown (dashed). Again, the NPRs shown discretize the detonation wave pressure profile. At the low pressure portions of the cycle, the IE-aerospike outperforms the flared; as observed from the Mach contours, this is due to the significant overexpansion for the flared aerospike. At higher NPRs, however, the flared aerospike outperforms the IE-aerospike. The higher performance at higher NPRs is the deciding factor in improving the overall performance, as more of the mass flow is associated at these higher pressure ratios.

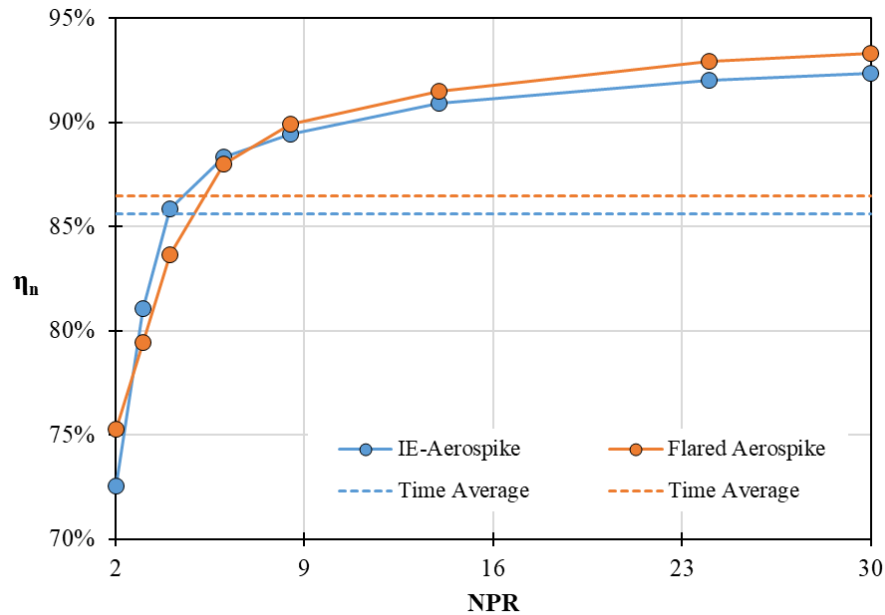


Fig. 3.14. Nozzle efficiency as function of NPR for IE- and flared aerospike. Time-averaged result also shown (dashed).

The trends in nozzle efficiency can be best understood by analyzing the component thrust contributions. The ramp and cowl surfaces contribute the majority of the pressure thrust on the surfaces and are dependent on the specific geometry. The thrust contributions for these surfaces are plotted in Fig. 3.14. At mid- to high- NPRs, both the cowl and ramp for the flared aerospike generate positive thrust. Although

the cowl in the IE-aerospike causes recompression which improves the coefficient of thrust on the ramp, the backward-facing design means that it can only create drag on the cowl surface. Another important factor is that the IE-aerospike geometry uses a conical ramp, whereas the flared aerospike in these cases had an aerodynamically designed ramp.

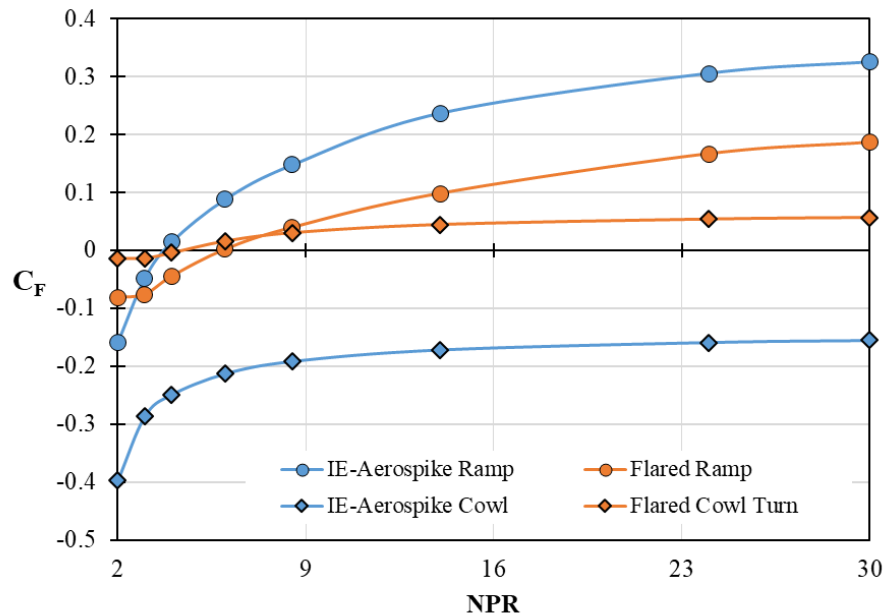


Fig. 3.15. Coefficient of thrust contribution from ramp (circles) and cowl (diamonds) for IE- and flared aerospike geometries.

3.5 Wave Number

It is unknown at present how the wave number is related to the performance of a rocket RDE. For high pressure rocket applications, it is difficult to control the number of waves beyond keeping the operating parameters the same. In terms of the combustion efficiency, for the methane/oxygen tests performed by Stechmann, lower wave number cases typically corresponded to higher performance. [10] This may not mean that lower wave numbers mean higher performance per se, but rather for the

propellants and configuration studied, a lower wave number was the optimal operating condition. The physical reason for the wave numbers effect on the performance is unknown. Additionally, it is unknown how the nozzle performance will change with wave number. The following study aims to detangle the effect of wave number on the nozzle performance from the combustion performance.

In the following study, the wave number for a full 3D detonation wave case was varied for the IE-aerospike geometry. The wave numbers studied were 1, 2, and 4 waves. The waveforms, shown in Fig. 3.16, were kept the same in each case; the peak, minimum, and equation for the pressure curve was kept the same. This is a major assumption and may not be consistent with ideal combustion performance. As the wave number increases, the fill height decreases and sidewall area relief effects become more important; thus, one would anticipate that peak detonation pressure would decrease with increased number of waves. However, the integrated pressure impulse was kept the same between cases in an attempt to isolate the effect of the wave number. The frequency of the waveform was determined using the frequencies found from Stechmann's V1.3 test campaign for various wave numbers [10]; the frequencies for the 1, 2, and 4 wave case were set to 8830, 13300, and 23300 Hz, respectively.

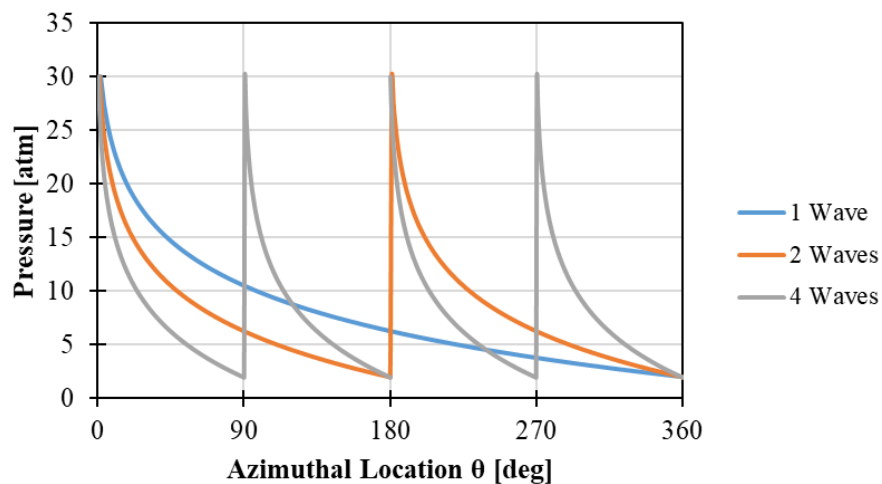


Fig. 3.16. Detonation pressure waveforms as function of azimuthal location in channel for 1, 2, and 4 wave cases.

3.5.1 Overall Performance

Table 3.6 shows the coefficient of thrust, nozzle efficiency, and specific impulse for each wave number. Although the coefficient of thrust and nozzle efficiency increase with wave number, the specific impulse peaks with the two wave case. Again, the pressure impulse is the same between all of the cases based on how the waveforms were generated. However, as the wave number increased, the mass flow rate required by the simulation slightly increased while the average stagnation pressure decreased slightly; this effect is detailed in Table 3.6. The peak raw thrust was seen in the 2 wave case. The following discussion regarding the surface pressures aims to understand this effect.

Table 3.6.

Flow conditions and performance for different wave numbers with same pressure impulse waveforms.

# Waves	Mass Flow [kg/s]	Stagnation Pressure [atm]	Force [N]	c_F	η_N	I_{sp} [s]
1	1.237	10.36	2571.9	1.13	0.88	212.0
2	1.239	10.36	2617.4	1.15	0.89	215.4
4	1.250	10.12	2561.0	1.15	0.89	208.8

3.5.2 Surface Pressures

The absolute surface pressure on the aerospike ramp for the 1, 2, and 4 wave cases is shown in Fig. 3.17 and is compared to the constant mass flow case. It is apparent that the pressure of the incoming flow changes with the number of waves in the chamber, peaking with the 2 wave case. The obvious drawback to this analysis is the fact that the waveform is essentially the same between the wave number cases; as stated above, in reality the peak pressure would likely decrease with the number

of waves, so the change in incoming static pressure with wave number may be an artificial result of this particular study. This effect is most likely an explanation for the changing performance in coefficient of thrust, nozzle performance, and specific impulse with wave number.

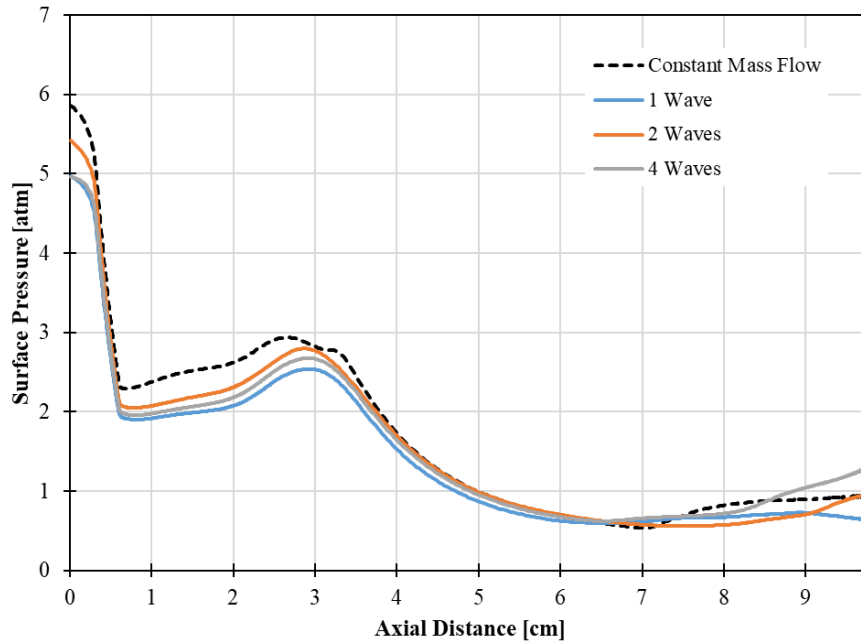


Fig. 3.17. Surface pressure on ramp surface for 1, 2, and 4 wave cases at same CTAP compared to constant mass flow case. Cowl exit plane at 2.5 cm.

Another important feature of the surface pressure plots is the location of the separation point. As stated before in the general analysis of the IE-aerospike, flow separation is delayed for the 2 wave case compared to the constant mass flow case. The onset of flow separation is difficult to pinpoint for the detonation wave cases; even as the flow clearly is not expanding anymore, the pressure does not rise rapidly back to the ambient pressure, as it does for the constant mass flow case. In the 1 wave case, the flow appears to separate close to the same point as the constant mass flow rate case. The flow separation point moves downstream for the 2 wave case, and then back upstream for the 4 wave case. The recovery pressure in the separated region

increases with wave number. The changing behavior in the location of the separation point with wave number is most likely due to the changing incoming pressure with wave number.

3.5.3 Refreshing Parameter

In assessing the effect of the number of waves on the nozzle performance, it would be helpful to have a non-dimensional parameter to determine an optimum number of waves for a specific nozzle design. One may consider the path of a particle as it traverses down the nozzle. While the primary flow direction of the particle is longitudinally down the nozzle, depending on the number of detonation waves, a particle may be re-energized or refreshed by high pressure flow more than once before it leaves the nozzle exit plane. The purpose of this analysis is to determine if there is a non-dimensional refreshing parameter that can be used to tune the number of waves for the nozzle design.

There are two time scales that can be used to describe the speed of the flow over the nozzle for an RDE. The first is the longitudinal time scale, or how long it takes a particle to propagate down the length of the nozzle. The time it takes for a particle to go from the nozzle entrance to the exit plane can be defined by the average axial velocity of the flow down the nozzle and the geometry of the nozzle (for a conical ramp):

$$t_{axial} = \frac{1}{v_{axial}} * L * \cos(\beta) \quad (3.1)$$

The second time scale is the wave time scale, or the speed of the detonation wave around the annulus. The time it takes for the pressure wave to be transmitted around the circumference of annulus can be defined by the velocity of the detonation wave, the number of waves, and the geometry of the annulus. For simplicity, we will only consider the speed as seen at the nozzle surface, so the geometry is instead defined by the nozzle geometry:

$$t_{wave} = \frac{1}{v_{wave}} * \frac{1}{n} * 2\pi * L * \sin(\beta) \quad (3.2)$$

These two time scales can be combined to produce a dimensionless ratio of the time it takes for a pressure wave to impact a particle on the nozzle to the time it takes for that particle to exhaust off of the nozzle, called the nozzle refreshing parameter:

$$\tau = \frac{t_{wave}}{t_{axial}} = 2\pi * \frac{\overline{v_{axial}}}{v_{wave}} * \frac{1}{n} * \tan(\beta) \quad (3.3)$$

The refreshing parameter is a function of the ratio of the wave speed to axial speed, the number of waves, and a simple geometric characteristic of the nozzle design (for a conical geometry). The wave speed is typically also a function of the number of waves, while the average axial speed is a function of the average Mach number and the speed of sound.

A related parameter is the helical angle mapped out by the pressure wave as it traverses down the nozzle. As a particle is flowing down the nozzle, the pressure wave will impact the particle at this angle. It does not describe the motion of the particle itself, only the pressure wave:

$$\alpha_{helix} = \tan^{-1}\left(\frac{\overline{v_{axial}}}{v_{wave}}\right) \quad (3.4)$$

Table 3.7 shows the refreshing parameter and helical angle for the different wave number cases considered, where the wave speeds were based on experimental data. In all cases, the nozzle geometry is the same ($\theta = 22.57$ degrees). The computed time-averaged Mach number is 1.6 for the geometry considered and the speed of sound is 1351.0 m/s for an average axial velocity of 3150.5 m/s.

The refreshing parameter approaches unity near the two to four wave cases. The results of the V1.3 experiments showed that the performance appeared to peak for a wave number of 2. [10] This trend suggests that the optimal refreshing of the nozzle occurs when the particles on the nozzle only encounter the pressure wave once. This could theoretically be the optimal refreshing rate, as the engine does not waste energy

Table 3.7.

Time scales, refreshing parameter, and helical angle for 1, 2, and 4 wave cases.

# Waves	t_{wave} [ms]	t_{axial} [ms]	τ	α_{helix} [deg]
1	93.1	43.8	2.1	39.2
2	60.1	43.8	1.4	46.4
4	37.5	43.8	0.9	52.7

on continually re-energizing the same particles before they exhaust out of the engine. The number of waves can then be tuned in conjunction with the nozzle design to approach a refreshing parameter of unity.

The helical angle increases with the wave number. As the particles are moving downstream, they are impacted by the pressure wave at an increasingly more normal angle. Thus, as the wave number increases, the rotating effect of the wave is not felt as greatly by the particles; rather, as the waves flow increasing more normal to the axis, the effect is more like an axially pulsing pressure wave rather than a rotating pressure wave.

3.6 Internal Expansion Ratio Results

3.6.1 Explanation of IEAR/IEPR

In conventional nozzle design practice, the main design parameter is the throat-to-exit area ratio, known as the nozzle area ratio. The nozzle area ratio is used to optimize the nozzle for the operating pressure ratio. When considering an aerospike geometry, obviously utilizing the nozzle area ratio is still valid. However, the inclusion of the cowl, which typically is used to expand the flow to some intermediate pressure ratio before the flow is exposed to the ambient conditions, means that there exists another important design parameter: the internal-expansion area ratio (IEAR). The IEAR is defined as the cowl exit area – essentially the flow cross sectional area at the

cowl exit plane – to throat area ratio. Similarly, the internal-expansion pressure ratio (IEPR) is the pressure ratio expected from the throat to the exit plane of the cowl.

Annular aerospike geometries have a unique property in that there is no set geometric solution for a given throat area and nozzle area ratio. Figure 3.18 shows an example of this property for a simplified annular RDE geometry. The annular channel location can be moved inward and outward; as long as the channel gap is adjusted to keep the throat area the same, and the diameter of the cowl exit is kept the same, the nozzle area ratio will also be the same. Obviously just keeping these parameters the same in this context does not necessitate that the performance will be the same; instead, the IEAR now plays an important part in determining the expansion properties.

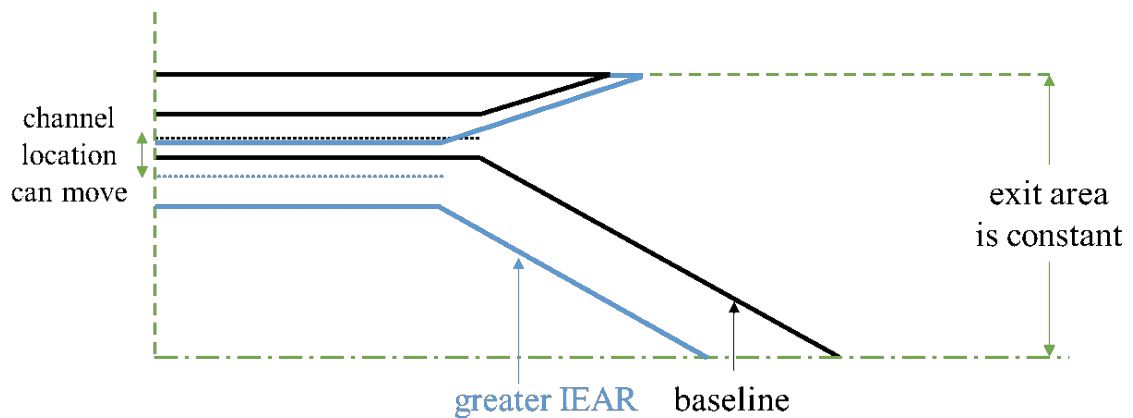


Fig. 3.18. Change of IEAR for annular aerospike geometry with constant throat area and nozzle area ratio.

In the context of annular RDEs, it is important to know the optimal placement of the annular combustion chamber with respect to the nozzle. The channel diameter and gap are critical parameters in the combustion/detonation performance, but it is also necessary to know how to integrate these features with a nozzle designed to optimally expand for the pressure ratios the engine will experience. The following study aims to

isolate the performance due to the IEAR, which can help to inform how to integrate the nozzle with the overall engine design.

The flared aerospike geometry was used for this study. Instead of using the aerodynamically designed surfaces, the cowl and ramp geometries were simplified to conical surfaces. Curved surfaces near the channel exit were employed for smooth expansion and to prevent shock formation. Four different IEAR cases were evaluated; the baseline case is the same engine geometry as previously described. In the following cases, the channel was moved by a certain percentage either inward or outward. Small changes in the channel location dramatically change the IEAR. Table 3.8 details the changes in channel dimension and the corresponding IEAR and IEPR.

Table 3.8.
Dimensions, internal-expansion area ratio, and internal-expansion pressure ratios considered for internal-expansion parametric study.

Case	Channel Radial Location [cm]	IEAR	IEPR
+3%	4.67	1.49	4.78
Baseline	4.55	1.96	7.43
-3%	4.42	2.38	9.93
-10%	4.09	3.20	15.13

3.6.2 Overall Performance

The four different IEAR geometries were run as 2D axisymmetric computations with a constant mass flow inlet. The channel length was kept the same for all geometries. For reference, the wider the channel diameter, the smaller the IEAR, as it takes less axial distance to expand to the final exit diameter. Figure 3.19 shows the Mach contour for the different IEAR cases. For the baseline and -3% cases, the plume looks to be optimally expanded – ie, the plume at the cowl does not expand or contract

significantly. As the IEAR increases, the separation zone on the ramp decreases. In the highest IEAR case, there is detachment of the plume on the cowl surface.

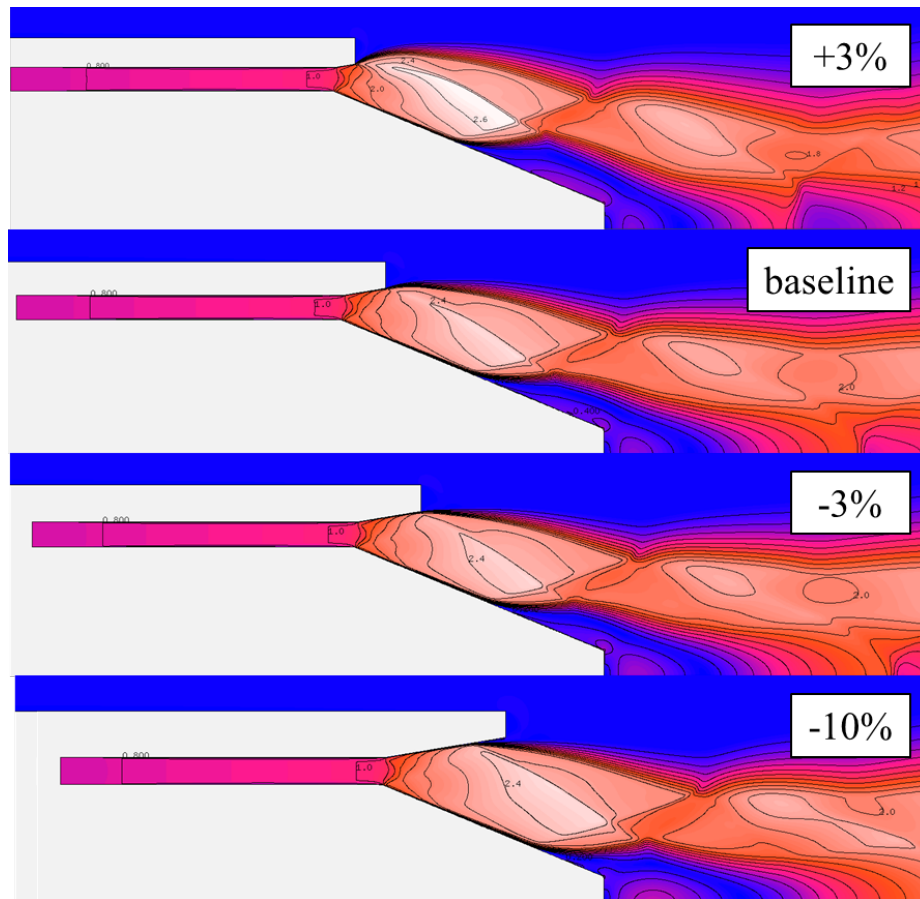


Fig. 3.19. Mach contours of exhaust plume for different internal expansion pressure ratios.

Figure 3.20 shows the specific impulse as a function of the IEPR. It is apparent that at some intermediate value of IEPR, there is a local peak in performance. The dashed line shows the operating pressure ratio. From the trend, it appears that designing the IEAR to produce an IEPR close to the operating pressure ratio will produce the highest performance. This is contrary to typical nozzle design practice, where the overall nozzle area ratio is designed to produce an NPR close to the operating pressure ratio. It is important to note that the changes in specific impulse are within 2%, so the trend shown may be within the uncertainty of the computation.

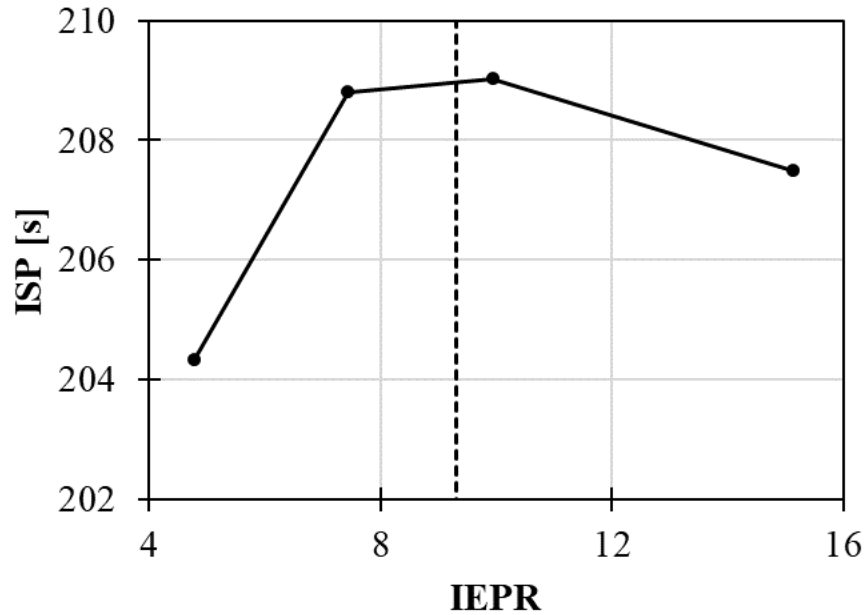


Fig. 3.20. Specific impulse with changing internal expansion pressure ratio for flared aerospike geometry; operating overall pressure ratio shown (dashed).

The component thrust contributions show how the change in geometry affects the distribution in pressure thrust. Figure 3.21 shows the component contributions from the ramp and cowl on the coefficient of thrust. For IEPR at or below 9.3 (the optimal expansion ratio), the contribution of pressure thrust appears to be evenly split between the cowl and ramp. Changes in IEPR have equal effect on the ramp and cowl. After $IEPR = 9.3$, changes in IEPR do not have equal effect on the ramp and cowl contributions. At the highest IEPR considered, the pressure thrust contribution from the ramp significantly drops, while that from the cowl significantly increases. At this high IEPR, the surface area of the ramp has significantly reduced, so there is less area to generate pressure thrust. Subsequently, the surface area of the cowl has increased, and therefore has more area to generate pressure thrust.

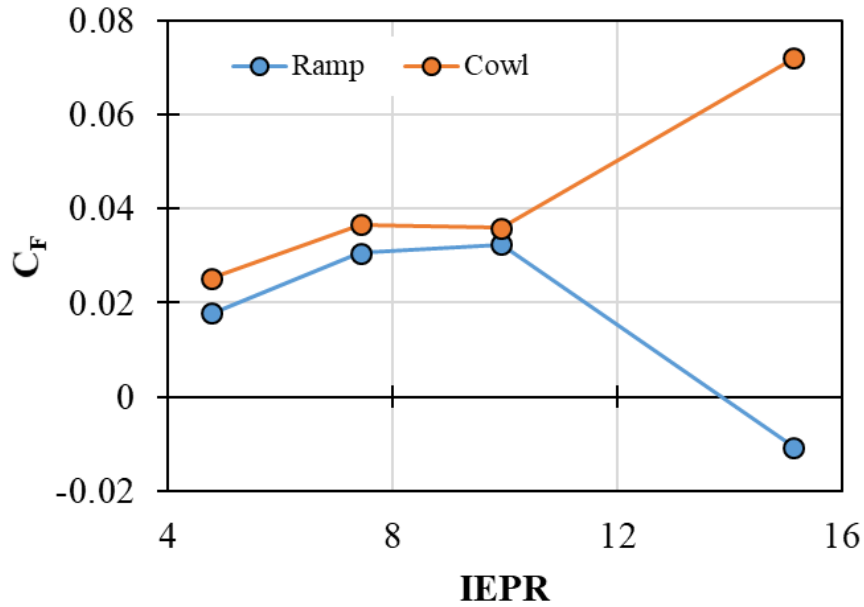


Fig. 3.21. Component coefficient of thrust for flared aerospike ramp and cowl surfaces with changing internal-expansion pressure ratio.

3.7 Channel Length

At present, it is unknown how to appropriately dimension the length of the chamber in an RDE to optimize the thrust potential. In the RDE community, it is held that there is some optimal length for the chamber based on the fill height. The fill height is the distance cold reactants reach before wave arrival. If the chamber length greatly exceeds the fill height, larger viscous losses will be incurred, whereas a chamber shorter than the fill height would lead to some propellants being combusted outside the chamber itself. Theoretically, the chamber length should be close to or larger than the fill height, [7] but this has not been extensively studied yet. The longer the chamber is made, however, the more the pressure waves will relax as the gases expand out toward the engine exit plane. Computationally, it has been shown that there is only a thermodynamic benefit by extracting work from the highly non-uniform pressure wave of the detonation. [13] Thus, as the chamber length extends, the thrust

generation should decrease. Beyond these general guidelines, no quantitative metric exists.

While the effect of the chamber length on combustion performance is obviously complex, the following analysis looks to isolate its effect on the nozzle performance alone. The length of the chamber should have two major effects on the pressure waves that exhaust onto the nozzle. The first, as mentioned before, is the relaxation or attenuation of the pressure waves. As discussed previously, the detonation wave case produces a higher specific impulse than the corresponding constant pressure case, showing that there is an efficiency improvement by using a non-uniform wave. However, it is unknown how the attenuation of the pressure wave affects the performance, i.e., perhaps the sharpness of the wave peak has an effect. The second effect is that of the viscous dissipation due to the increased wall surface area with increased chamber length. Based on the computational analysis by Matsutomi [13] and the added effect of viscous dissipation, theoretically shortening the chamber would enhance the nozzle performance.

Three different chamber lengths were evaluated to determine the effect on the nozzle performance. The first was the original chamber length used in previous computations, with a chamber length of 8.3 cm. The next two cases shortened the chamber length by using half and a quarter of the original chamber length, respectively. It is important to note that again, the entirety of the detonation wave is not modeled; rather, the exhausting condition of the detonation wave is imposed as the inflow boundary condition.

3.7.1 Overall Performance

The computational performance results for the chamber length, shown in Table 3.9, show a more complicated trend than suggested from theory. Between the original and the quarter-length case, the performance in all metrics slightly declined by shortening the chamber length; however, for the half-length case, the performance

more significantly declined. These effects are within half of a percent, so these results may be within the margin of error of the computation. To better understand these results, a more detailed look at the surface pressures is required.

Table 3.9.
Performance results for original, half-, and quarter- length chambers.

Normalized Chamber Length	c_F	η_N	I_{sp} [s]
1/4	1.16	0.90	212.5
1/2	1.15	0.90	211.8
Original	1.16	0.91	214.1

3.7.2 Surface Pressures

The surface pressure plots for the different chamber length cases provide an equally complicated picture as the performance trends suggest. Figure 3.22 shows the surface pressure for both the chamber wall and the ramp surface, where the boundary between these two surfaces is denoted by the $x = 0$ line. The internal chamber wall surface plots start at different axial locations depending on the chamber length considered. It is immediately apparent that the pressure incoming to the channel changes with the channel length considered. Again, the incoming boundary condition is a time-varying pressure inlet; unlike a mass flow inlet, a pressure inlet is more flexible, so that the computation will vary the pressure at this boundary to satisfy the solution. The incoming mass flow for all three cases is within less than a percent, so the boundary condition is still enforcing the same mass flow. This means that the flow conditions are changing radically in the subsonic portion of the chamber, where information can still be propagated backward, causing the computation to change the pressure inlet to achieve the same mass flow. To understand the mechanism driving the change

in incoming chamber pressure, the fluid dynamics in the chamber must be evaluated further.

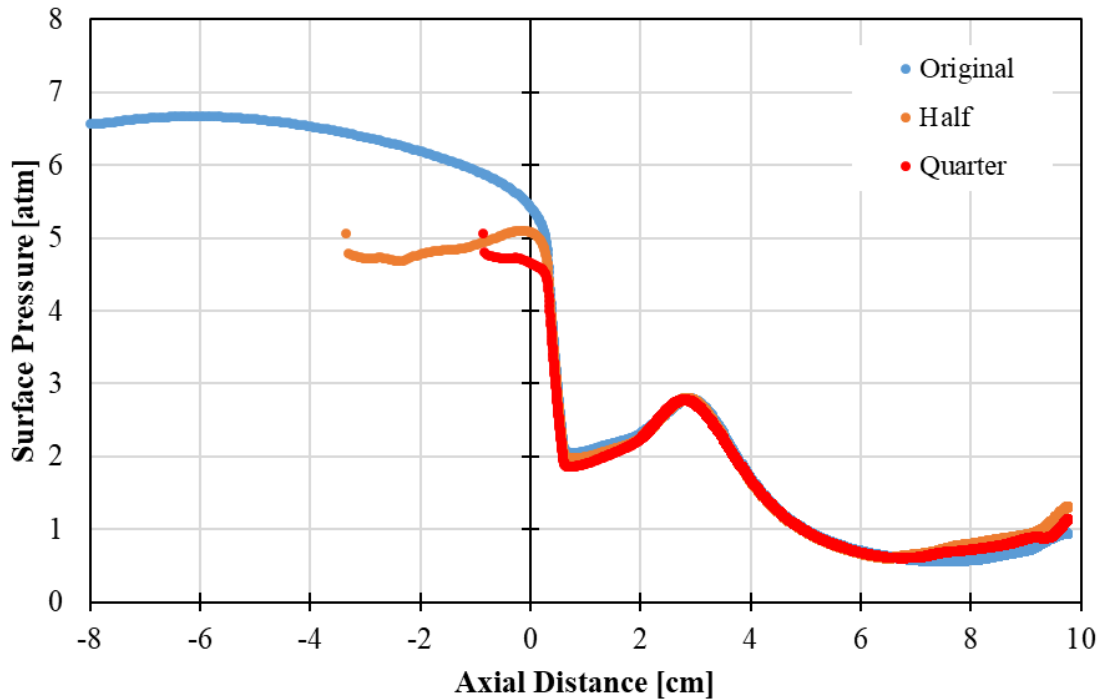


Fig. 3.22. Surface pressures on chamber wall and ramp surfaces for original, half-, and quarter-length chambers. Cowl exit plane at 2.5 cm.

The incoming pressures for the half and quarter length cases are comparable, but much lower than the original length case. Shortly after the chamber to ramp boundary at $x = 0$, however, the surface pressure plots for all three cases are very similar. After the flows are recompressed in the internal expansion region of the cowl, the pressure recovers to almost the same value in all three cases, near $x = 2.6$ cm. The only difference beyond this feature are the separation points; the half and quarter length cases appear to separate at about the same point, earlier than the original case. This is unsurprising considering the lower incoming chamber pressure.

Plots of the sonic plane inside each internal chamber, shown in Fig. 3.23, help to better understand the reduction in incoming pressures for the different chamber length cases. In the full length chamber case, the Mach 1 iso-surface extends backward, following the expansion behind the pressure wave. In the shorter chamber length cases, while it appears some expansion is occurring directly behind the wave, the flow suddenly becomes sonic after a certain axial distance downstream of the inlet boundary. This may be the boundary between the slip and no slip walls in the computation; an artificial jump in the physics. This jump appears to affect the solution more as the chamber length decreases. Thus, the different trends in surface pressure in Fig. 3.22 are partly due to the natural expansion of the pressure wave and the formulation of the simulation.

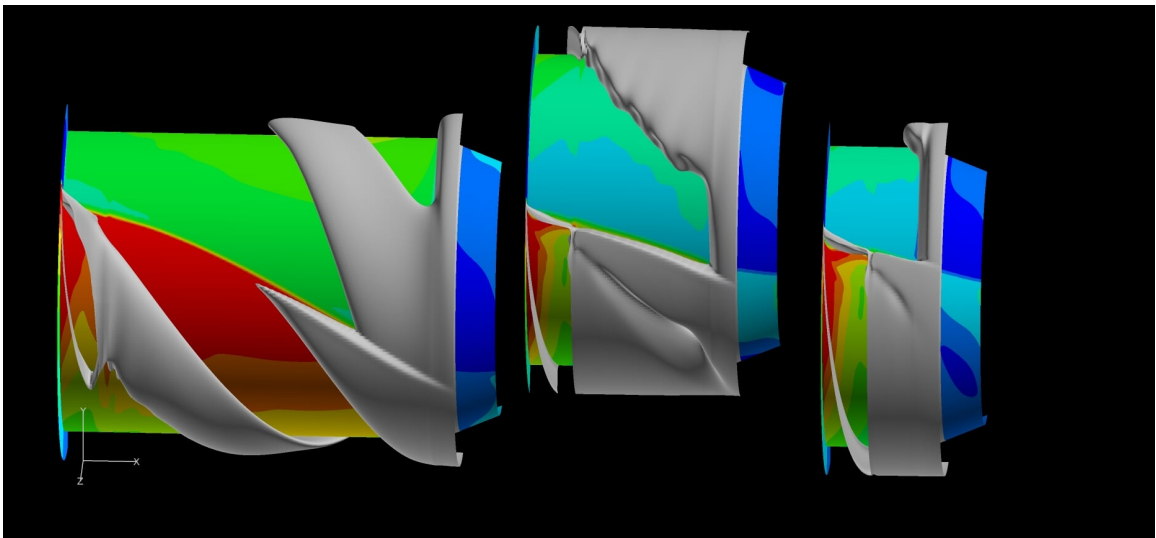


Fig. 3.23. Flow fields inside each chamber for chamber length study. From left to right, (a) original, (b) half-, and (c) quarter-length chambers. Inner chamber wall is mapped with colored pressure contours. Gray volume designates Mach 1 iso-surface. Flow is from left to right in each chamber.

4. EXPERIMENTAL RESULTS

The previous discussion encompasses the results and trends of the computational studies only. This chapter focuses on validation of the computational studies against experimental results. In Section 4.1, the computational results are compared to the RDE V1.3 test campaign that employed the IE-aerospike design to determine the accuracy of the computational parameters. In Section 4.2, new experiments from the V1.4 test campaign are analyzed. The computational results that are based on the V1.3 campaign are compared to the V1.4 experimental results.

4.1 RDE V1.3 Test Campaign

4.1.1 Background

The rotating detonation engine V1.3 test campaign, led by Dr. David Stechmann, was conducted in the spring of 2017. [10] The propellants investigated were natural gas or methane with gaseous oxygen. Both the nozzleless and IE-aerospike configurations were tested. Eighty-four tests were conducted with either configuration, 72 of which used natural gas as the fuel. Multiple parametrics were evaluated, including chamber gap size and injector configurations. Please see reference [10] for more about the specific configuration used for each test. Test #53 of this series, which utilized the IE-aerospike nozzle, was used as the basis of the computational work as described thus far as this test displayed stable rotating detonations with two waves.

4.1.2 Instrumentation

The primary test conditions measured during the test campaign were thrust, mass flow rates, and time-averaged pressures. Axial force was measured via three calibrated

load cells. Mass flow rates were metered with cavitating venturis upstream of the run valves. Pressure transducers and thermocouples on either side of the venturis were used to calculate the subsequent mass flow rates. A capillary tube averaged pressure was taken by mounting a semi-infinite capillary tube to the chamber. High frequency pressure measurements were impossible to capture as the combustion process destroyed all flush mounted probes. Please refer to Stechmann's dissertation for additional details into instrumentation. [10]

4.1.3 Comparison of Experimental Performance to Computation Results

In order to determine the validity of the computational results, the 3D time-varying result and 2D logarithmic model were compared to the test results from the V1.3 campaign. Only tests using the 0.3 chamber gap were considered to keep the throat area parameter constant; however, all injector configurations were included as there did not seem to be any particular effect on the thrust. The V1.3 test campaign with the larger chamber gap includes 33 tests with the IE-aerospike configuration and 26 with nozzleless configuration.

Figure 4.1 compares the experimental results for both the nozzleless and IE-aerospike cases to the 3D time-varying and 2D axisymmetric time-averaged computational results for the nominal 1.1 kg/s cases. The V1.3 test campaign includes 22 tests with the IE-aerospike configuration and 20 with nozzleless configuration at the nominal mass flow of 1.1 kg/s. Again, the computational results were based on the input conditions for Test #53. As mentioned before, it was impossible to directly measure the flow conditions in the combustor; thus, as the detonation wave boundary condition for the computation was derived, it was difficult to match the inflow conditions to those in the experiment. Subsequently, the mass flow rates in the computations varied from the experiment.

Both the 3D and 2D results overestimate the specific impulse generated for both the IE-aerospike and nozzleless cases at the 1.1 kg/s mass flow rate. The mass flow

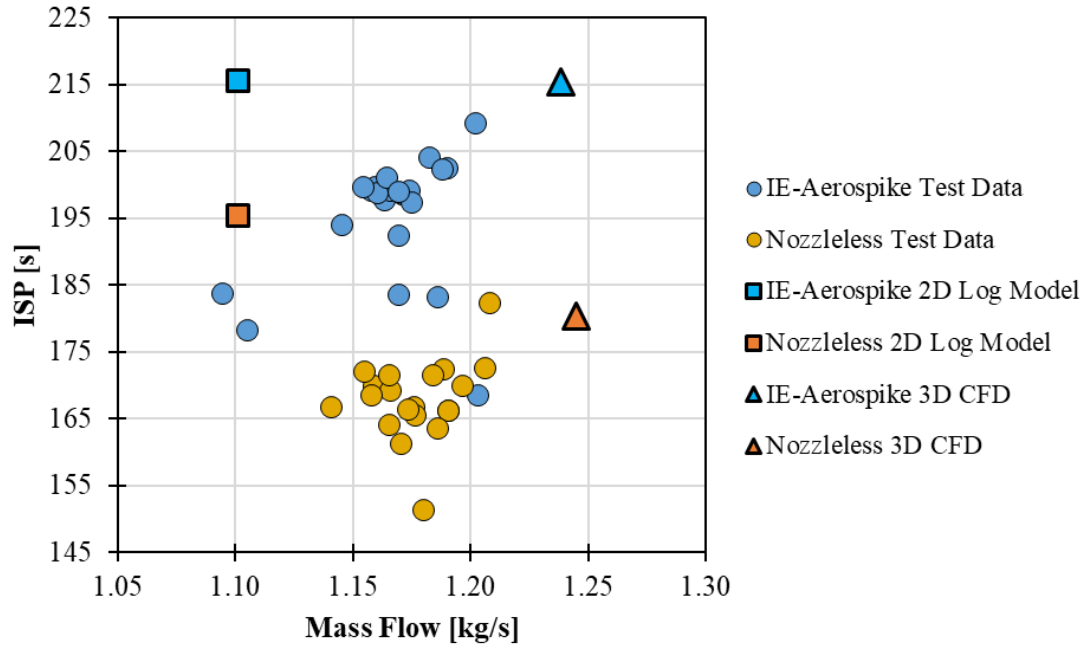


Fig. 4.1. Specific impulse of RDE V1.3 experiments, 2D axisymmetric time-averaged computational result, and 3D time-varying computational result for IE-aerospike and nozzleless configurations at nominal mass flow of 1.1 kg/s.

differs between the 3D and 2D computations because of the method used to calculate both. For the 3D computation, the pressure wave profile is imposed at the inflow and the mass flow rate is subsequently determined to match that inflow condition. For the 2D computation, the results of several computations at steady-state conditions were time-averaged, including the mass flow. Considering the mass flow rates are within 10%, this error was considered acceptable.

Table 4.1 summarizes the findings in Fig. 4.1. The 3D computational results are within 10% of the averaged experimental results, which is encouraging as it suggests the computation is able to capture a close representation of the physics in the nozzle plume. The computation does not take into account the effect of heat transfer effects, which may explain a portion of the overestimation in performance compared to the

experiment. The most significant source of error is the assumed detonation pressure profile, which again could not be exactly matched to the experimental flow conditions. It should be noted that the experiment confirms the 16.3% increase in specific impulse by adding the nozzle, which was also seen in the computation.

Table 4.1.

Average experimental specific impulse from v1.3 test campaign for nozzleless and IE-aerospike geometries compared to computational results of 3D time-varying and 2D logarithmic averaged solution.

Source	Nozzle-less		IE-Aerospike	
	I_{sp} [s]	Difference	I_{sp} [s]	Difference
Experiment	167.9		195.2	
3D Time-Varying Computation	180.3	+7.3%	215.4	+10.3%
2D Log Averaged Computation	200.2	+19.2%	212.1	+8.7%

Figure 4.2 shows the experimental results for both the nozzleless and IE-aerospike cases for all mass flow cases tested. The 3D and 2D axisymmetric time-averaged computational results for Test #53 conditions are also included for reference. As expected, the specific impulse improves with increasing mass flow, as mass flow is directly correlated to chamber pressure.

4.2 RDE V1.4 Test Campaign

4.2.1 Background

The RDE V1.4 test campaign, led by Jenna Humble and Dasheng Lim, was conducted in the spring of 2019. The propellants investigated were liquid kerosene with gaseous oxygen. This test campaign tested the nozzleless configuration, the

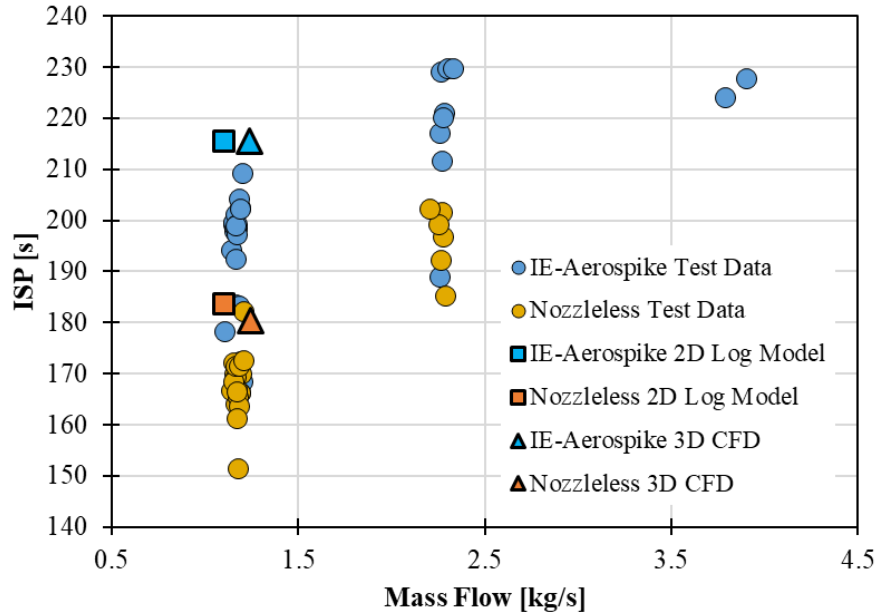
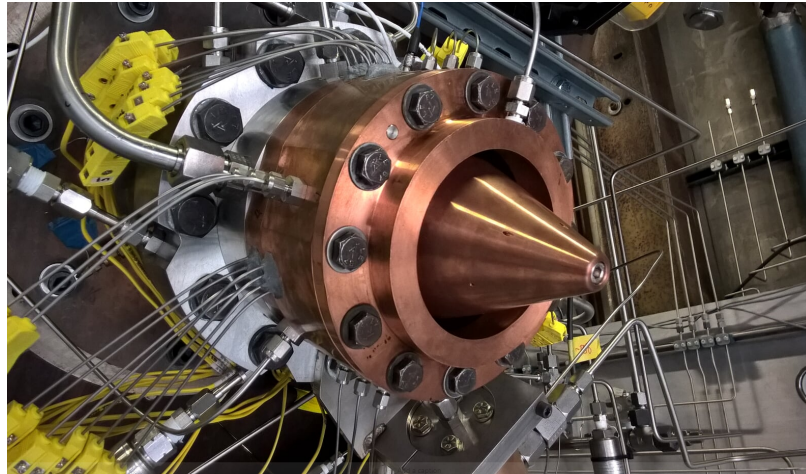


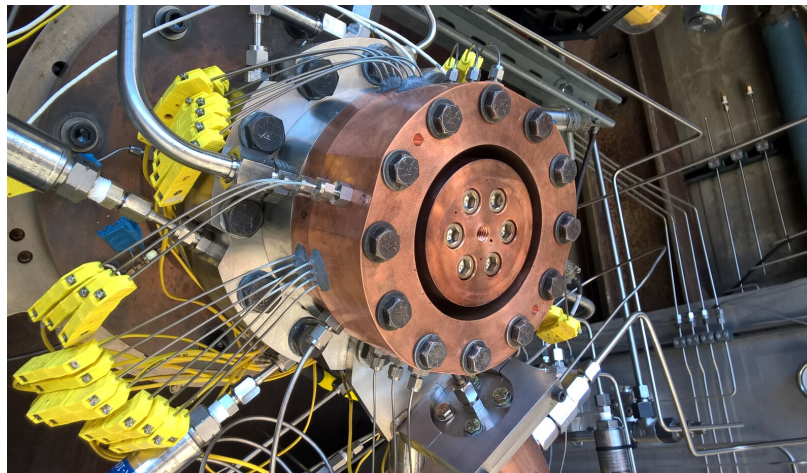
Fig. 4.2. Specific impulse of RDE V1.3 experiments, 2D axisymmetric time-averaged computational result, and 3D time-varying computational result for IE-aerospike and nozzleless configurations for all mass flow rates considered.

same IE-aerospike configuration as tested in the V1.3 campaign, and the new flared aerospike geometry introduced in Chapter 2. The V1.4 campaign hardware with the IE-aerospike nozzle and nozzleless configurations are shown in Fig. 4.3.

The following discussion compares the computational results from the V1.3 Test #53, based on natural gas/oxygen, to the experimental results derived from the V1.4 campaign, based on kerosene/oxygen. The combustion and subsequent gas properties will not be the same between the two test campaigns; however, the ratio of specific heats for the constant pressure combustion of natural gas with gaseous oxygen and kerosene with gaseous oxygen are approximately the same at $\gamma = 1.142$. If we can assume the ratio of specific heats is relatively the same, the surface pressures should be dependent on the incoming pressure field only. The speed of sound for methane is 1160 m/s compared to that for kerosene at 1350 m/s, an error of 16.3%. The speed of



(a)



(b)

Fig. 4.3. Photos of V1.4 RDE with 4.5 cm detonation channel diameter. (a) IE-aerospike nozzle and (b) nozzleless configuration.

sound change will have an effect on the detonation wave propagation down the plug, but the change is small enough to neglect in this study.

4.2.2 Instrumentation

The instrumentation used in the V1.3 test campaign was also employed in the V1.4 campaign. For this test campaign, it was decided to include pressure taps along the

surface of the nozzleless base region and the aerospike nozzles ramp region. Drawings of the hardware can be found in Appendix A. While the optimal measurement device would have included high frequency data to capture the dynamics of the pressure wave, the limited space in the engine itself prevented direct mounting of Kulites. Instead, the pressure ports extended back through the engine and were connected to low frequency pressure transducers that recorded steady-state pressure values. Although the long lengths of the pressure ports necessitate relatively large volumes, risking latency in the measurement of the steady-state pressure, the RDE mode of operation was long enough that a satisfactory steady-state period was achieved.

Due to limited available instrumentation, both GE UNIK 5000 and Druck PMP-1260 pressure transducers, with 0.04% and 0.25% of full scale accuracies respectively, were used to capture the base and surface pressures. The accuracies associated with each transducer are included in the uncertainties reported in the following results.

Figure 4.4 shows the modified hardware for the nozzleless configuration. A centerline port already existed from the V1.3 hardware. Six additional ports were added to record pressures at different radial locations on the centerbody plug. In all, seven radial locations were sampled. A front view of the computer-aided design and the actual hardware is shown in Fig. 4.5. The ports are evenly distributed along the radius of the centerbody. The six upper ports are all clocked 30 degrees away from each other; this was chosen to take advantage of the extremely limited space available in the hardware.

Figure 4.6 shows the modified hardware for the aerospike configuration. Six ports were located at different axial locations on the plug. The centerline port was unusable because this feature was used to fasten the plug to the centerbody. A front view of the computer-aided design and the actual hardware is shown in Fig. 4.7. The ports are evenly distributed axially along the length of the plug.

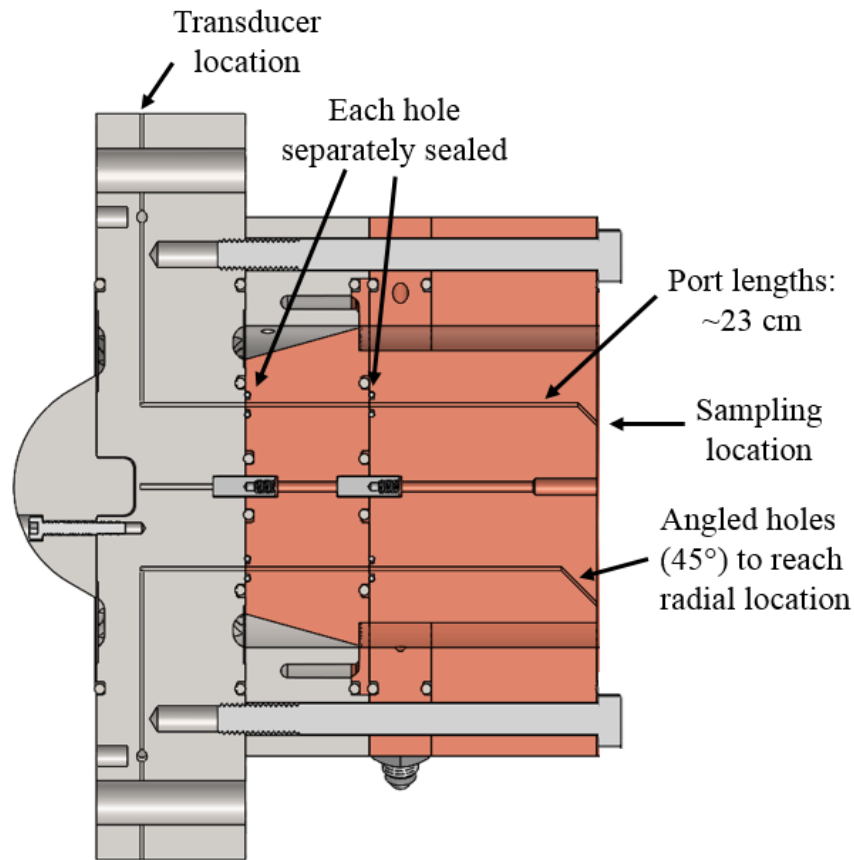


Fig. 4.4. Cut-away of nozzleless configuration with pressure ports on base surface.

4.2.3 Evaluation of Nozzleless Results

Twenty-three experiments in the V1.4 test campaign without a nozzle were evaluated. Figure 4.8 shows the base pressure plots for all seven pressure ports from Test #49. Around $t = 6$ s, the preburner igniter is activated, as seen by the noise in the data caused by the preburner spark plug. The preburner flows gaseous oxygen from approximately $t = 6.5$ s to 8 s; there is a small decrease in the base pressure values at this point. At $t = 8$ sec, the main chamber igniter is activated, as seen by the significant amount of noise caused by the spark plug. The RDE mode of operation lasts approximately 0.5 s before shutdown.

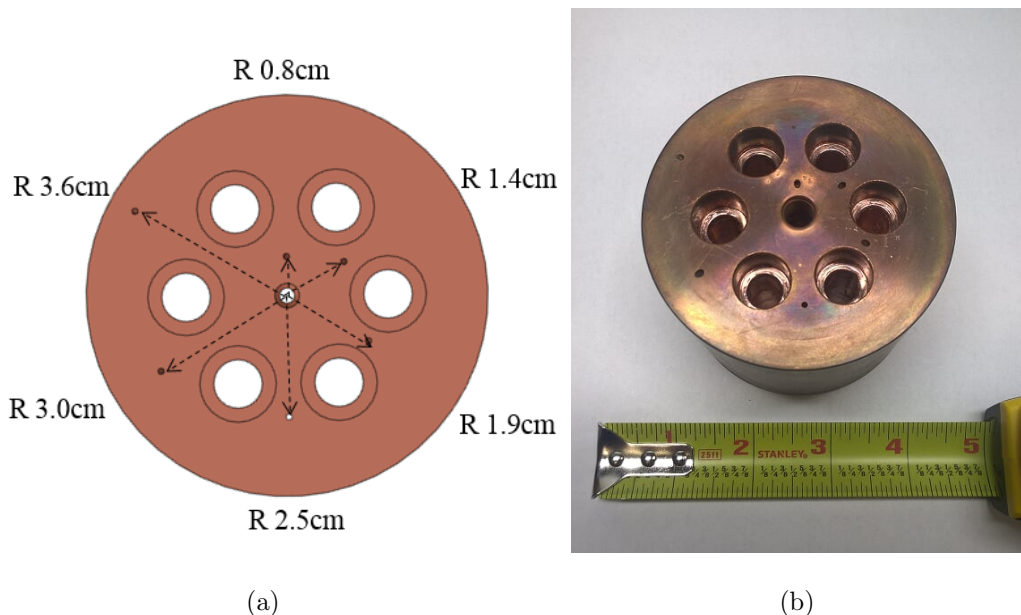


Fig. 4.5. Computer-aided design and hardware of nozzleless configuration with seven pressure ports.

Figure 4.9 shows the base pressures, windowed for the RDE mode of operation. A 1 Hz low pass filter was used. For the rest of the discussion, the base pressures are time-averaged during the RDE mode of operation. These pressures never fully equilibrate; this is expected as the flow field behind a rearward facing step takes a significant amount of time to develop. For the purposes of this study, the base pressures are stable enough for a time-averaged analysis.

The base pressures for Tests #54, 55, 65, 66, and 79 of the V1.4 campaign were compared to the computational results from V1.3 in Fig. 4.10. In Tests #54, 55, 65, 66, and 79, the mass flow rates ranged from 1.23 to 1.26 kg/s respectively, approximately 1% different from the mass flow rate of 1.24 kg/s in the detonation wave computational case. The base pressure measurements agree well with the surface pressure plot from the detonation wave case. The surface area averaged base pressures for the tests ranged from 0.58 to 0.60 psia, for an average of 0.59 psia, about 1% greater than the detonation wave case. The reduction in pressure in the test con-

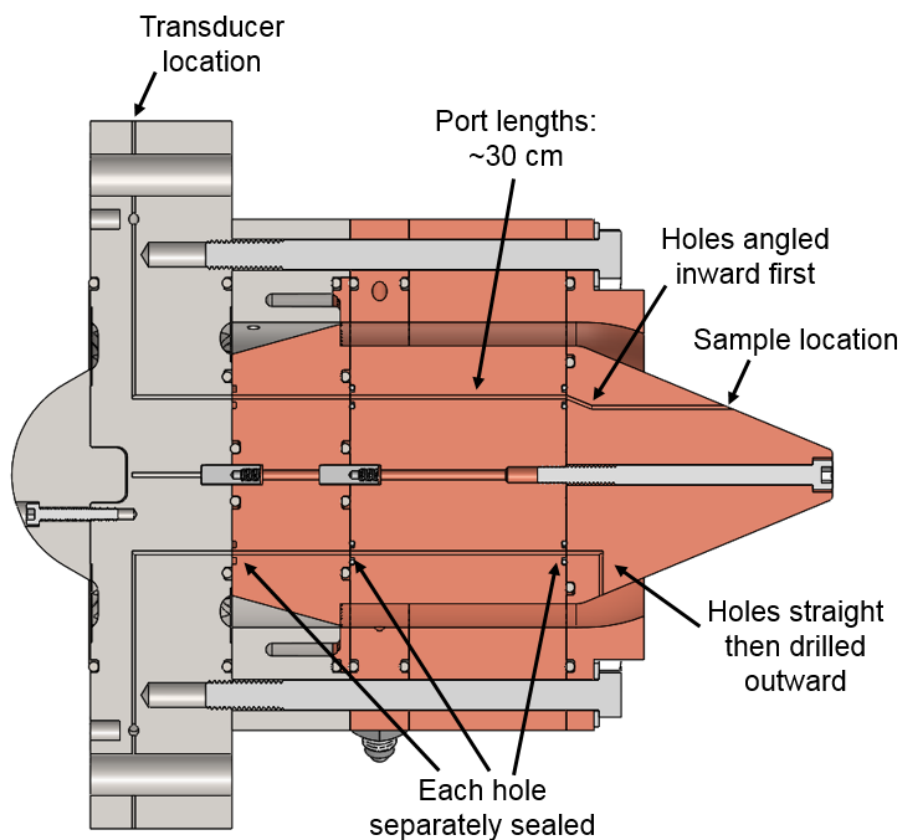


Fig. 4.6. Cut-away of aerospike nozzle configuration with pressure ports on ramp surface.

firmly that the suction on the base region of the nozzleless geometry is greater than predicted from a constant mass flow rate computation.

Predicting and evaluating the base pressure for nozzleless geometries is important to correcting the base drag component of the thrust of an RDE. As shown above, predicting the base pressure for an RDE is even more difficult than a constant pressure engine. In fact, the RDE appears to increase the inherent ejector action on the base region and increase the base drag beyond that for a steady state engine. To better understand the dynamics in the base region, the base pressure is plotted versus the mass flow rate in Fig 4.11. Equation 1.1, proposed by Stechmann, predicts that as

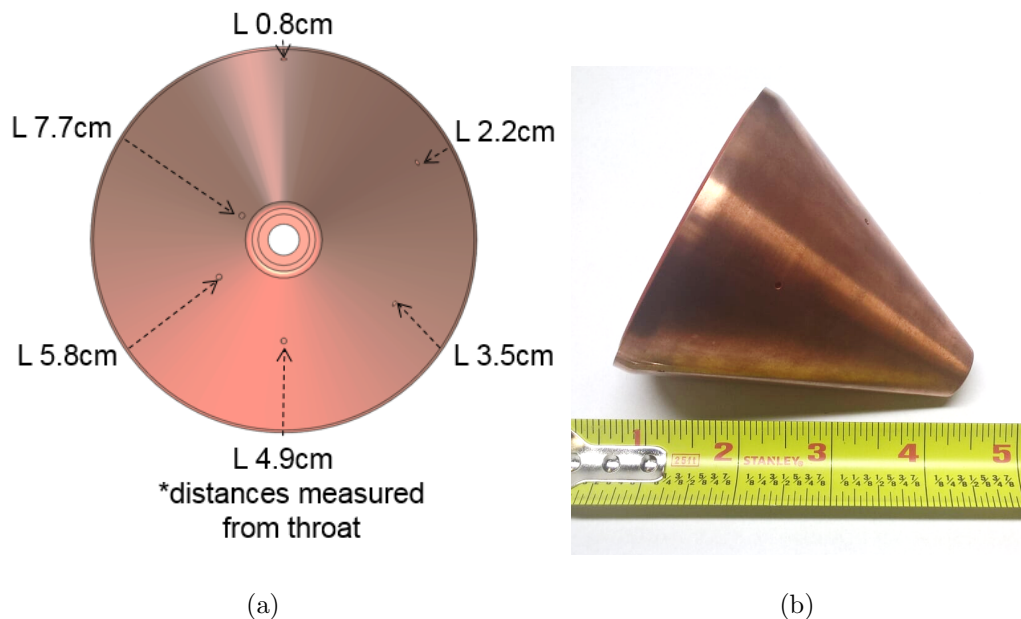


Fig. 4.7. Computer-aided design (head-on view) and hardware (profile view) of aerospike plug with six pressure ports.

the mass flow (and thus the chamber pressure) increases, the base pressure should decrease. [10] In reality, there is a non-linear relationship between the base pressure and mass flow rate. The model has decent accuracy for the cluster of tests for the mass flow rate cases around 1.3 kg/s.

The base pressure obviously cannot be simply predicted by the mass flow rate; however, there may be a relation with the chamber-to-atmospheric pressure ratio. In typical aerospike nozzle flows with a truncated cone, a base region will develop aft of the truncation; this is considered a base region. At low chamber-to-atmospheric pressures, the base region will be in open-wake mode, where the atmospheric pressure influences the base pressure. After a certain chamber-to-atmospheric pressure is reached, the base region will enter closed-wake mode, where the base pressure is independent of the atmospheric pressure. [43] This transition pressure ratio can only be derived experimentally and is dependent on the geometry and flow conditions.

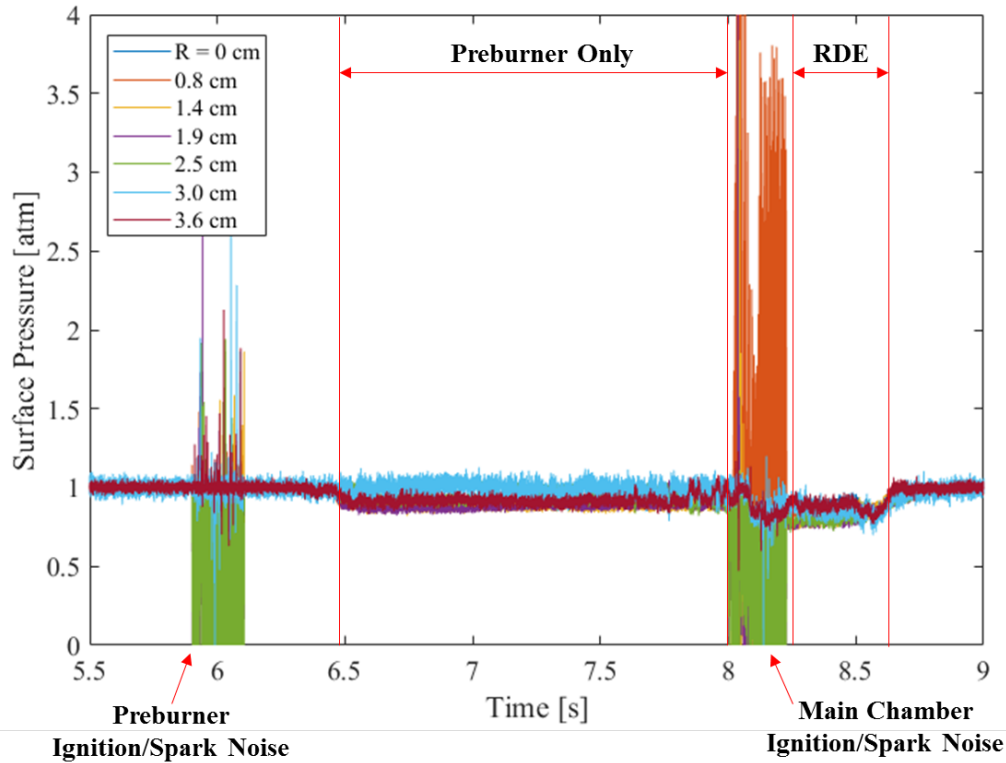


Fig. 4.8. Base pressure plots of seven base region locations on nozzle-less geometry for Test #49.

Figure 4.12 shows the normalized base pressure versus the normalized atmospheric pressure. The normalizing pressure is the incoming chamber pressure. At low pressure ratios, $P_a/P_c < 0.15$, the base pressure appears to be independent of P_a/P_c . This is considered a closed-wake mode. Above this pressure ratio, the base pressure increases with increasing P_a/P_c – also known as open wake mode. In Muellers experiments [43, 44], the data in the open wake mode followed the trend $P_b/P_c = 1$, as the base pressure was directly adjusting to the atmospheric pressure. Instead, the V1.4 experiments show an offset from theory, where the base pressure is lower than expected; this is unsurprising considering the RDE appears to have greater suction in the base region than expected with a constant pressure engine. It appears that only a normalized

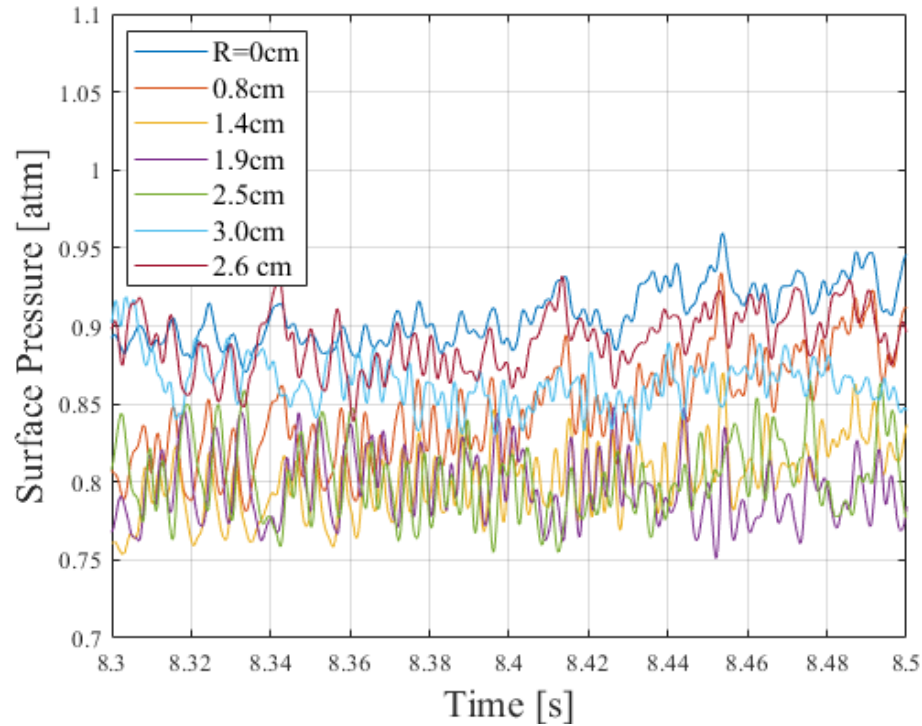


Fig. 4.9. Low-pass filtered base pressures for seven radial locations on nozzleless geometry for Test #49 during RDE window of operation.

base pressure to atmospheric pressure plot, like shown, can be used to predict the base pressure and thus the base drag.

4.2.4 Evaluation of IE-Aerospike Results

Eight experiments in the V1.4 test campaign with the IE-aerospike were evaluated. Figure 4.13 shows the surface pressure plots for all six pressure ports from Test #70. Figure 4.14 shows the ramp surface pressures, windowed for the RDE mode of operation. A 100 Hz low pass filter was used. For the rest of the discussion, the ramp pressures are time-averaged during the RDE mode of operation.

The ramp surface pressures for Tests #69, 70, and 77 of the V1.4 campaign were compared to the computational results from V1.3 in Fig. 4.15. In Tests #69, 70, and 77, the mass flow rates ranged from 1.27 to 1.32 kg/s, approximately 2 to 6% higher

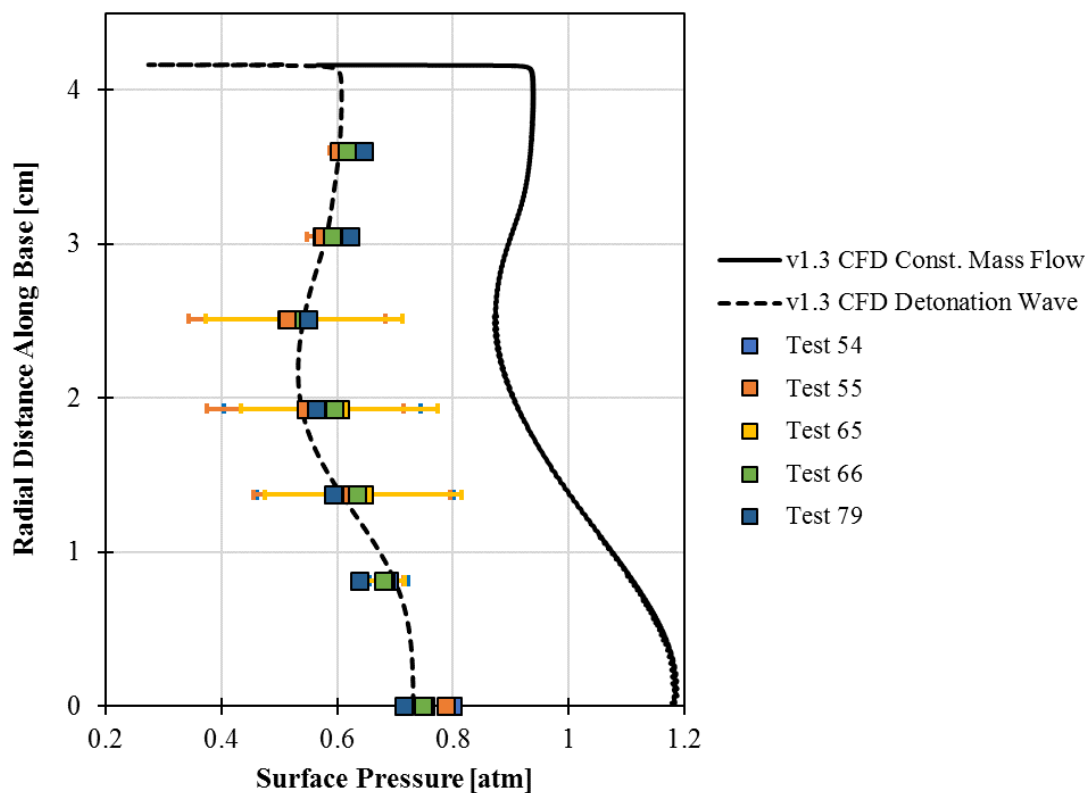


Fig. 4.10. Base pressure plots for V1.3 computations, including results from constant mass flow case and detonation wave case, compared to experimental results from V1.4 Tests #54, 55, 65, 66, and 79 for nozzleless geometry.

than the mass flow rate of 1.24 kg/s in the detonation wave computational case. The experimental results appear to confirm the presence of a region of recompression after the initial expansion after the throat. Unfortunately, there is not enough resolution in the placement of the pressure ports to resolve the peak of the recompression region. While it was predicted from the detonation wave computation that there would be a delay in the occurrence of flow separation at the end of the nozzle, the final static pressure does not appear to show this behavior. More pressure measurements in this region would be necessary to investigate the flow separation region further.

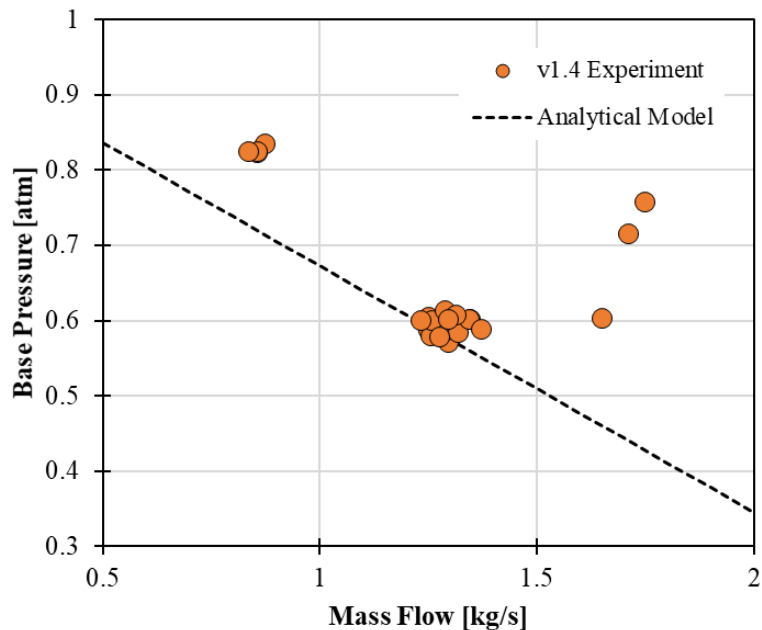


Fig. 4.11. Base pressure as function of incoming mass flow for V1.4 nozzleless experiments. Compared to Stechmanns analytical model. [10]

4.2.5 Comparison of Different Nozzle Designs

Three experiments in the V1.4 test campaign with the flared aerospike were evaluated. Each test with the flared aerospike was paired with a test with the IE-aerospike, where the operating conditions were kept the same and only the cowl was changed. The subsequent operating parameters are detailed in Table 4.2. Three different incoming mass flows/CTAPs were tested to determine the effect of the pressure ratio on the performance of the nozzle.

Figure 4.16 shows the chamber pressure normalized surface pressure plots from each of the paired tests. The normalized surface pressures are used to take into account the small differences in CTAP between the paired cases. In all cases, the flared aerospike expands the flow more rapidly than the IE-aerospike, leading to lower surface pressures. Part of this discrepancy is due to the recompression region caused by the IE-aerospike, which causes higher pressure at the beginning of the

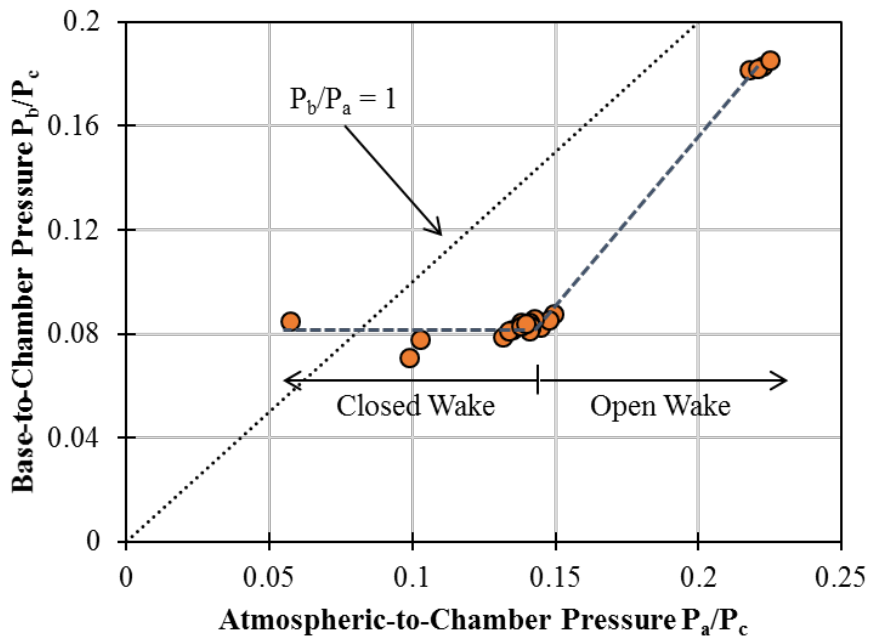


Fig. 4.12. Normalized base pressure to atmospheric pressure for V1.4 nozzleless experiments. Closed to open wake transition at approximately $P_a/P_c = 0.15$.

Table 4.2.

Conditions for low-, mid-, and high-pressure paired tests for IE- and flared aerospike geometries.

Case	IE-Aerospike			Flared Aerospike		
	Test #	CTAP [atm]	Mass Flow [kg/s]	Test #	CTAP [atm]	Mass Flow [kg/s]
Low-Pressure	77	7.8	1.32	76	7.4	1.32
Mid-Pressure	73	8.3	1.45	75	8.5	1.48
High-Pressure	87	16.5	2.77	86	15.7	2.79

plug. The higher surface pressures on the IE-aerospike plug signify that this design is producing higher pressure thrust for the pressure ratios considered. Unfortunately,

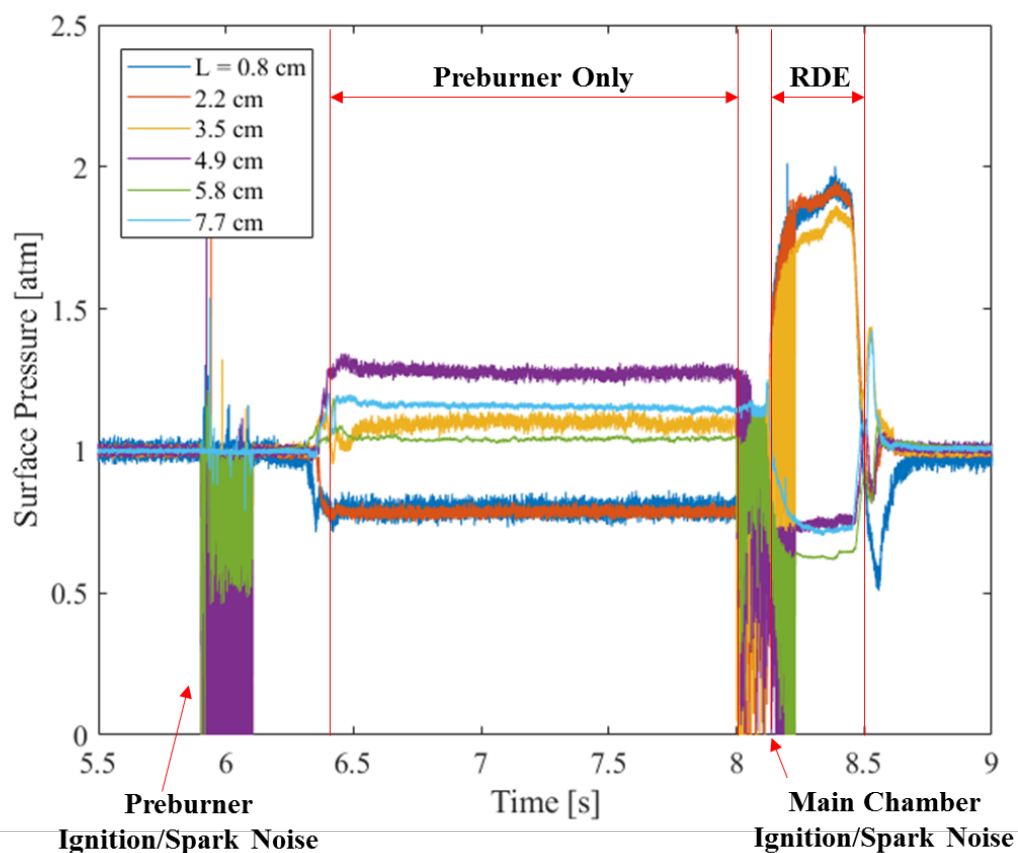


Fig. 4.13. Surface pressure plots of six ramp locations on IE-aerospike geometry for Test #70.

higher pressure ratios could not be considered as the few tests with higher mass flow rates led to destruction of the hardware. For this reason, the flared aerospike could not be tested at CTAP pressures where the higher design area ratio may have been favorable over the IE-aerospike.

For the pressure ratios tested, the flow never separated on the plug of the IE-aerospike. For the flared aerospike, however, flow separation is eventually achieved due to the greater expansion ratio. This is apparent from the sudden rise in surface pressure at station 5 for the low- and mid- pressure cases (Figs. 4.16(a) and 4.16(b)).

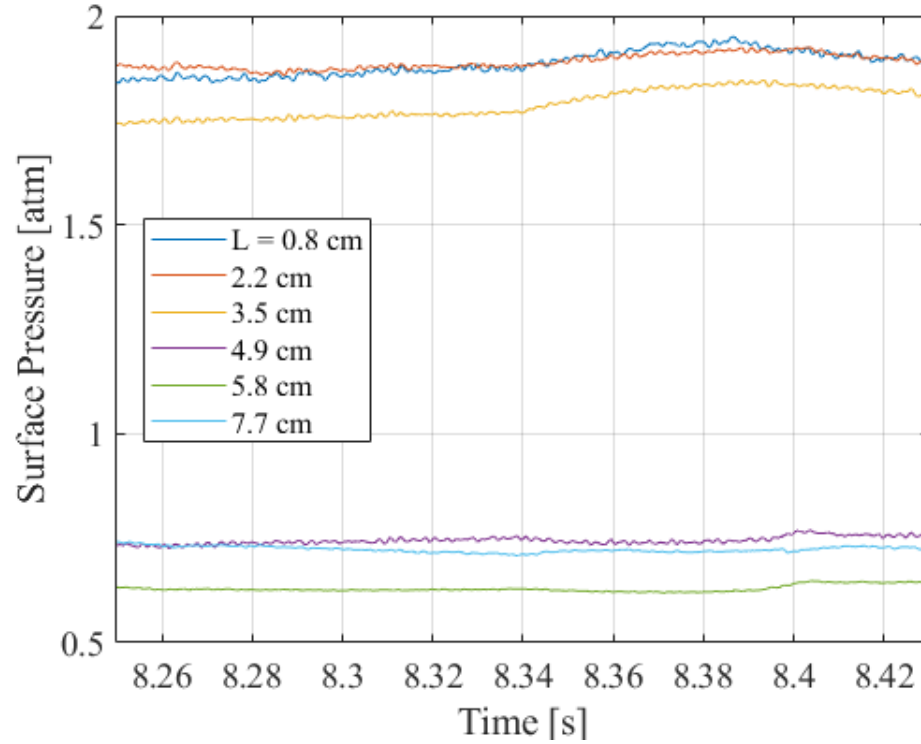


Fig. 4.14. Low-pass filtered ramp pressures for six axial locations on IE-aerospike geometry for Test #70 during RDE window of operation.

These tests are useful to show how much the flow separation is delayed by using the detonation wave pressure profile versus a constant pressure flow. In these two cases, by station 2, the surface pressure has reached $P/P_c = 0.075$, where it remains through station 4. Since the flow separates later at station 5, it can be assumed that $P/P_c = 0.075$ represents the flow separation pressure. Thus, for the detonation wave case, the flow remains attached from stations 2 to 4 even after achieving the flow separation point; this is in contrast to a constant pressure operation, where the flow would have separated almost immediately at the flow separation pressure near station 2.

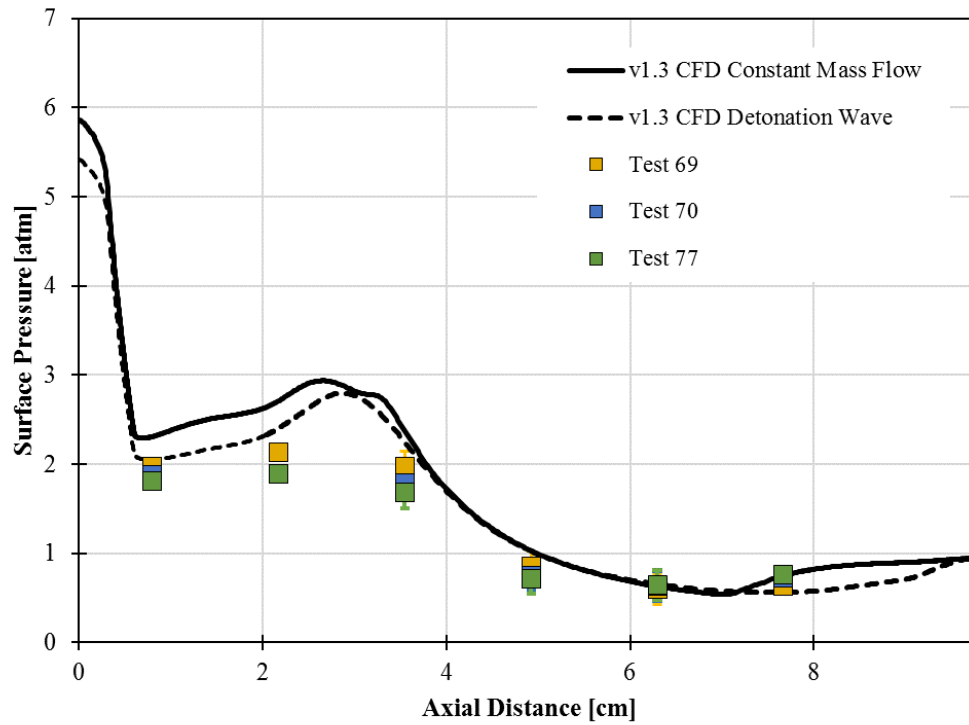
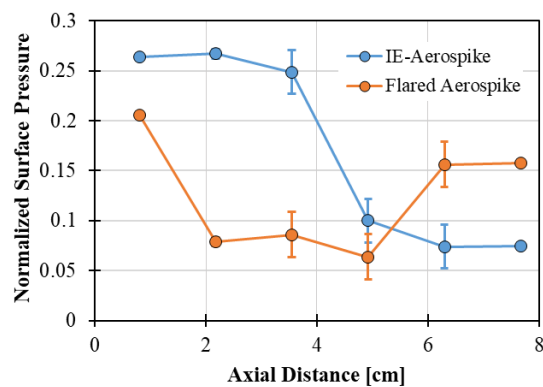
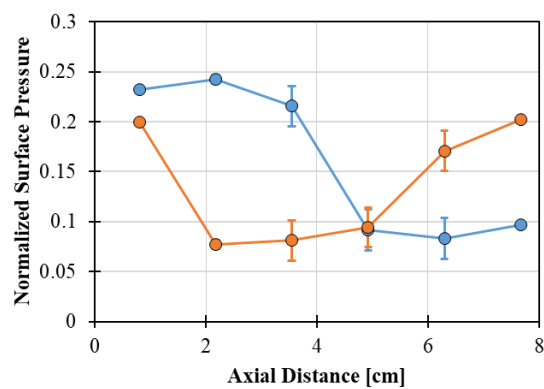


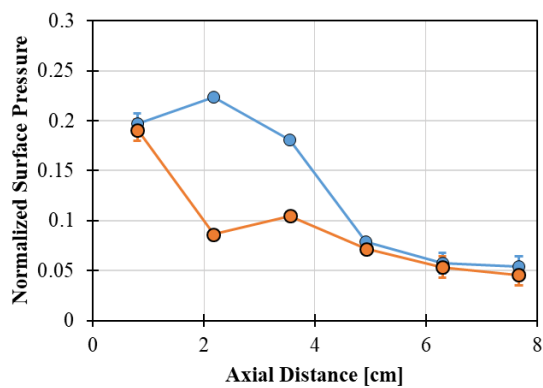
Fig. 4.15. Surface pressure plots for V1.3 computations, including results from constant mass flow case and detonation wave case, compared to experimental results from V1.4 Tests #69, 70, and 77 for IE-aerospike geometry. Cowl exit plane at 2.5 cm.



(a) Low pressure ratio.



(b) Mid pressure ratio.



(c) High pressure ratio.

Fig. 4.16. CTAP normalized surface pressures for IE- and flared aerospike at different CTAPs.

5. CONCLUSIONS

The purpose of this study was to assess the performance of a nozzle with a rocket application detonation wave pressure cycle using both computational and experimental methods. Multiple computational studies were conducted based on the experimental results of the V1.3 RDE test campaign, described in Chapter 3. The flow physics of the nozzleless and IE-aerospike geometries were analyzed and loss mechanisms were identified. A new flared aerospike geometry was designed and its performance was compared to the IE-aerospike. Several parametric studies were also conducted on the effect of the detonation wave number, nozzle internal expansion ratio, and detonation channel length.

The computational results were then compared back to multiple experiments in Chapter 4. The IE-aerospike and nozzleless geometry performances were compared to the V1.3 experiments. The V1.4 test campaign employing kerosene fuel provided surface pressures for the nozzleless, IE-, and flared aerospike geometries. These surface pressures provided confidence in the accuracy of the computations, although the different propellants used provides a caveat to direct comparison.

5.1 Main Conclusions

5.1.1 RDE Nozzleless Configuration as Enhanced Ejector

Perhaps the most significant finding from the study was the ejector action caused by the intermittent arrival of the rotating detonation wave at a given location on the nozzle surface. As seen from the computational results from Chapter 3 and verified by the experimental results in Chapter 4, the base pressure for the nozzleless geometry when operating with the detonation wave is significantly lower than for

the subsequent constant pressure case. Periodic high energy post-detonation gases continuously re-accelerate the fluid in the base region, leading to enhanced suction on the base region. In the open wake regime at low chamber pressures, the base pressure was below ambient pressure, contrary to the trend typically seen in constant pressure devices with base regions.

The lower base pressures associated with rocket RDE cycles has two major implications. The first is the effect on determining the performance of the engine. Many RDE experiments are conducted without a nozzle, where the base drag is analytically computed and subtracted from the measured thrust to determine the performance of the engine alone. If the base drag is computed using relations for a constant pressure device, the thrust of the nozzleless RDE may be significantly underpredicted. Instead, the thrust should be corrected for the inherently lower pressures associated with the RDE cycle, leading to higher potential thrust calculations.

The second implication is an unexpected application of this type of this device. The nozzleless RDE acts as an enhanced ejector, where base pressures can be drawn down below the capability of a steady ejector device. While this effect is undesirable for a rocket engine – where a nozzle would be used regardless – there are many applications for ejectors that may benefit from the enhanced suction that an RDE cycle could provide.

5.1.2 Delay of Flow Separation for RDE Aerospike

The ability of the detonation wave to re-energize boundary layers growing under adverse pressure gradients provides a mechanism to delay flow separation. In Chapter 3, 3D time-varying computations for the IE-aerospike show that the separation of the flow on the plug due to the adverse pressure gradient occurs further down the plug surface with the detonation wave versus the constant mass flow case. The delay of flow separation on the IE-aerospike was confirmed by the surface pressures captured in the V1.4 test campaign in Chapter 4. While the computational study was performed

on an aerospike geometry, the delay of flow separation for an RDE would most likely extend to any nozzle geometry considered, even a bell nozzle.

The initial reaction to this result is to assume that aerospike nozzles perform worse with a detonation wave cycle than a constant pressure inflow. The purpose of an aerospike nozzle is to naturally adapt to the ambient pressure. At low chamber-to-ambient pressure ratios, aerospikes can adapt to the ambient pressure and theoretically achieve ideal nozzle performance up to the design pressure ratio of the nozzle. Part of this altitude compensation phenomena is the flow separation on the aerospike plug, where the ambient pressure is recovered on the nozzle. For RDEs operating at ambient pressures where flow separation on the plug would occur, instead of the aerospike compensating and regaining pressure thrust on the plug, instead drag is generated. This result means that the RDE aerospike would lose some of the inherent performance benefit of the aerospike altitude compensation at low altitudes.

A way to reframe the performance benefit of using an RDE is to design the area ratio to be greater than that achievable by a constant pressure engine. Nozzles for booster engines are typically designed for a pressure altitude somewhere in between sea level and the high altitude where the second stage detaches. Typically, the area ratio is biased larger toward the higher pressure altitudes, as the majority of the engine operation is at these higher altitudes; however, the maximum area ratio for the nozzle is limited to that which will not cause flow separation at sea level. Even though flow separation is a mode of altitude compensation that can improve pressure thrust, the phenomena is typically unstable for nozzles and can cause destructive behavior. Thus, nozzle design is limited from attaining the optimal area ratio for a constant pressure booster engine. In contrast, the RDE nozzle can be designed with a much higher area ratio due to the delay of potentially destructive flow separation on the nozzle. Thus, where the RDE nozzle may lose performance at the low altitudes, it more than regains this performance in the higher altitude operation.

The performance benefit from utilizing larger nozzle area ratios makes the RDE an exciting option considering the enhanced nozzle performance alone. This analysis

does not consider the additional thrust benefit of using the higher thermodynamic efficiency of the pressure gain cycle, which may drive the thrust potential of RDEs even higher.

5.1.3 Flared versus IE-Aerospike Design

Two aerospike geometries were evaluated in this study. The first is the IE-aerospike, which was a legacy geometry from the V1.3 test campaign. The flared aerospike geometry was created to counter some of the inherent flaws in the IE-aerospike, including the backward facing cowl and the recompression region caused by the cowl. Additionally, the flared aerospike geometry allows for larger area ratio to be attained. Two-dimensional axisymmetric computational studies in Chapter 3 showed that for the detonation wave cycle considered, the flared aerospike should outperform the IE-aerospike by 1% in specific impulse.

In the V1.4 test campaign, both nozzles were tested with the same operating conditions at different chamber pressures. For all of the chamber pressures considered, the surface pressures were lower for the flared aerospike, showing the higher area ratio flared aerospike generated less pressure thrust. This suggests that the IE-aerospike, which was designed for the CTAP-to-ambient pressure ratio, is the more optimal design. Unfortunately, higher chamber pressures where the flared aerospike may have been at its design condition could not be tested.

5.1.4 Use of 2D Axisymmetric Cases to Approximate 3D Results

The results of several two-dimensional axisymmetric computational cases with constant mass flow inlet conditions were time-averaged to approximate the time-varying flow field of the full 3D detonation wave case. For the IE-aerospike computation, the 2D time-averaged specific impulse had an error of 1.5% compared to the 3D full detonation wave result. The 2D time-averaged result did not match as well for the nozzleless case, with a 10% error in specific impulse. The discrepancy is most

likely due to the oscillating plume dynamics that occur in the full 3D case and are not captured in the axisymmetric cases, as described in Chapter 3.

The main benefit to using 2D axisymmetric constant mass flow cases is lower computational cost. For example, an axisymmetric grid for this study typically had 300,000 cells, compared to 20-30 million cells for a 3D grid. Additionally, the time for the detonation wave inflow condition to reach a static periodic solution would take at least 20-30 cycles, which translated to 15000-25000 iterations, or 1-2 ms of clock time. In contrast, the 2D constant mass flow solutions needed a few thousand iterations to reach a steady state. While multiple of the 2D axisymmetric constant mass flow cases are needed – in this study, eight were used – this computational requirement pales in comparison to the cost of the 3D detonation wave case mesh size and iteration count. For future nozzle studies, it may make practical sense to start with the 2D time-averaged approach to test different conditions before moving to the computationally intensive 3D cases. The 2D time-averaged result may give relatively accurate nozzle performance results, but should not be used to analyze flow structures, etc. It is not recommended to use the 2D axisymmetric time-average approach for geometries with large recirculation regions.

5.1.5 Comparison of Computational and Experimental Results

Two major comparisons were made between the computational and experimental results in Chapter 4. The first comparison is that of the computed performance to the V1.3 experimental results. Both the 2D axisymmetric time-averaged and 3D results for the IE-aerospike and nozzleless geometries overestimate the specific impulse compared to the test results. The main suspected cause of the discrepancy is the imposed detonation waveform in the computation, which may not match the actual waveform. Based on the good agreement in the pressure traces in the latter half of the chapter, for the same CTAP, the specific pressure profile does not appear to have a large effect on the pressure thrust generated on the surfaces. Instead, the pressure

waveform most likely has the strongest effect on the thrust generated on the engine exit plane, causing the discrepancy.

The second comparison is the surface pressures for the computations based on the V1.3 campaign to the results from the V1.4 campaign. For both the nozzleless and IE-aerospike, the surface pressures for cases with similar mass flow rates are close to the accuracy of the instrumentation. This is a surprising result, considering the gas properties, number of waves, and detonation wave profile are either suspected or known to be different. This result suggests that the average stagnation-to-ambient pressure ratio is more important to the surface pressures than the above mentioned flow field properties for the aerospike geometries. In the future, it would be beneficial to add more pressure ports and use higher accuracy pressure transducers to improve the resolution and accuracy of the experimental surface pressure results.

5.2 Lessons Learned

5.2.1 CFD Solver Stability

As mentioned in Chapter 2, originally the Purdue-maintained GEMS CFD code was employed for this study. While GEMS is used at Purdue for rocket RDE computations, it was not suitable for the nozzle flow physics necessary for this study. The GEMS code did not have inherent stability schemes to prevent the computation from becoming unstable after many thousands of iterations. Eventually the computational studies were conducted with the NASA Loci/CHEM code after the GEMS computations consistently failed to perform even simple steady flow cases. The latest version of NASA Loci/CHEM had a greater degree of stability that would not diverge for the nozzle flow physics. This was especially important when conducting the detonation wave cases, where the flow field was inherently unstable. The stability of the computational solver is one of the most important factors that should be considered when conducting this type of study.

5.2.2 Design Hardware with Diagnostics in Mind

The V1.3 test campaign was conducted before significant work on nozzle design and analysis was considered. The small dimensions of the hardware provided sufficient space for hardware integration, such as securing fasteners and sealing elastomers; however, nozzle region diagnostics were given little consideration. The V1.4 test campaign hardware was directly taken from the V1.3 hardware with the same space constraints for diagnostics. The space for surface pressure ports was extremely limited; in fact, only the exact pressure port configuration described in Chapter 4 was feasible. In the future, the design of the engine should include space and functionality for the inclusion of pressure instrumentation on the nozzle surfaces.

5.3 Future Work

5.3.1 Analysis of Different Parameters

A few parametric studies were conducted in the course of this study, as discussed most extensively in Chapter 3; however, there are many different parameters that could potentially have a large effect on the nozzle performance. The following parametric studies are avenues for future work in the computational realm.

Detonation Pressure Ratio

The pressure ratio of the detonation wave is the defining parameter of the detonation wave pressure profile for a given average pressure. As the pressure ratio changes, one would expect the nozzle performance to change drastically. For example, higher peak pressures may enhance the re-energization of the boundary layer on the aerospike plug surface. Although only one detonation pressure ratio was evaluated in the course of this study, different propellant combinations with subsequently different pressure ratios necessitate more exploration into their effect on the nozzle performance.

Wave Number/Frequency

Although the effect of wave number was analyzed in this study, it was difficult to generate the correct waveform for a specific wave number case. As discussed previously, the pressure wave is not expected to be the same for different wave numbers due to differences in expansion in the detonation channel. This parametric study would benefit from deriving its inlet boundary condition from a fully reacting RDE computation.

Another confounding factor was the relationship between the wave number and the frequency. In this study, the frequency for each wave number case was drawn from experimental results from the V1.4 test campaign. It would be useful to analyze just the effect of wave number or frequency on the performance.

Area Ratio

The area ratio is the primary design factor for a thrust generating nozzle. There are two confounding factors when designing an RDE nozzle: the pressure ratio on which to base the design and how to balance the expansion between the internal and external portions of the nozzle. To determine the correct design pressure ratio for a detonation wave nozzle, a parametric study comparing different area ratio nozzles with the same geometric design is necessary. Two area ratio nozzles were compared in this study, but their cowl geometries varied drastically; the parametric study should keep the cowl geometry relatively similar.

The second necessary parametric study in this area is for the balance of the internal and external area ratios. This study did analyze the effect of the internal expansion ratio on performance; however, this parametric study was computed with constant pressure conditions and did not vary the external area ratio as well. This parametric study should be carried forward with a detonation wave inflow in the future.

5.3.2 Altitude Testing for High Area Ratio Nozzle Concepts

All of the Purdue RDE nozzle test campaigns were conducted at sea level ambient conditions. As mentioned above, the true potential of the RDE nozzle may be realized at high altitude, low ambient pressure conditions, making this engine ideal for a space engine. Future work with varying back pressures is necessary to characterize the performance map for aerospikes with a detonation wave cycle. In particular, low ambient pressures may be necessary to generate the higher chamber-to-ambient pressure ratios required to test the flared aerospoke geometry at its design pressure ratio.

5.3.3 Application of New Physics to Current Nozzle Performance Calculation Methods

This study identified two major differences in flow phenomena for the detonation wave cases. For the aerospoke geometry, flow separation was delayed until some point further downstream on the aerospoke plug. For the nozzleless geometry, the pressure on the base region was drawn down below pressures expected in a constant pressure case. While these results are critical to understand the change in performance, it is unknown how to predict the flow separation point on an aerospoke plug or the base pressure on the nozzleless base region without conducting 3D simulations. More work is required to make these results applicable when deriving the nozzle performance of these devices for other flow conditions. Two approaches may be used here; the first would be to perform more simulations on a range of parameters to derive trends. The second approach would be to revisit the analytical theory for nozzle performance and consider the effect of temporally and spatially evolving inflow conditions.

REFERENCES

REFERENCES

- [1] “Space Shuttle Main Engine Orientation,” Rocketdyne Propulsion and Power, Tech. Rep., June 1998, BC98-04.
- [2] B. I. Katorgin, V. K. Chvanov, F. Y. Chelkis, and V. S. Sudakov, “RD-180 Program History.” Salt Lake City, UT: 37th AIAA/ASME/SAE/ASEE Joint Propulsion Conference, July 2001, doi: 10.2514/6.2001-3552.
- [3] F. K. Lu and E. M. Braun, “Rotating Detonation Wave Propulsion: Experimental Challenges, Modeling, and Engine Concepts,” *Journal of Propulsion and Power*, vol. 30, no. 5, pp. 1125–1142, September-October 2014, doi: 10.2514/1.B34802.
- [4] E. Winterberger and J. E. Shepherd, “Model for the Performance of Airbreathing Pulse-Detonation Engines,” *Journal of Propulsion and Power*, vol. 22, no. 3, pp. 593–603, May-June 2006, doi: 10.2514/1.5792.
- [5] W. H. Heiser and D. T. Pratt, “Thermodynamic Cycle Analysis of Pulse Detonation Engines,” *Journal of Propulsion and Power*, vol. 18, no. 1, pp. 68–76, January-February 2002, doi: 10.2514/2.5899.
- [6] S. Gordon and B. J. McBride, *Computer Program for Calculating and Fitting Thermodynamic Functions*, 2014, <http://www.grc.nasa.gov/www/CEAWeb/>.
- [7] D. P. Stechmann, S. D. Heister, and A. J. Harroun, “Rotating Detonation Engine Performance Model for Rocket Applications,” *Journal of Spacecraft and Rockets*, vol. 56, no. 3, pp. 887–898, May-June 2019, doi: 10.2514/1.A34313.
- [8] D. A. Schwer and K. Kailasanath, “Numerical Investigation of Rotating Detonation Engines.” Nashville, TN: 46th AIAA/ASME/SAE/ASEE Joint Propulsion Conference, July 2010, doi: 10.2514/6.2010-6880.
- [9] F. A. Kykovskii, E. F. Vedernikov, S. V. Polozov, and Y. V. Golubev, “Initiation of Detonation in Flows of Fuel-Air Mixtures,” *Combustion, Explosion and Shock Waves*, vol. 43, no. 3, pp. 345–354, 2007, doi: 10.1007/s10573-007-0048-8.
- [10] D. P. Stechmann, “Experimental Study of High-Pressure Rotating Detonation Combustion in Rocket Environments,” Ph.D. dissertation, Purdue University, 2017.
- [11] D. E. Paxson and D. A. Schwer, “Operational Stability Limits in Rotating Detonation Engine Numerical Simulations.” San Diego, CA: AIAA SciTech Forum, January 2019, doi: 10.2514/6.2019-0748.
- [12] J. Kindracki, P. Wolanski, and Z. Gut, “Experimental research on the rotating detonation in gaseous fuels-oxygen mixtures,” *Shock Waves*, vol. 21, no. 2, pp. 75–84, 2011, doi: 10.1007/s00193-011-0298-y.

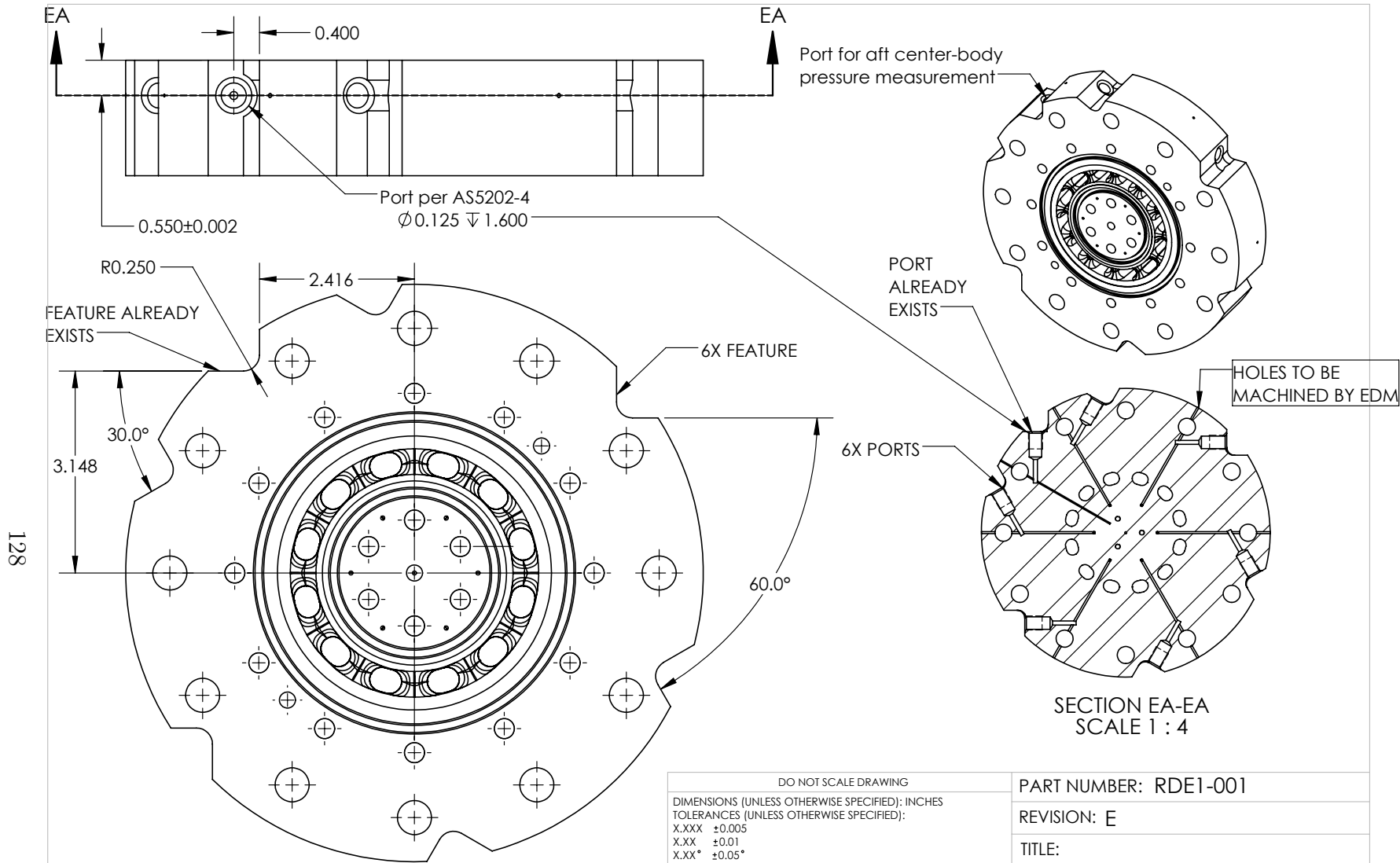
- [13] Y. Matsutomi, "Studies on Pressure-Gain Combustion Engines," Ph.D. dissertation, Purdue University, 2010.
- [14] K. Ishihara, Y. Kato, K. Matsuoka, J. Kasahara, A. Matsuo, and I. Funaki, "Performance Evaluation of a Rotating Detonation Engine with Conical-Shape Tail." Kissimee, FL: AIAA SciTech Forum, January 2015, doi: 10.2514/6.2015-0630.
- [15] M. L. Fotia, F. Schauer, T. Kaemming, and J. Hoke, "Experimental Study of the Performance of a Rotating Detonation Engine with Nozzle," *Journal of Propulsion and Power*, vol. 32, no. 3, pp. 674–681, May-June 2016, doi: 10.2514/1.B35913.
- [16] M. L. Fotia, T. A. Kaemming, J. Hoke, J. R. Codoni, and F. Schauer, "Experimental Thrust Sensitivity of a Rotating Detonation Engine to Various Aerospoke Plug-Nozzle Configuration." San Diego, CA: AIAA SciTech Forum, January 2019, doi: 10.2514/6.2019-1743.
- [17] M. C. Schnabel, "Pressure distribution and performance impacts of aerospoke nozzles on rotating detonation engines," Master's thesis, Naval Postgraduate School, 2017.
- [18] D. A. Schwer, R. Kelso, and C. M. Brophy, "Pressure Characteristics of an Aerospoke Nozzle in a Rotating Detonation Engine." Cincinnati, OH: AIAA Propulsion and Energy Forum, July 2018, doi: 10.2514/6.2018-4968.
- [19] N. Tsuboi, N. H. Jourdain, T. Watanbe, A. K. Hayashi, and T. Kojima, "Three-dimensional Numerical Simulation on Hydrogen-Oxygen Rotating Detonation Engine with Unchoked Aerospoke Nozzle." Kissimee, FL: AIAA SciTech Forum, January 2018, doi: 10.2514/6.2018-1885.
- [20] G. P. Sutton and O. Biblarz, *Rocket Propulsion Elements*, 7th ed. New York, NY: Wiley and Sons, 2001, ch. Nozzle Theory and Thermodynamics Relations, pp. 45–101.
- [21] O. July and L. Martin, "X-33 Advanced Technology Demonstrator," National Aeronautics and Space Administration, Tech. Rep., MSFC 96-1.
- [22] J. J. Korte, "Parametric Model of an Aerospoke Rocket Engine." Reno, NV: 38th AIAA Aerospace Sciences Meeting and Exhibit, January 2000, doi: 10.2514/6.2000-1044.
- [23] "Multidisciplinary Approach to Aerospoke Nozzle Design," National Aeronautics and Space Administration, Tech. Rep., February 1997, NASA TM-110326.
- [24] M. Onofri, "Plug Nozzles: Summary of Flow Features and Engine Performance." Reno, NV: 40th AIAA Aerospace Sciences Meeting and Exhibit, January 2002, doi: 10.2514/6.2002-584.
- [25] G. Hagemann, H. Immich, , and M. Terhardt, "Flow Phenomena in Advanced Rocket Nozzles - The Plug Nozzle." Reston, VA: 34th AIAA/ASME/SAE/ASEE Joint Propulsion Conference and Exhibit, 1998, doi: 10.2514/6.1998-3522.

- [26] G. Angelino, "Approximate Method for Plug Nozzle Design," *AIAA Journal*, vol. 2, no. 10, pp. 1834–1835, 1964, doi: 10.2514/3.2682.
- [27] B. L. Denton, "Design and analysis of rocket nozzle contours for launching Pico-Satellites," Master's thesis, Rochester Institute of Technology, 2008.
- [28] S. D. Smith, "Final Report - Aerospike Design and Performance Tool," Plumetech, Huntsville, AL, Tech. Rep., August 2001, PT-FR-01-01.
- [29] G. V. R. Rao, "Exhaust Nozzle Contour for Optimum Thrust," *Jet Propulsion*, vol. 28, no. 6, pp. 377–382, June 1958, doi: 10.2514/8.7324.
- [30] E. A. Luke, X. L. Tong, J. Wu, and P. Cinnella, "CHEM 2: A Finite-Rate Viscous Chemistry Solver – The User Guide," Mississippi State University, Mississippi State, MS, Tech. Rep., September 2004, MSSU-COE-ERC-04-07.
- [31] "Information about Loci/CHEM," Tetra Research Corporation, Tech. Rep., [retrieved 25 January 2019].
- [32] M. E. Harvazinski, "Modeling Self-Excited Combustion Instabilities Using a Combination of Two- and Three-Dimensional Simulations," Ph.D. dissertation, Purdue University, 2012.
- [33] J. H. Ruf and D. M. McDaniels, "Computational and Experimental Results for a Dual Throat Linear Aerospike." Pennsylvania State University: 14th Annual Propulsion Engineering Research Center Symposium, December 2002.
- [34] K. Mikoshiba, S. V. Sardeshmukh, and S. D. Heister, "Two Dimensional Simulation of RDE Combustor with a Dynamic Injection Model." San Diego, CA: AIAA SciTech Forum, January 2019, doi: 10.2514/6.2019-0477.
- [35] D. C. Wilcox, *Turbulence Modeling for CFD*, 3rd ed. La Canada, CA: DCW Industries, Inc., 2006.
- [36] ———, "Formulation of the k- Turbulence Model Revisited," *AIAA Journal*, vol. 46, no. 11, pp. 2823–2838, November 2008, doi: 10.2514/1.36541.
- [37] F. R. Menter, "Two-Equation Eddy-Viscosity Turbulence Models for Engineering Applications," *AIAA Journal*, vol. 32, no. 8, pp. 1598–1605, August 1994, doi: 10.2514/3.12149.
- [38] P. R. Spalart and S. R. Allmaras, "One-Equation Turbulence Model for Aerodynamic Flows," *Recherche Aerospaciale*, no. 1, pp. 5–21, 1994.
- [39] S. Sarkar, G. Erlebacher, M. Y. Hassaini, and H. O. Kreiss, "The Analysis and Modeling of Dilatational Terms in Compressible Turbulence," Tech. Rep., 1989, ICASE Report 89-79.
- [40] H. Schlichting, *Boundary-Layer Theory*, 7th ed. New York, NY: McGraw-Hill, 1979, ch. Turbulent flow through pipes, pp. 600–602, doi: 10.1007/978-3-662-52919-5.
- [41] E. A. Luke, X. L. Tong, J. Wu, P. Cinnella, R. Chamberlain, and K. Walters, "CHEM 4.0: A Finite-Rate Viscous Chemistry Solver - The User Guide," Tech. Rep., April 2018.

- [42] H. A. Cikanek, "Characteristics of Space Shuttle Main Engine Failures." San Diego, CA: 23rd AIAA/ASME/SAE/ASEE Joint Propulsion Conference, June 1987, doi: 10.2514/6.1987-1939.
- [43] T. J. Mueller, W. P. Sule, A. E. Fanning, T. V. Giel, and F. L. Galanga, "Analytical and Experimental Study of Axisymmetric Truncated Plug Nozzle Flow Fields," National Aeronautics and Space Administration, Tech. Rep., September 1972, NASA N-73-12282.
- [44] T. J. Mueller, W. P. Sule, and C. R. Hall, "Characteristics of Separated Flow Regions within Altitude Compensating Nozzles," National Aeronautics and Space Administration, Tech. Rep., January, NASA N-71-18990.

APPENDICES

A. RDE V1.4 HARDWARE DRAWINGS



128

SIX NEW FEATURES, OFFSET 30DEG FROM ORIGINAL FEATURE
PORTS ARE EVENLY SPACED 60DEG APART



DO NOT SCALE DRAWING	
DIMENSIONS (UNLESS OTHERWISE SPECIFIED): INCHES	
TOLERANCES (UNLESS OTHERWISE SPECIFIED):	
X.XXX	±0.005
X.XX	±0.01
X.XX°	±0.05°
X.X°	±0.5°
FINISH	63/
unless otherwise noted	
NAME	DATE
DRAWN BY: David P. Stechmann	09/19/2016
ADVISOR: Stephen D. Heister	09/19/2016

PART NUMBER: RDE1-001	
REVISION: E	
TITLE: Preburner Adaptor	
MATERIAL: 17-4PH Stainless (H900)	SIZE A
SCALE: 1:2	WT: 29.6 lbm SHEET 4 OF 7

5

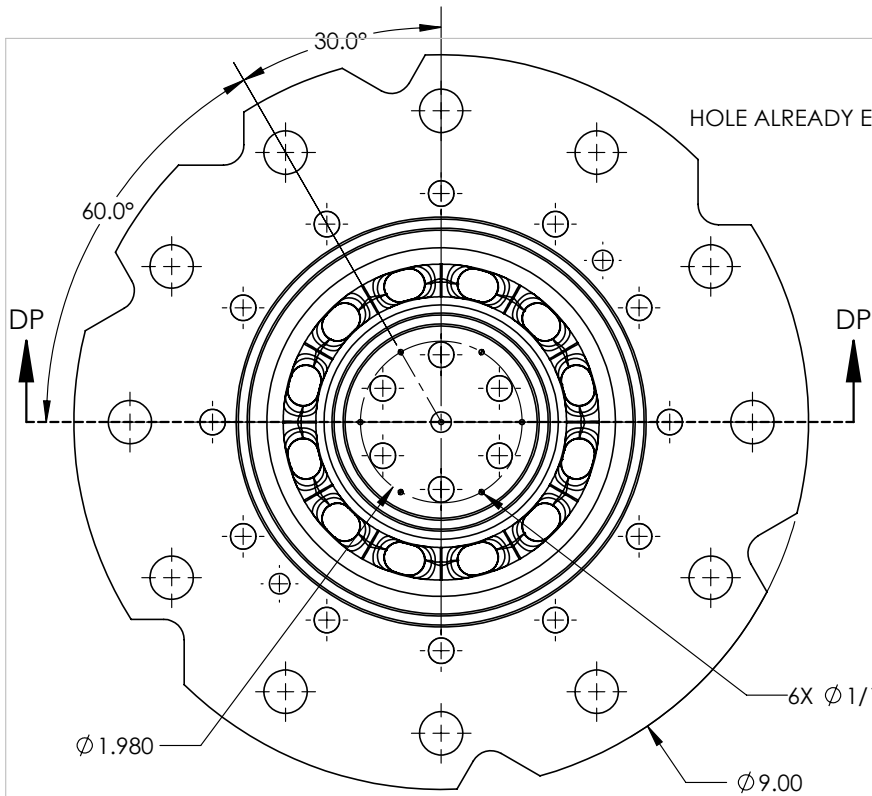
4

3

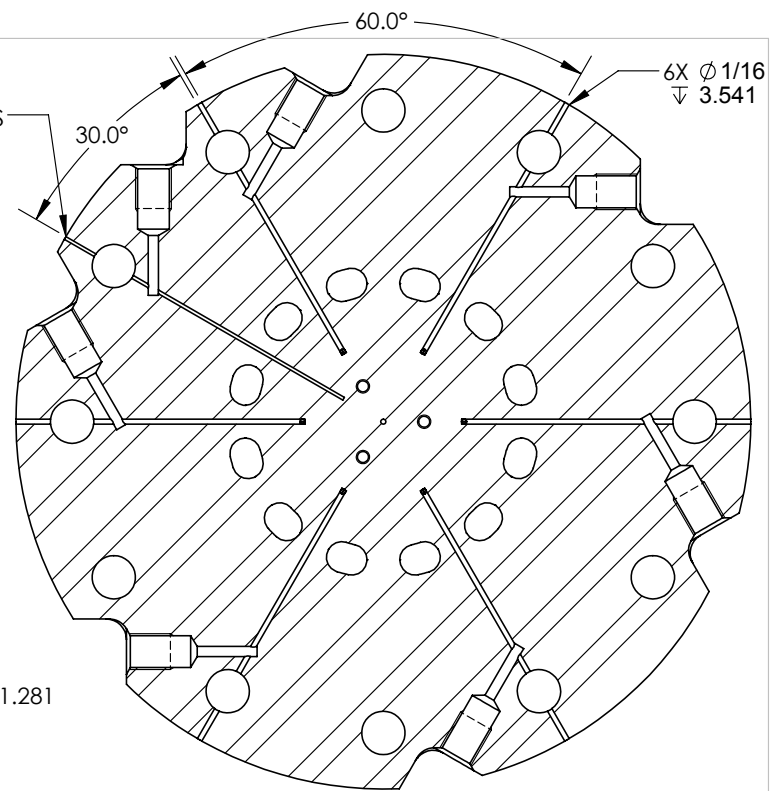
2

1

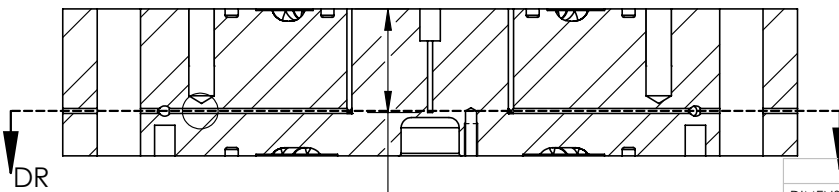
129



SECTION DP-DP



SECTION DR-DR



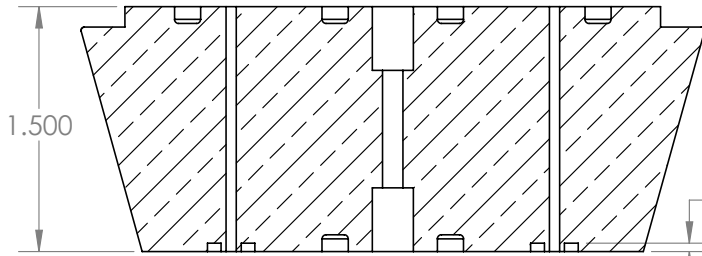
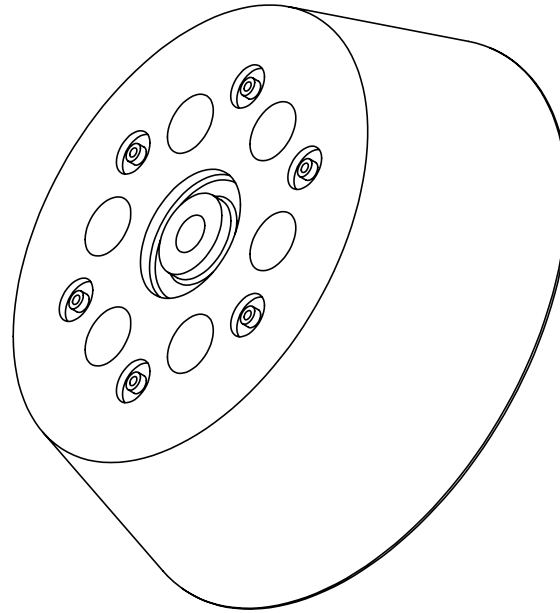
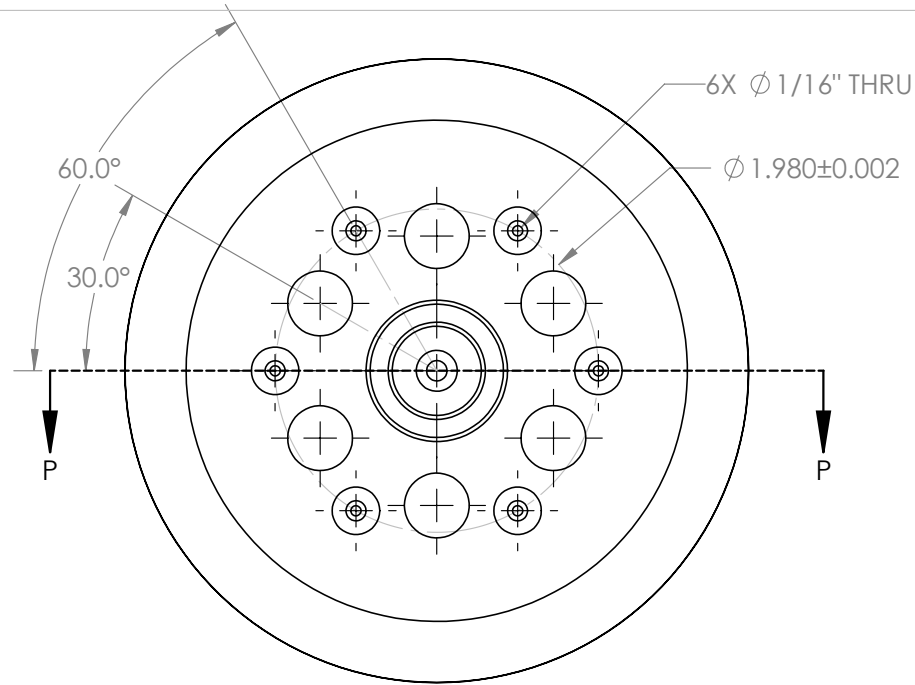
SIX 1/16" RADIAL HOLES
SIX 1/16" AXIAL HOLES

DO NOT SCALE DRAWING		PART NUMBER: RDE1-001	
DIMENSIONS (UNLESS OTHERWISE SPECIFIED): INCHES TOLERANCES (UNLESS OTHERWISE SPECIFIED): X.XXX ±0.005 X.XX ±0.01 X.XX° ±0.05° X.X° ±0.5°		REVISION: F	
FINISH 63/ unless otherwise noted		TITLE: Preburner Adaptor	
DRAWN BY: David P. Stechmann 09/19/2016		MATERIAL: 17-4PH Stainless (H900)	
ADVISOR: Stephen D. Heister 09/19/2016		SCALE: 1:2 WT:29.6 lbm SIZE A	
SHEET 5 OF 7			



5 4 3 2 1

130



SIX 1/16" THRU HOLES
 SIX O-RING GLANDS
 EACH GLAND ENCIRCLES ONE HOLE

SECTION P-P
 SCALE 1 : 1

ϕ 0.123^{+0.001}/_{-0.000}
 ϕ 0.291^{+0.000}/_{-0.003}

DO NOT SCALE DRAWING	
DIMENSIONS (UNLESS OTHERWISE SPECIFIED): INCHES	
TOLERANCES (UNLESS OTHERWISE SPECIFIED):	
X.XXX	\pm 0.005
X.XX	\pm 0.01
X.XX°	\pm 0.05°
X.X°	\pm 0.5°
FINISH	63/
unless otherwise noted	
NAME	DATE
DRAWN BY: David P. Stechmann	09/19/2016
ADVISOR: Stephen D. Heister	09/19/2016

PART NUMBER: RDE1-005B
REVISION: D
TITLE: Fuel Injector Centerbody Type B
MATERIAL: C101 or C110 Copper
SIZE A
SCALE: 1:1.5 WT: 4.1 lbm SHEET 1 OF 1



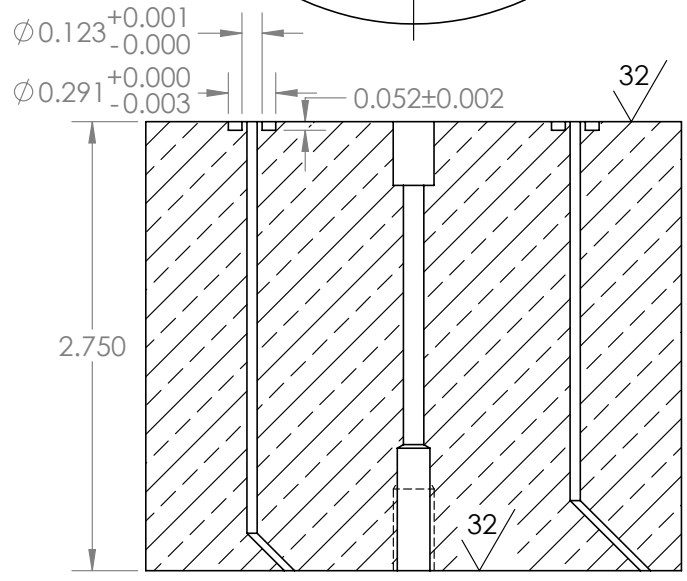
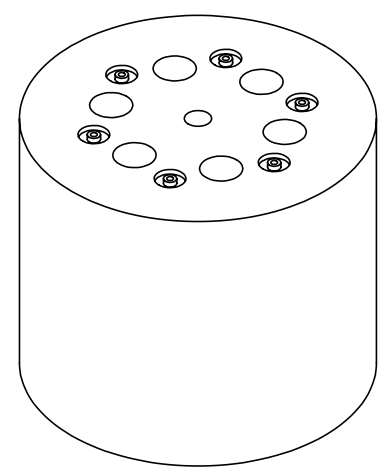
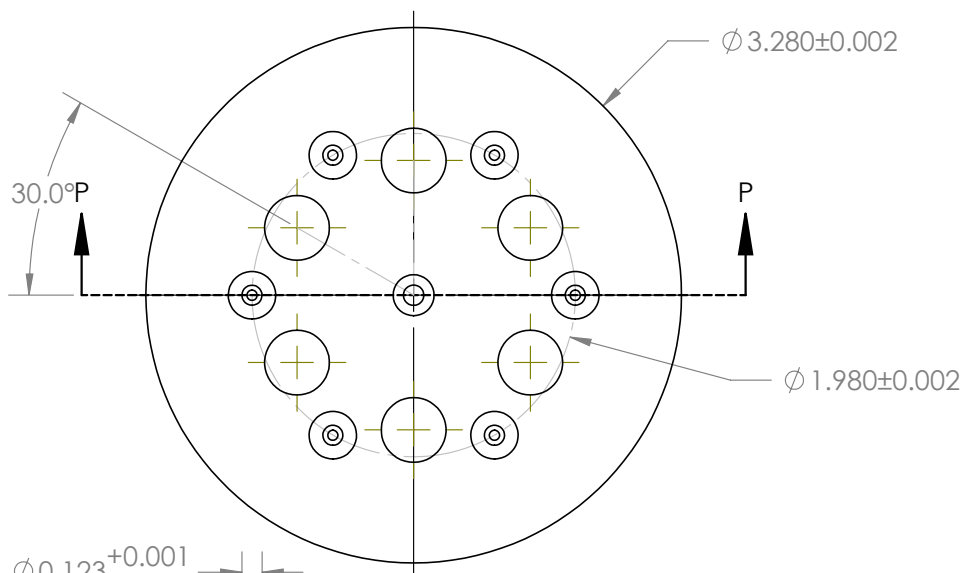
5

4

3

2

1



SECTION P-P
SCALE 1 : 1

131

DO NOT SCALE DRAWING		PART NUMBER: RDE1-007LP	
DIMENSIONS (UNLESS OTHERWISE SPECIFIED): INCHES		REVISION: B	
TOLERANCES (UNLESS OTHERWISE SPECIFIED):		TITLE:	
X.XXX	±0.005	Inner Chamber - Wide Channel	
X.XX	±0.01	MATERIAL:	
X.XX°	±0.05°	C101 or C110 Copper	
X.X°	±0.5°	SIZE	
FINISH	63/	A	
unless otherwise noted		SCALE: 1:1.5 WT: 6.8 lbm SHEET 1 OF 2	
NAME	DATE		
DRAWN BY: David P. Stechmann	09/29/2016		
ADVISOR: Stephen D. Heister	09/29/2016		



5

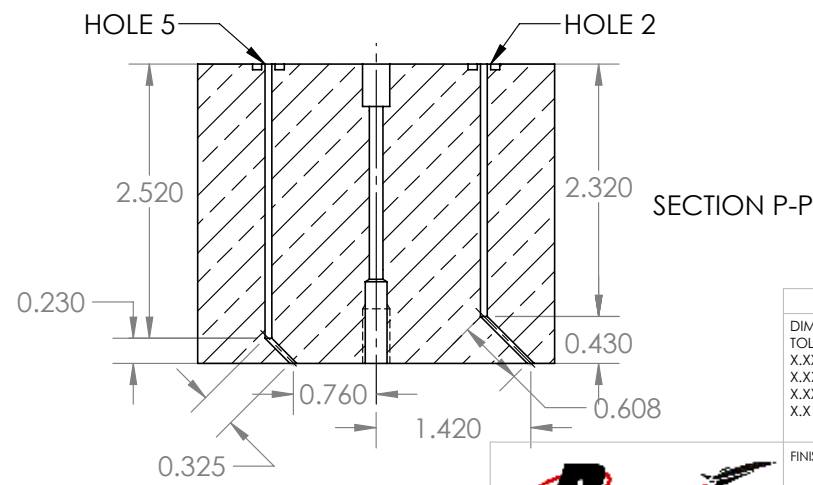
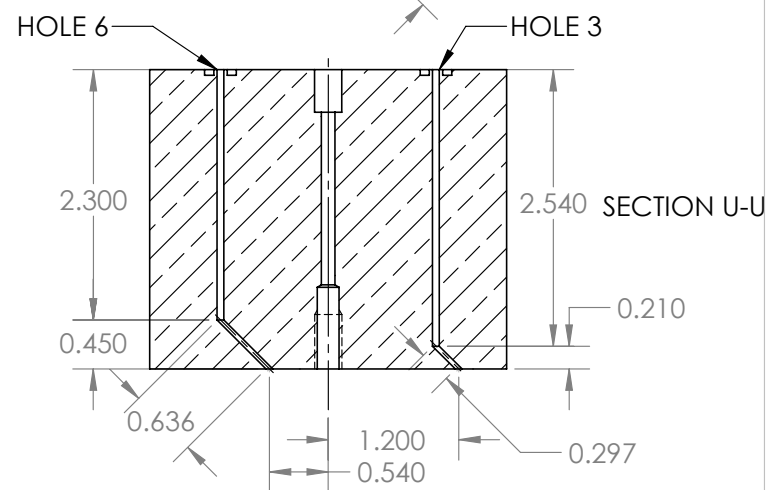
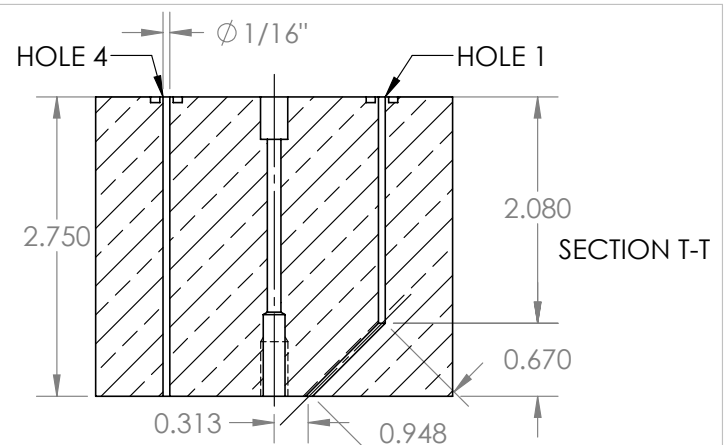
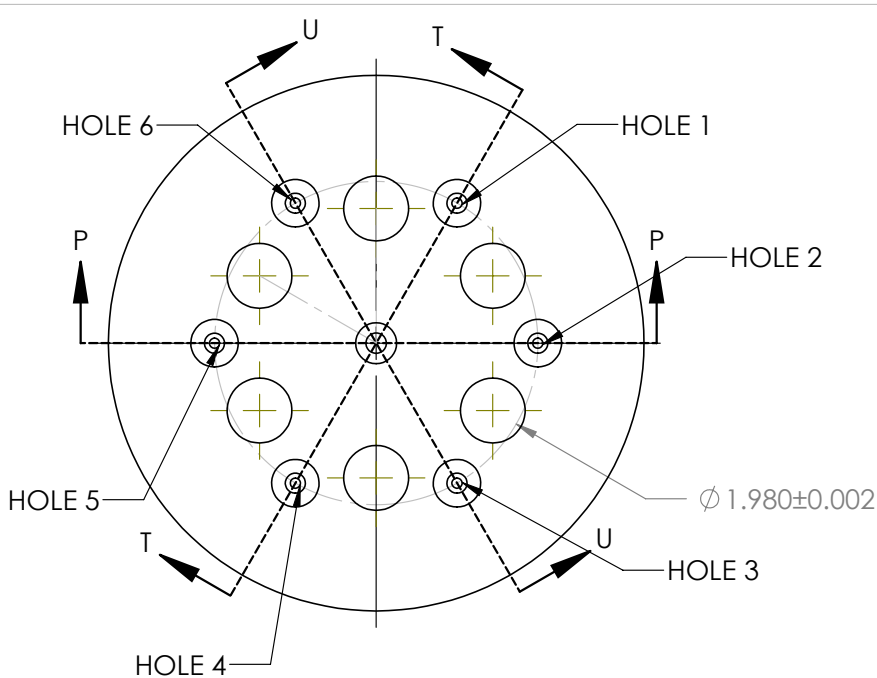
4

3

2

1

132



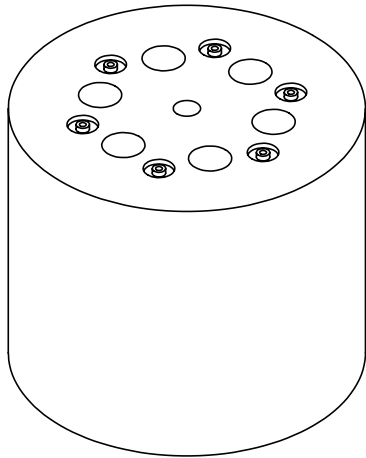
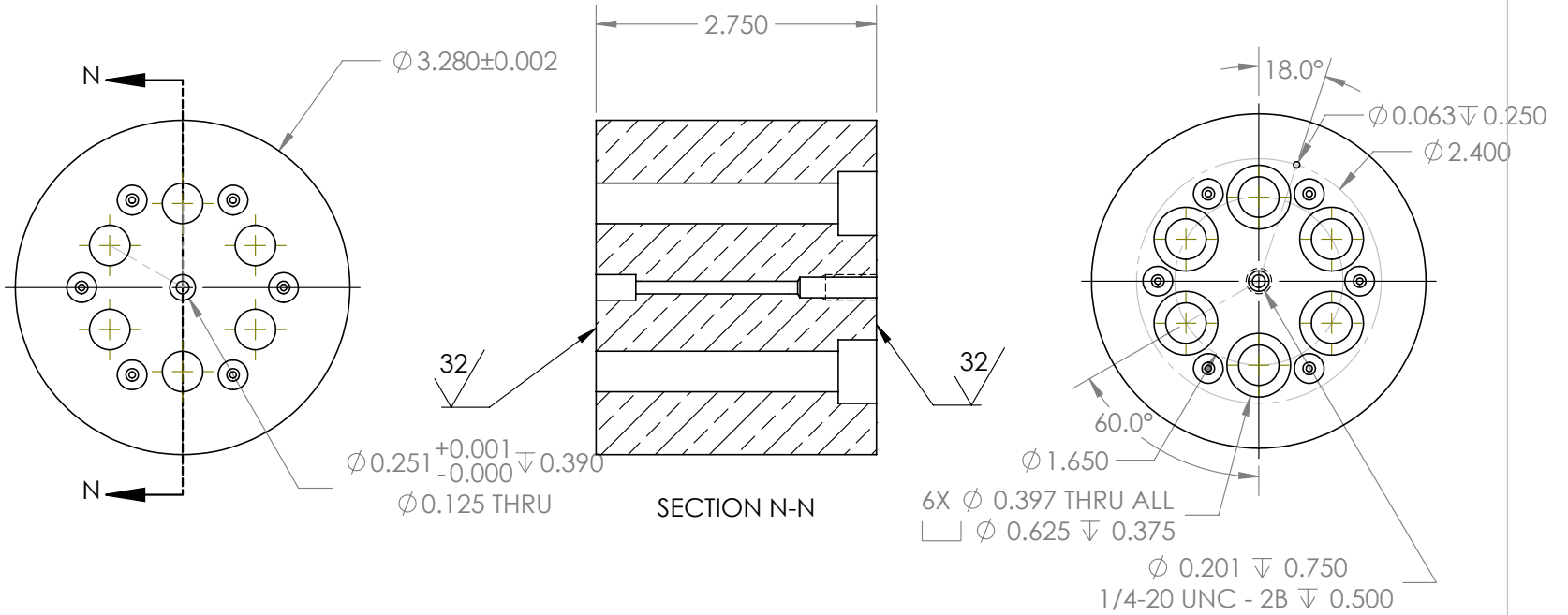
ALL HOLES ARE $\phi 1/16''$
 ALL ANGLED HOLES DRILLED AT 45°
 FROM CENTERLINE



DO NOT SCALE DRAWING	
DIMENSIONS (UNLESS OTHERWISE SPECIFIED): INCHES	
TOLERANCES (UNLESS OTHERWISE SPECIFIED):	
X.XXX	± 0.005
X.XX	± 0.01
X.XX°	$\pm 0.05^\circ$
X.X°	$\pm 0.5^\circ$
FINISH	63/
unless otherwise noted	
NAME	DATE
DRAWN BY: David P. Stechmann	09/29/2016
ADVISOR: Stephen D. Heister	09/29/2016

PART NUMBER: RDE1-007LP	
REVISION: B	
TITLE: Inner Chamber - Wide Channel	
MATERIAL:	SIZE
C101 or C110 Copper	A
SCALE: 1:1.5	WT: 6.8 lbm
SHEET 2 OF 2	

5 4 3 2 1

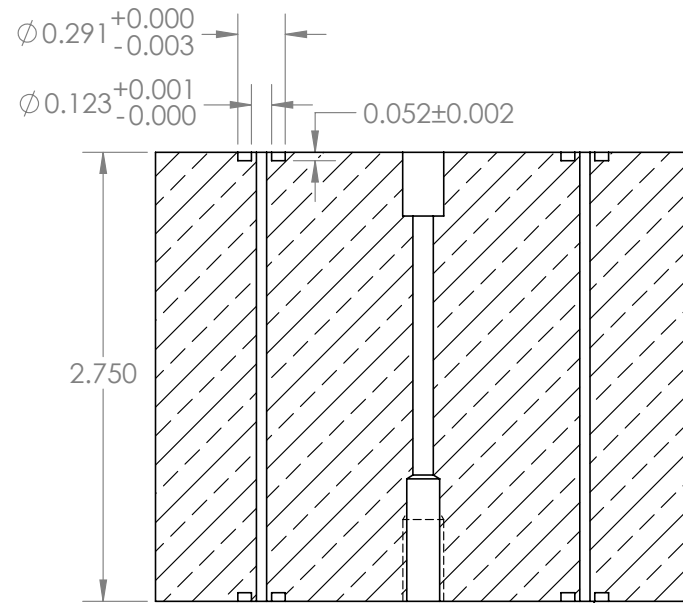
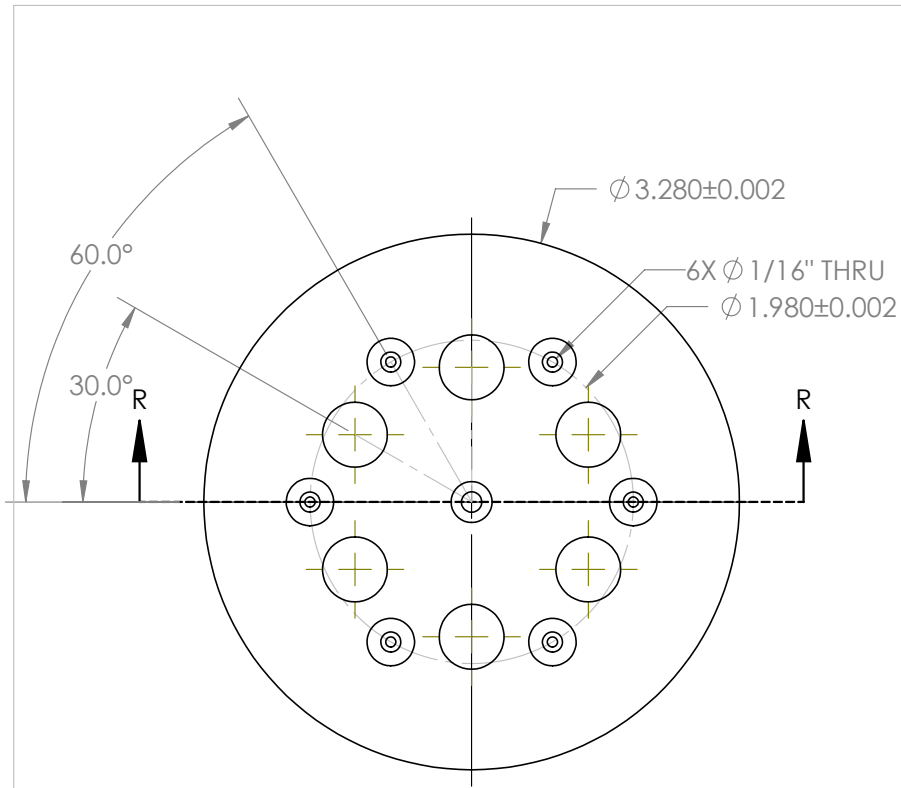


DO NOT SCALE DRAWING	
DIMENSIONS (UNLESS OTHERWISE SPECIFIED): INCHES	
TOLERANCES (UNLESS OTHERWISE SPECIFIED):	
X.XXX	± 0.005
X.XX	± 0.01
X.XX°	$\pm 0.05^\circ$
X.X°	$\pm 0.5^\circ$
FINISH	63/
unless otherwise noted	
NAME	DATE
DRAWN BY: David P. Stechmann	09/29/2016
ADVISOR: Stephen D. Heister	09/29/2016

PART NUMBER: RDE1-007LP	
REVISION: B	
TITLE: Inner Chamber - Wide Channel	
MATERIAL:	SIZE
C101 or C110 Copper	A
SCALE: 1:1.5	WT: 6.8 lbm
SHEET 1 OF 2	



134



SECTION R-R
SCALE 1 : 1
6X O-RING GLANDS
ON EACH SIDE

DO NOT SCALE DRAWING		PART NUMBER: RDE1-007LP	
DIMENSIONS (UNLESS OTHERWISE SPECIFIED): INCHES		REVISION: B	
TOLERANCES (UNLESS OTHERWISE SPECIFIED):		TITLE:	
X.XXX	± 0.005	Inner Chamber - Wide Channel	
X.XX	± 0.01	MATERIAL:	
X.XX°	$\pm 0.05^\circ$	C101 or C110 Copper	
X.X°	$\pm 0.5^\circ$	SIZE	
FINISH	63/	A	
unless otherwise noted		SCALE: 1:1.5 WT: 6.8 lbm SHEET 2 OF 2	
NAME		DATE	
DRAWN BY:	David P. Stechmann	09/29/2016	
ADVISOR:	Stephen D. Heister	09/29/2016	



5

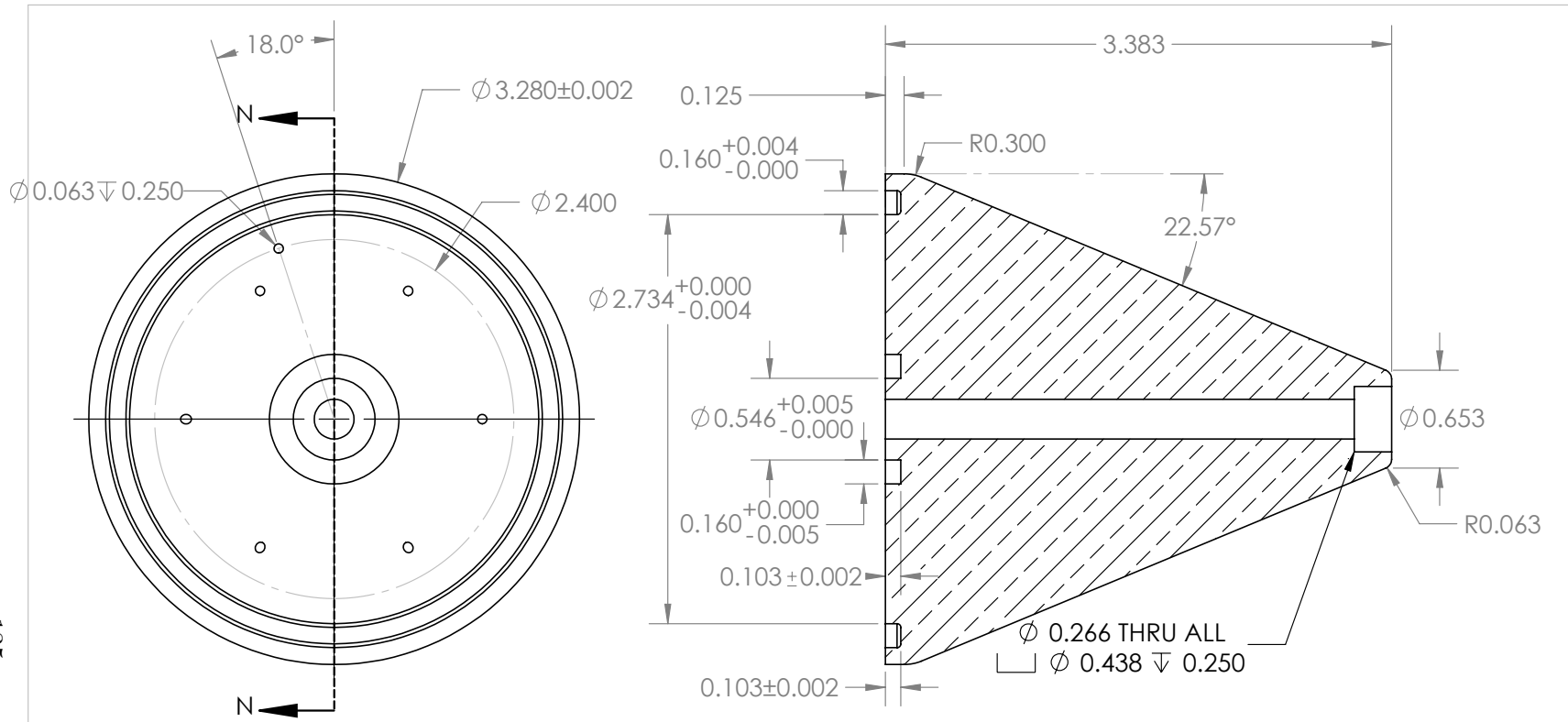
4

3

2

1

135



SECTION N-N

SCALE: 1:1.5



DO NOT SCALE DRAWING		PART NUMBER: RDE1-015LP	
DIMENSIONS (UNLESS OTHERWISE SPECIFIED): INCHES		REVISION: NEW	
TOLERANCES (UNLESS OTHERWISE SPECIFIED):		TITLE:	
X.XXX ±0.005		Low Pressure Nozzle Plug	
X.XX ±0.01		MATERIAL:	
X.XX° ±0.05°		C101 or C110 Copper	
X.X° ±0.5°		SIZE	
FINISH	32/	A	
unless otherwise noted			
	NAME	DATE	
DRAWN BY:	David P. Stechmann	11/17/2016	
ADVISOR:	Stephen D. Heister	11/17/2016	
SCALE: 1:1		WT: 2.7 lbm	SHEET 1 OF 2

5

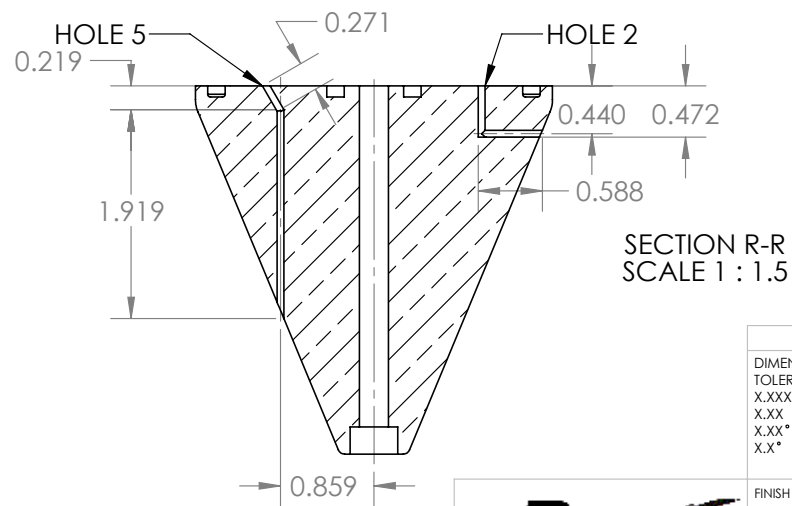
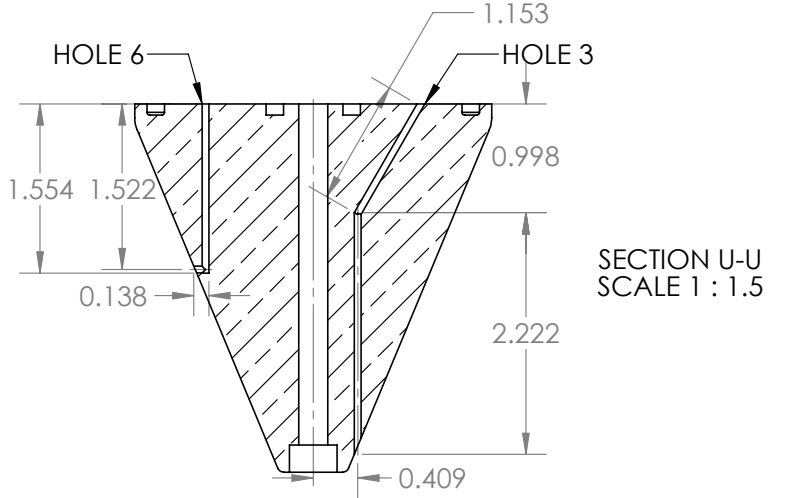
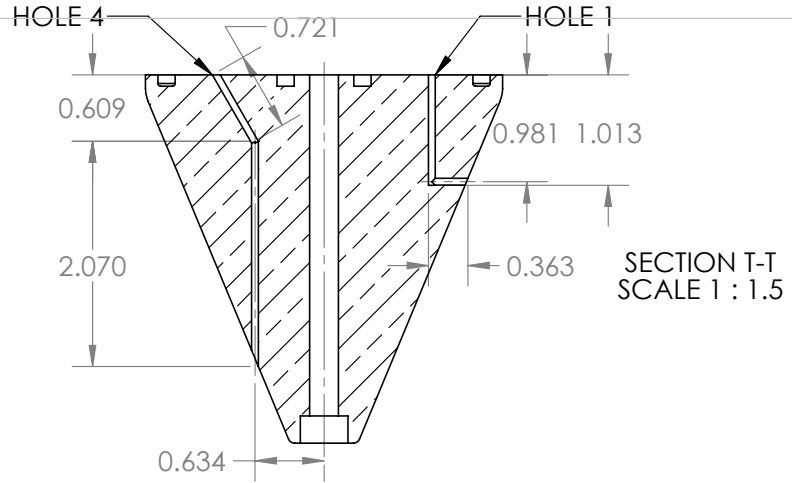
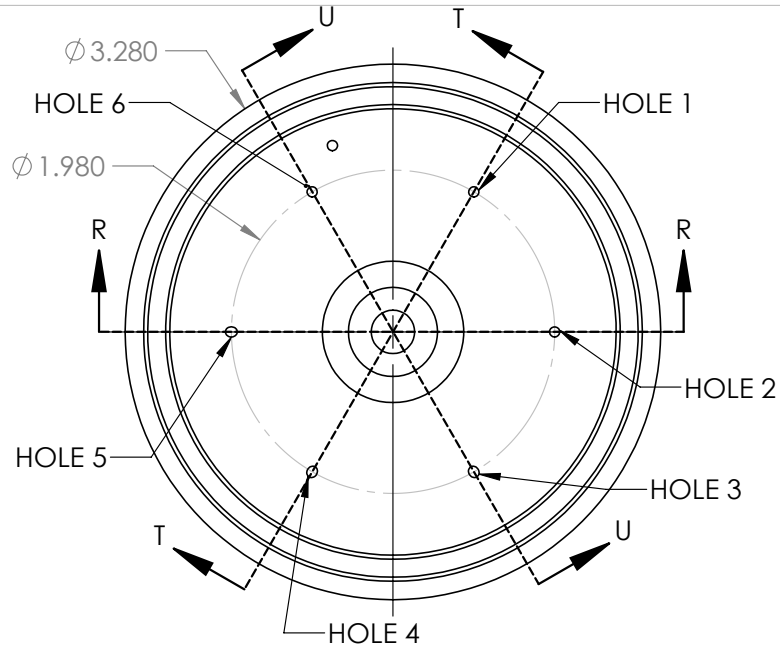
4

3

2

1

136



ALL HOLES ARE $\phi 1/16"$
 ALL ANGLED HOLES ARE ON 30°
 FROM CENTERLINE



DO NOT SCALE DRAWING	
DIMENSIONS (UNLESS OTHERWISE SPECIFIED): INCHES	
TOLERANCES (UNLESS OTHERWISE SPECIFIED):	
X.XXX	± 0.005
X.XX	± 0.01
X.XX°	$\pm 0.05^\circ$
X.X°	$\pm 0.5^\circ$
FINISH	32/
unless otherwise noted	
NAME	DATE
DRAWN BY: David P. Stechmann	11/17/2016
ADVISOR: Stephen D. Heister	11/17/2016

PART NUMBER: RDE1-015LP	
REVISION: NEW	
TITLE: Low Pressure Nozzle Plug	
MATERIAL: C101 or C110 Copper	SIZE A
SCALE: 1:1	WT: 2.7 lbm
SHEET 2 OF 2	

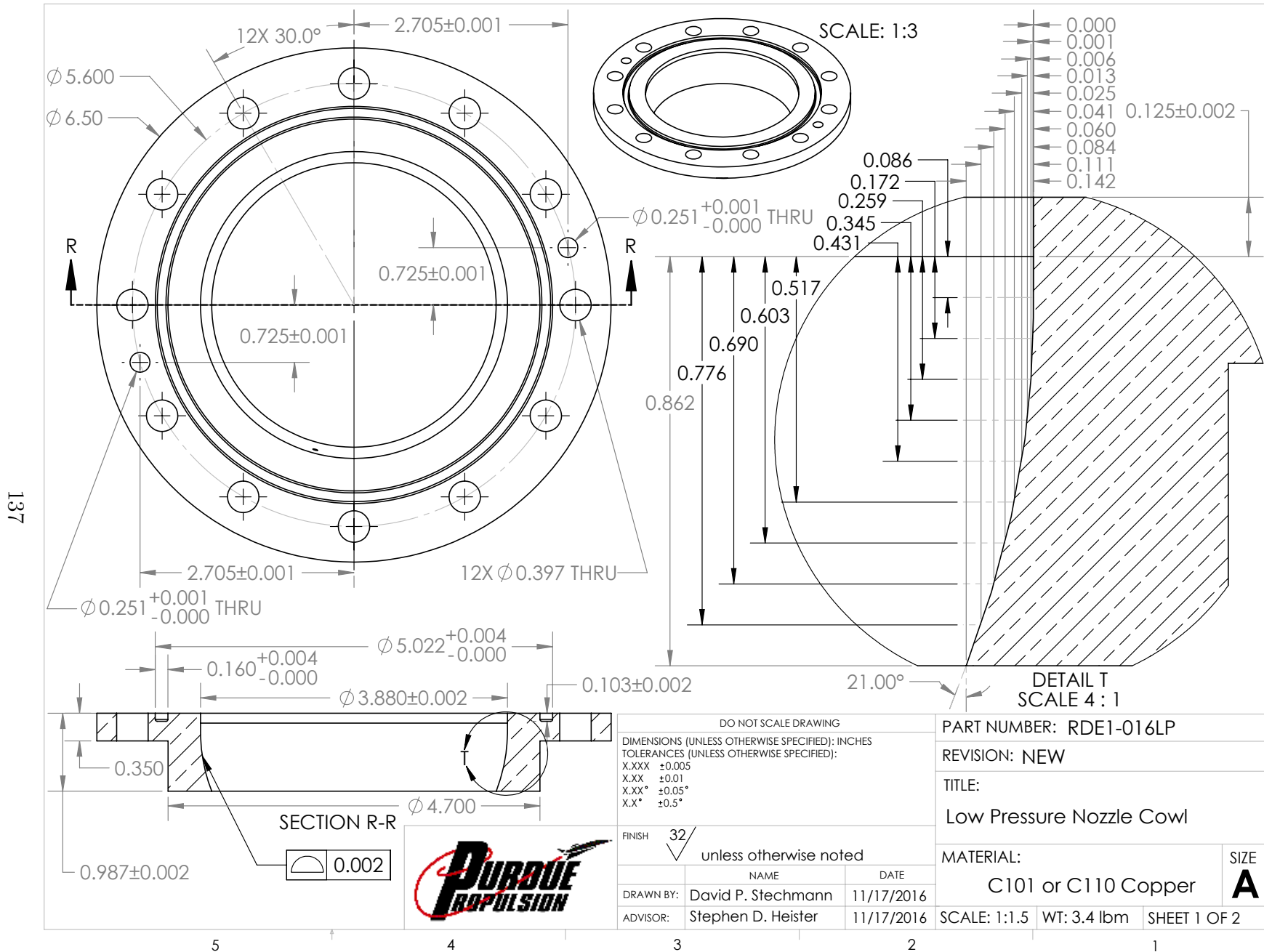
5

4

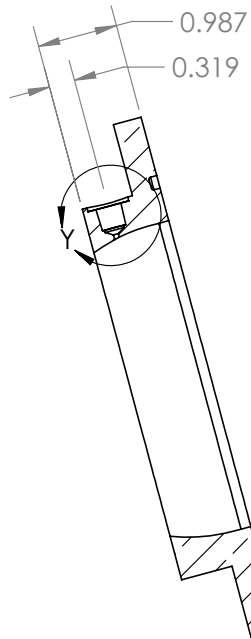
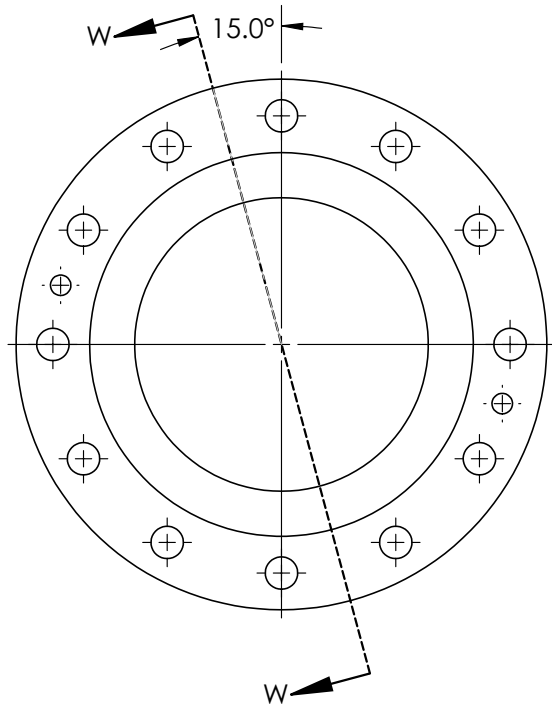
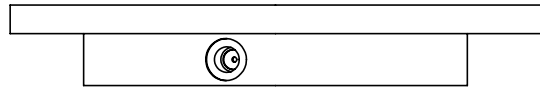
3

2

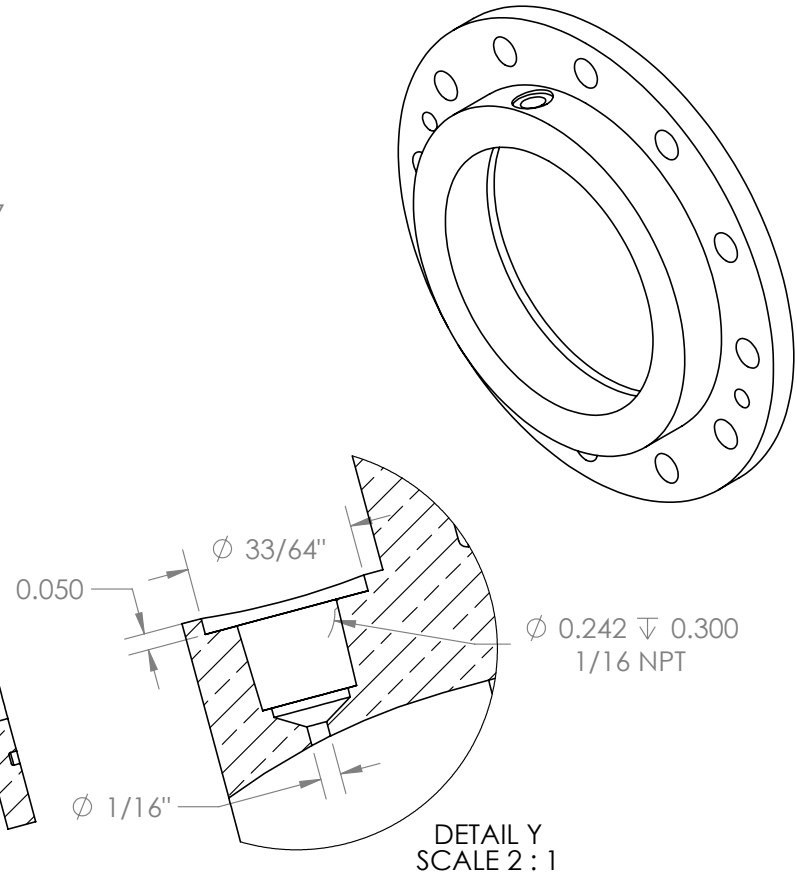
1



138



SECTION W-W
SCALE 1 : 2



DETAIL Y
SCALE 2 : 1



DO NOT SCALE DRAWING	
DIMENSIONS (UNLESS OTHERWISE SPECIFIED): INCHES	
TOLERANCES (UNLESS OTHERWISE SPECIFIED):	
X.XXX	±0.005
X.XX	±0.01
X.XX°	±0.05°
X.X°	±0.5°
FINISH	32/
unless otherwise noted	
NAME	DATE
DRAWN BY: David P. Stechmann	11/17/2016
ADVISOR: Stephen D. Heister	11/17/2016

PART NUMBER: RDE1-016LP	
REVISION: NEW	
TITLE: Low Pressure Nozzle Cowl	
MATERIAL: C101 or C110 Copper	SIZE A
SCALE: 1:1.5	WT: 3.4 lbm
SHEET 2 OF 2	

5

4

3

2

1